DISS. ETH NO. 26374

Transparent metasurfaces harvesting sunlight for icephobicity, antifogging and water repellency applications

A thesis submitted to attain the degree of
DOCTOR OF SCIENCES of ETH Zurich
(Dr. sc. ETH Zurich)

presented by

Efstratios Mitridis
Diploma in Chemical Engineering, Aristotle University of Thessaloniki

born on 08.09.1992
citizen of Greece

accepted on the recommendation of

Prof. Dr. Dimos Poulikakos, ETH Zurich
Prof. Dr. Christoph Müller, ETH Zurich
Prof. Dr. Giulia Tagliabue, EPFL
Dr. Thomas M. Schutzius, ETH Zurich

2019

ABSTRACT

My thesis revolves around the water–energy nexus, from a surface engineering aspect, taking advantage of the heat that the sun can provide through light-absorbing surfaces that do not compromise their transparency. The focus of the thesis is on applications which often require a significant degree of transparency, such as on windows, windshields, eyewear and all kinds of optics in general. The importance of ensuring water or ice-free surfaces is not only due to aesthetic purposes, but also to maintain functionality of vehicles and devices and definitely for safety purposes. I will try to investigate the effect of water condensation on surface visibility and quantify the strength of ice adhesion on surfaces with the purpose of preventing fogging and freezing from happening or counteracting their impact by means of non-conventional technology and rational micro/nano-engineering. I will then go one step further with proposing a method for complete elimination of water from surfaces by stopping its nucleation in the first place.

More specifically, in the first chapter of my experimental study, I study frost formation and ice adhesion on surfaces in sub-zero temperatures and establish the metasurface-based technology – at this first stage – for effective anti-icing and deicing. It is well-known that inhibiting frost formation is critical in modern technology, such as in aviation, vehicles and public infrastructure, to give a few examples. Current technologies are either based on spending large amounts of energy to melt ice, applying mechanical forces to shed ice off surfaces, or using chemicals to depress the melting point of water. My contribution is the development of metasurfaces, nanocomposites of ultra-thin gold and titania layers, that are compatible with transparent surfaces, as a totally passive means of rapid anti-icing and de-icing with abundant sunlight. Depending on the severity of environmental conditions that our surfaces are exposed to, we can tune their transparency level accordingly. I found that metasurfaces can cause a > 10 °C temperature increase when applied on other surfaces, leading to quick deicing within a few seconds or minutes, and reducing the ice nucleation probability multifold.

In the second chapter, I investigate a fresh approach to battling surface fogging and visibility loss in transparent surfaces. As a matter of fact, fogging can have adverse effects on visibility, affecting the performance of windows, windshields, optical systems and eyewear. These are just a few examples that make us realize the need for more research on developing new solutions against fogging. Admittedly, there is a host of ongoing research based on superhydrophilic and superhydrophobic coatings that either form a continuous water film or prevent droplet coalescing and facilitate their removal, however both approaches suffer from reduced performance and visibility over time. I propose new and passive anti-fogging coatings based on metasurfaces and sunlight, which in combination with surface chemistry can delay or prevent fogging. The results show a up to 4-fold reduction in defogging time under severely supersaturated conditions, providing superior visibility through surfaces with respect to current state-of-the-art technologies, while being environmentally friendly and ready for possible large-scale fabrication in the future.

The last chapter of this thesis deals with surface wettability, targeting the field of super-antiwetting multifunctional surfaces. Research has been conducted during the last decades to increase surface water repellency by means of low surface energy chemistry, structured surfaces and flexibility. The behavior of such surfaces for a wide variety of water temperatures has also been investigated, ranging from very cold droplets to hot water. Especially in the case of hot water, there is a pronounced lack of surfaces that can maintain repellency for long periods of time, due to condensate nucleation within the structures, which compromises superhydrophobicity. Another important aspect is the ability of a surface to reversibly transition from a sticky behavior to a water-repellent state, which up to the present was mainly achieved by active methods. This chapter proposes the usage of metasurfaces and sunlight to enhance hot water repellency by heating up surfaces, while maintaining their transparency.

In closing, it is my strong belief that my findings and technology that I developed will potentially help shield real surfaces from the effects of liquid water and ice. At the very minimum, I expect that my results will pave the way towards more research based on utilizing the power of renewable energy sources in everyday applications, unobtrusively and in compatibility with the modern technical requirements.

ZUSAMMENFASSUNG

In meiner Doktorarbeit beschäftige ich mich mit den Zusammenhängen von Wasser und Energie und dem technischen Design von Oberflächen. Diese Oberflächen nutzen die von der Sonne gelieferte Wärme mittels Absorption von Licht, wobei sie zugleich ihre Transparenz bewahren. Der Fokus der Arbeit liegt auf Anwendungen, welche oft ein hohes Mass an Transparenz erfordern, wie beispielsweise Fenster, Windschutzscheiben, Brillen und alle Arten optischer Geräte. Oberflächen wasser- oder eisfrei zu halten hat nicht nur ästhetische Gründe, sondern beeinflusst auch die Sicherheit und Funktionalität von Fahrzeugen und Geräten. Ich werde versuchen, den Einfluss von Wasserkondensation auf die Sichtbarkeit durch Oberflächen zu untersuchen und die Stärke von Eisadhäsion auf Oberflächen zu quantifizieren. Ziel ist es Kondensation und Eisbildung zu verhindern oder mit nicht konventionellen Technologien und rationalem Micro-/Nanoengineering zu bekämpfen. Ich werde dann einen Schritt weitergehen und eine Methode vorschlagen, wie Wasser auf Oberflächen komplett eliminiert werden kann, indem die Nukleation von Anfang an unterdrückt wird.

Im ersten Kapitel meiner experimentellen Studie untersuche ich Frostbildung und Eisadhäsion auf Oberflächen bei Temperaturen unter dem Gefrierpunkt. Darauf baue ich meine metaoberflächen-basierte Technologie auf, um an erster Stelle, effektives Anti- und Enteisverhalten zu zeigen. Es ist ohne Zweifel, dass das Hemmen von Frostbildung für moderne Technologien, wie in der Luftfahrt, bei Fahrzeugen oder der öffentlichen Infrastruktur, kritisch ist. Heutige Technologien basieren entweder darauf, grosse Mengen Energie zu verbrauchen, um das Eis zu schmelzen, mechanische Arbeit zu leisten, um das Eis von der Oberfläche zu kratzen, oder Chemikalien zu verwenden, die den Schmelzpunkt von Wasser herabzusetzen. Mein Beitrag ist das Entwickeln von Metaoberflächen, die aus nano-composits mit ultradünnen Gold- und Titaniumoxidschichten bestehen und gleichzeitig optische Transparenz bieten können. Diese stellen eine Möglichkeit dar, komplett passiv und schnell mittels Sonnenlicht Oberflächen zu enteisen oder Eisbildung zu verhindern. Abhängig von der Schwere der Umwelteinflüsse, denen unsere Oberflächen ausgesetzt sind, können wir ihre Transparenz anpassen. Ich konnte zeigen, dass Metaoberflächen, welche auf andere Oberflächen aufgetragen werden können, eine Temperaturerhöhung von mehr als 10 °C erreichen können, was zu schnellem Enteisen innerhalb weniger Sekunden oder Minuten führt und die Wahrscheinlichkeit von Eisnukleation um ein Vielfaches reduziert.

Im zweiten Kapitel untersuche ich einen neuartigen Ansatz um das Beschlagen und den Verlust der Transparenz von Oberflächen zu verhindern. Das Beschlagen von Oberflächen kann ungünstige Effekte auf die Durchsichtigkeit haben, was die Leistungsfähigkeit von Fenstern, Windschutzscheiben, optischen Systemen oder Brillen beeinträchtigt. Dies sind nur einige Beispiele, die uns allen klar machen sollten, dass mehr Forschung im Bereich von neuen Lösungen gegen das Beschlagen von Oberflächen nötig ist. Zugegebenermassen existiert bereits eine Unzahl an laufender Forschung, welche sich mit superhydrophilen und superhydrophoben Beschichtungen beschäftigt. Diese formen entweder einen kontinuierlichen Wasserfilm oder verhindern das Zusammenschliessen von Wassertröpfchen und erleichtern deren Entfernung. Nichtdestotrotz leiden beide Ansätze mit der Zeit unter einer reduzierten Leistungsfähigkeit und Durchsichtigkeit. Ich schlage neue und passive Antikondensationsbeschichtungen vor, welche auf Metaoberflächen und Sonnenlicht basieren und in Kombination mit einer geeigneten Oberflächenchemie das Beschlagen verzögern oder verhindern können. Die Resultate zeigen eine 4-fache Reduktion in der Zeit, die nötig ist, um das Komdenzwasser auf der Oberfläche zu verdampfen, und dies unter extrem übersättigten Bedingungen. Dies bedeutet verbesserte Sichtbarkeit durch derartige Oberflächen im Vergleich zu aktuell existierenden Technologien. Die Beschichtungen sind umweltfreundlich und können in Zukunft leicht auf grösserer Skala hergestellt werden.

Das letzte Kapitel dieser Doktorarbeit beschäftigt sich der Benetzbarkeit von Oberflächen und setzt sich zum Ziel, eine multifunktionale, super-unbenetzbare Oberfläche zu entwickeln. In den letzten Jahrzehnten wurde viel Forschung durchgeführt, um das Wasserabweisungsvermögen von Oberflächen zu verbessern mittels strukturierten Oberflächen, Flexibilität oder Chemie, um eine tiefe Oberflächenenergie zu erzeugen. Das Verhalten derartiger Oberflächen wurde auch für eine grosse Spannbreite an Wassertemperaturen untersucht, von sehr kalten Tropfen bis zu heissem Wasser. Besonders im Falle von heissem Wasser besteht ein grosser Mangel an Oberflächen, welche das Wasserabweisungsvermögen für längere Zeit aufrechterhalten können. Grund dafür ist die Kondensationsnukleation in der Oberflächenstruktur, welche die Superhydrophobie beeinträchtigt. Ein weiterer wichtiger Aspekt ist die Fähigkeit einer Oberfläche, von einem wasseranziehenden zu einem -abweisenden Status zu wechseln. Bis heute wurde dies meist durch aktive Methoden erreicht. In diesem Kapitel schlage ich die Nutzung von Metaoberflächen und Sonnenlicht vor, um Oberflächen aufzuwärmen und dadurch das Abweisungsvermögen gegen heisses Wasser zu erhöhen, ohne einen Kompromiss bezüglich Transparenz einzugehen.

Abschliessend bin ich der Ansicht, dass meine Ergebnisse und die Technologie, die ich entwickelt habe, möglicherweise helfen werden, echte Oberflächen vor den Effekten von flüssigem Wasser und Eis zu schützen. Ich erwarte mindestens, dass meine Resultate den Weg für weitere Forschung im Bereich der Nutzung von erneuerbaren Energiequellen in Alltagsanwendungen weisen können, welche unauffällig und kompatibel mit modernen technischen Anforderungen sind.

ACKNOWLEDGEMENTS

During the four years of my doctoral studies, I have gained significant experiences, not only in the scientific sense but also within a broader concept of collaboration and collegiality. First of all, I would like to express my deepest gratitude to Prof. Dr. Dimos Poulikakos who selected me out of numerous candidates and gave me the opportunity to proceed with my doctorate in a world-class university, ETH Zurich. His open-mindedness in terms of scientific approaches, his educated advice and supervision, as well as the freedom I had on how to proceed with research on several different topics are the elements that anyone would dream of finding in a Professor, hence my recognition to him.

Secondly, my research on a daily basis would not have been possible without the continuous supervision by our group leader, Dr. Thomas Schutzius, who was the first person from the group to meet with during my first interview as a candidate. His well-thought advice, demanding but rational requests, practical assistance in experiments and of course his highly motivated approach to everyday life clearly helped me improve my skills and have more energy during the working days.

Next, I would like to thank Prof. Dr. Giulia Tagliabue and Prof. Dr. Christoph Müller who, as my external co-examiners, had the patience to read and critically examine my thesis, giving me the unique opportunity to conclude my doctorate studies.

It would also not be fair not to thank all my colleagues, members of LTNT group, for the great time we had together, inside and outside the working hours. My special thanks go to my office mates, Gustav Graeber and Nafsika Chala, who put up with my loud voice and discussions with students, always with smiles on their faces. I also acknowledge the valuable contribution of my students, Bachelor and Master, who sped up the execution of experiments and positively contributed to publications.

Furthermore, I would like to thank Jovo Vidic and Peter Feusi for their continuous support during my doctorate. Jovo assisted me with experimental setups and data acquisition, while Peter was the mastermind of many mechanical constructions and chambers required in experiments. It is such necessary background support that helps one travel the extra mile and save valuable time. Since part of my work was in IBM’s cleanroom facilities in Rüschlikon, I would like to express my gratitude to Ute Drechsler, who as a leading member of the BRNC team supported me in every fabrication step and proposed numerous possible ways of achieving the same outcome.

In closing, all this would have been just a dream had it not been for my parents, who encouraged me to move to Switzerland and expand my horizons, also providing full emotional and practical support throughout these – admittedly challenging – four years of my life.

TABLE OF CONTENTS

LIST OF FIGURES

LIST OF MAIN VARIABLES AND ABBREVIATIONS

Metasurfaces leveraging solar energy for icephobicity

Variables

α	thermal diffusivity
β	thermal expansion coefficient
$\varepsilon_{\mathrm{r,nc}}$	permittivity of nanocomposite
λ	wavelength of light
ν	kinematic viscosity
v_{Au}	volumetric concentration
τ_{yx}	shear stress
$\mathcal{A}$	light absorption
d	gold nanoparticle diameter
D	diameter of illuminated area
F	mechanical force
g	acceleration of gravity
l	substrate thickness
I_{r}	solar irradiance
k	thermal conductivity
L	film thickness
n	refractive index
N	number of nanoparticles
N_0	total number of particles
N_{L}	number of layers
p	pitch between gold layers
P	power density of light
R	cylinder radius
$\mathcal{R}$	light reflection
Ra	Rayleigh number
t	time
T	temperature
$\mathcal{T}$	light transmission

Abbreviations

Au	gold
DC	direct current
DMF	dimethylformamide
IR	infrared
NMP	N-methyl pyrrolidone
PMMA	acrylic
PVDF	polyvinylidene fluoride
RF	radio frequency
RTD	resistance temp. detector
TiO_2	titanium dioxide

Transparent metasurfaces counteracting fogging by harnessing sunlight

Variables

δ	image distortion
$\Delta\mathrm{s}$	distance that a dot moves
θ	water contact angle
$\mathcal{A}$	light absorbance
C	image clarity
d	diameter of a dot
I	intensity
k	number of bilayers
p	water vapor pressure
p_L	saturation vapor pressure
P	performance factor
$\mathcal{R}$	light reflectance
t	time
T	temperature
$\mathcal{T}$	light transmittance
t_df	defogging time
V_d	droplet volume

Abbreviations

Au	gold
DC	direct current
iCVD	initiated chemical vapor deposition
IR	infrared
PFDA	perfluorodecyl acrylate
RF	radio frequency
TBPO	tert-butyl peroxide
TCVS	trichlorovinylsilane
TiO_2	titanium dioxide

Transparent metasurfaces naturally boosting their own superhydrophobicity by absorbing sunlight

Variables

α	correction factor
γ	water surface tension
δ	meniscus penetration depth
θ_a	advancing contact angle
θ_r	receding contact angle
λ	wavelength of light
v	water droplet velocity
ρ	water density
τ_c	contact time
τ_f	filling time
φ	wetting fraction
Φ	impalement probability
$\mathcal{A}$	light absorbance
d	micropillar diameter
h	micropillar height
p	micropillar pitch
P	power density of light
$\mathcal{R}$	light reflectance
R_0	initial droplet radius
t	time
T	temperature
$\mathcal{T}$	light transmittance
We	Weber number

Abbreviations

Au	gold
iCVD	initiated chemical vapor deposition
IR	infrared
PDMS	polydimethylsiloxane
PFDA	perfluorodecyl acrylate
PUA	polyurethane acrylate
SiO_2	silicon dioxide
TBPO	tert-butyl peroxide
TCVS	trichlorovinylsilane
TiO_2	titanium dioxide
UV	ultraviolet

1. INTRODUCTION

1.1. Challenges in water and energy

Water and energy are two commodities that the world needs desperately. More water means requirements for more energy, and production of more energy requires more water.[1] This is one of the predominant interpretations of the water–energy nexus in the 21st century. In terms of availability, water is scarce in densely populated areas and their surroundings, especially the amounts required for agricultural purposes.[2] At the same time, energy sources, especially the ones based on coal, oil and natural gas, have become significantly scarcer since the 1970s.[3] There is also a lot of politics and policy making when water and energy rely on each other.[4] The thirst for energy has been responsible for major challenges in modern civilization, such as global warming, air pollution and chemical pollution.[5] It is therefore clear that there is urgent need for green energy and minimization of energy consumption.

Going beyond the aforementioned framework of water and energy interplay, thinking out of the reach of politics and resource availability, there is an – often – overlooked set of water–energy interactions that affect everyone in everyday life activities. This is interfacial phenomena that involve a surface and presence of water, in its liquid or solid state. Fogging is a common example of unwanted presence of water on surfaces, affecting a wide variety of surfaces, from windows to eyeglasses and optical systems.[6] Furthermore, the solid state of water, ice, causes even more problems in applications such as aviation,[7] automobiles[8] and power lines.[9] Numerous active and passive approaches exist to tackle surface icing and fogging, however all of them come with several disadvantages that make one question their applicability in long-term practical scenaria. This is exactly the inspiration behind the research associated with this thesis. Essentially, we will attempt to answer the following questions: Can we find alternative approaches to removing unwanted water off surfaces or reducing its negative implications in icing and fogging? Can this be done without spending energy from conventional sources and affecting the environment?

1.1.1. Surface icing

Having mentioned the general implications of the water–energy nexus on surfaces, we will begin with a phenomenon which does not only cause fear and paralyzes most everyday activities when it occurs, but it also poses significant dangers to people and infrastructure: icing. Icing has negative consequences in many applications, from airplanes[7] and vehicles[8] to transportation[10] and buildings.[11] Overall, the financial impact of icing and the associated infrastructure of counteracting it are quite significant.[12,13] Thinking beyond statistics and financial data, one could realize the real cost of icing in human lives is much higher than anticipated. In the history of aviation alone, icing was, or suspected to be, a factor in almost 1000 accidents.[14] It is thus justified to give ice the attention it deserves, as scientists have righteously done over the last century.

Countless strategies to mitigate icing have been developed. In terms of passive approaches, meaning one does not need energy to induce de-icing or prevent ice formation, research has been focused on rational engineering of superhydrophobic surfaces,[15–21] which have been known to reduce ice adhesion and facilitate shedding of ice off surfaces, as well as liquid-like surfaces, infused with liquid substances.[22,23] Needless to say, more classical countermeasures against icing include resistive heating[24] and ice removal by mechanical means.[25]

All approaches mentioned above suffer from several disadvantages, which could be either the requirement for – a lot of – energy or reduced practical value due to lack of optical transparency or long-term endurance.[22,26] There is clearly need for developing strategies with fewer – if any – disadvantages compared to the present ones, if we want to move towards a sustainable future.

1.1.2. Surface fogging

As we already briefly discussed, icing is not the only concern when it comes to water–surface interactions. In fact, uncontrolled liquid water nucleation on surfaces, hereafter termed fogging, can have a detrimental impact in a plethora of everyday applications, for example in windows, windshields, displays, lenses, eyewear and all kinds of goggles and spectacles.[6] Apart from the aesthetic aspect of fogging, there are serious safety implications, for example when visibility is lost while driving a car, or in challenging activities such as scuba diving. This is of course the reason why scientists have developed multiple solutions to alleviate fogging or – realistically speaking – reduce its adverse effects for certain amounts of time.

Going one logical step back, fogging occurs when microscopic water droplets form on a surface, and when they coalesce, they eventually form a continuous water layer, depending on the hydrophilicity of the surface. Temporary passive solutions target exactly this continuous water layer case which is promoted by rendering a surface superhydrophilic.[27,28] Another pathway is via more permanent passive solutions taking advantage of the other extreme partial wetting case, superhydrophobicity, which has led to the development of self-cleaning surfaces through rational micro and nanoengineering. There are also emerging bioinspired approaches which attempt to prevent possible loss of hydrophobicity when water droplets coalesce,[29–32] rendering the surfaces water-repellent and suitable for anti-fogging.

All of these approaches bear one or more disadvantages, ranging from loss of effectiveness due to contamination[33] to condensate nucleation within the texture of carefully engineered surfaces, which renders them non-functional in high relative humidity conditions.[34,35] This discussion leads us to the conclusion that there is urgent need for the development of a comprehensive defensive strategy against fogging, possibly by rethinking all current research approaches to anti-fogging and defogging.

1.1.3. Droplet repellency

As it has been made obvious in the previous paragraphs, many approaches to counteracting surface icing and fogging revolve around reducing the wettability of surfaces, making water less prone to form and stay on a surface or facilitating its removal by some external force. It is therefore in our best interests to work on the basis of hydrophobicity and develop water-repellent surfaces with very high repellency and robust performance.

In the real world, water droplets hit onto a surface in a dynamic manner, and research has been conducted on how to repel those droplets, specifically by reducing surface energy,[36–39] combinations of open and closed structures,[40–42] designing special surfaces with hierarchical roughness[43–47] and providing flexibility[37,48,49] to absorb part of the impact momentum of droplets. As difficult as it is to repel cold and ambient temperature water from surfaces, repelling hot water[50] is especially even more challenging due to condensation within the texture of surfaces when exposed to warm and humid environmental conditions.[34,50,51] Standard condensation resistance practices try to minimize the presence of water in the first place or reduce its residence time[52,53] or adhesion force.[50] A fraction of the research on superhydrophobic surfaces is also dedicated to reversible repellency,[54,55] which is the process of pushing water out of the texture in case it was previously condensed or pushed into it.

Despite the amount of research in the field of super water-repellent surfaces, there is still significant room to employ alternative approaches that will try to address some of the disadvantages of existing methods, the most important of which being failure to completely prevent nucleation condensation within the texture, and this is why we propose a new approach through the present thesis.

1.2. Going beyond the state-of-the-art

Without having the purpose of diminishing the suspense – always in scientific terms – of the research presented in this thesis, we will give a few hints on the common denominator that links all of its chapters. This is naturally occurring sunlight. We attempt to use sunlight as our sole renewable energy source to mitigate icing, fogging and even enhance the water repellency of properly engineered surfaces. Ideally, sunlight should heat up a surface, leading to lower chances of ice formation, lower water nucleation rates and higher vapor pressures within the texture, preventing penetration of water in the texture. We term the linking element between sunlight and heating "metasurfaces", which are ultrathin light-absorbing coatings that we specifically developed for the purpose of applying them onto a variety of substrates, ranging from smooth, to micro and nanorough. This is our tool that enables all kinds of interesting and useful phenomena under the umbrella of surface–water interactions, while at the same time neither changing the underlying morphology of our surfaces, critical, for example, in water repellency designs, nor compromising their transparency. In essence, utilizing the power of nanotechnology and having studied pre-existing research approaches to the phenomena discussed in this thesis, we employ a fresh approach to mitigate the negative outcomes of these phenomena in a seamless and unobtrusive manner, with the power of sun.

2. THEORY

2.1. Wettability

This chapter provides the basic theoretical background on surface wettability by water, which is an integral part of all phase change and surface interaction phenomena described in this thesis. Upon giving a short overview of the fundamentals of surface–water interactions, followed by wetting transitions and behavior of drops on composite structured surfaces, the behavior of dynamic water drops impacting surfaces will be described. Based on this theory, which partially follows the book by David Quéré et al. entitled "Capillarity and Wetting Phenomena",[56] one can design surfaces with a certain degree of wettability. The focus of this work is on hydrophobic and superhydrophobic surfaces, which are the most challenging to prepare and have practical implications in phase change phenomena, surface transparency and clarity, and repellency.

2.1.1. Fundamentals

Liquid water is a condensed state in which molecules exert attractive forces on each other, which overcome thermal vibrations. When a molecule is in the bulk, a symmetric field of interactions with neighbors is into perspective, whereas a molecule on the surface loses half of its interactions, thus being in a less energetically favorable state. As a consequence, liquid water tends to shape in such a way that it exposes the minimum surface area possible, corresponding to minimum surface energy. This energy per unit area is also called surface tension, typically symbolized with γ, with units of [J m^{-2}] or [N m^{-1}].

When we place a water drop onto a surface, it can either spread and wet it, or try to minimize its contact area with the surface by forming a hemispherical shape. The decision is made by comparing surface energies, with the so-called spreading parameter:

$$S = \gamma_{\mathrm{SO}} - \left(\gamma_{\mathrm{SL}} + \gamma_{\mathrm{LV}}\right) \tag{2.1}$$

where the subscripts in surface tensions are SO for solid–air, SL for solid–water and LV for water-air interactions. If the parameter S has a positive value, water fully spreads on the surface, while for $S < 0$ we are in a partial wetting state, where the drop forms an angle with the substrate. This equilibrium angle is the Young's contact angle, θ_{E}. By projecting the equilibrium forces onto the surface plane, one can derive Young's equation: $\gamma_{\mathrm{LV}} \cos\left(\theta_{\mathrm{E}}\right) = \gamma_{\mathrm{SO}} - \gamma_{\mathrm{SL}}$, or:

$$\cos(\theta_E) = \frac{\gamma_{SO} - \gamma_{SL}}{\gamma_{LV}} \tag{2.2}$$

For $\theta_E < 90^\circ$ the surface is considered hydrophilic, while for $\theta_E > 90^\circ$ it is hydrophobic. Hence, a surface is hydrophobic when $\gamma_{SO} < \gamma_{SL}$. In the extreme case of $\theta_E > 150^\circ$, the surface is called superhydrophobic. Figure 2.1 shows a water drop sitting on a silicon surface rendered hydrophobic by initiated chemical vapor deposition of a silane.

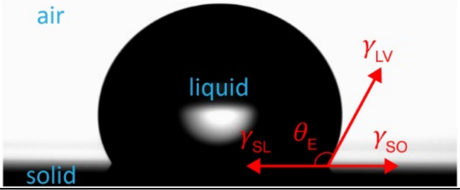

Figure 2.1 Image of a water droplet on a hydrophobic silane-treated silicon surface. The three states of matter, surface tensions and Young's angle, θ_E, are shown in the image.

From equation (2.2) it becomes apparent that in order to increase the Young's angle, one needs to reduce γ_{SL} as much as possible. For a given liquid, water in our case, the only possibility is reduction of the surface energy of the solid. Wetting phenomena are interdisciplinary, involving various scientific fields such as chemistry, physics and surface micro and nanoengineering. Chemistry is vital in reducing surface energy and extensive research has been conducted on chemical modifications of surfaces,[57] for example by plasma treatment of polymers[39] or deposition of ultralow energy fluorosilanes.[58] The effect of surface structuring on wettability will be discussed in the following section.

2.1.2. Wenzel and Cassie–Baxter models

Realistic surfaces are far from the ideal smooth surfaces one envisions in Young's model; therefore, the macroscopic contact angle has to be corrected to account for structural inhomogeneities on the surface. Assuming surface roughness, r, which is the ratio of the real surface area to the apparent surface area, to be much smaller that the drop size, we arrive at Wenzel's relation:

$$\cos\theta^* = r\cos\theta_E \tag{2.3}$$

where θ^* is the apparent contact angle. Based on the previous equation, it is profound that for non-smooth surfaces ($r>1$), $\theta^*<\theta_\mathrm{E}$ if the smooth surface was hydrophilic and $\theta^*>\theta_\mathrm{E}$ if it was already hydrophobic, which brings us to the conclusion that hydrophobicity can be boosted by increasing roughness.[56] In the case of well-defined structures, which provide roughness, such as a square array of circular pillars with diameter d, pitch p and height h (see Figure 2.2), roughness can be calculated as $r=\left(\pi dh+p^2\right)/p^2$.

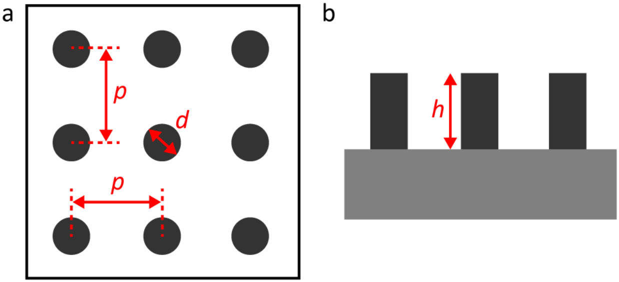

Figure 2.2 Schematic of a square pillar array: **(a)** top-view, **(b)** side-view.

In such composite surfaces (solid and air) like the one shown in Figure 2.2, there is a possibility that under certain conditions air can get trapped under the water drop. If we assign Φ_S and Φ_A to the relative contributions (contact area fraction) of the solid and air, respectively, the macroscopic contact angle can be calculated by the following mixing law: $\cos\theta^*=\Phi_\mathrm{S}\cos\theta_\mathrm{E,S}+\Phi_\mathrm{A}\cos\theta_\mathrm{E,A}$. Substituting $\Phi_\mathrm{A}=1-\Phi_\mathrm{S}$ and knowing that the Young's angle between water and air, $\cos\theta_\mathrm{E,A}$, is 180°, we can write:

$$\cos\theta^*=\Phi_\mathrm{S}\left(1+\cos\theta_\mathrm{E}\right)-1 \tag{2.4}$$

where θ_E is the previously discussed Young's angle in the case of a smooth solid surface. Equation (2.4) implies that if air is trapped between the pillars, the cosine of the apparent contact angle is less or equal to $\Phi_\mathrm{S}-1$, approaching -1, which corresponds to $\theta^*=180^\circ$. However, in reality neither $\Phi_\mathrm{S}=0$ nor $\theta_\mathrm{E}=180^\circ$ can be achieved, justifying the difficulty in designing superhydrophobic surfaces. It has been shown that the Cassie–Baxter regime is energetically favorable beyond a certain angle, $\theta^*=\theta_\mathrm{c}$, called the critical contact angle and defined as $\cos\theta_\mathrm{c}=\left(\Phi_\mathrm{S}-1\right)/\left(r-\Phi_\mathrm{S}\right)$. For $\theta^*>\theta_\mathrm{c}$ the regime is stable while for $90^\circ<\theta^*<\theta_\mathrm{c}$ it is metastable. This leads to the conclusion that if we want to design a superhydrophobic surface we need to achieve a high apparent contact angle while keeping the critical angle as low as possible.[59] Figure 2.3 shows examples of a drop in the Wenzel (right) and Cassie–Baxter (left) states, on a silane-treated substrate with glass micropillars.

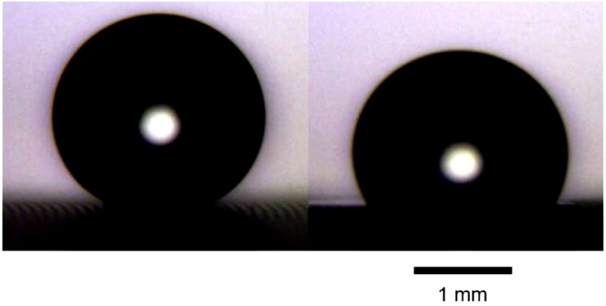

Figure 2.3 Images of water drops in the Cassie–Baxter (left) and Wenzel (right) states, on a micropillared silane-treated hydrophobic substrate.

2.1.3. Droplet dynamics

Up to this point, we only considered the static contact angle of a drop sitting on a surface. Let us discuss now about two common phenomena involving drops that are not static anymore. On the one hand, during evaporation, it is noticed that the volume of the drop decreases with time while the apparent contact angle also decreases until reaching a certain angle at which the drop begins to recede, reducing its surface area on the solid. On the other hand, in a supersaturated environment where condensation occurs, the apparent angle of the condensate (for our purposes, a single droplet) increases up to a certain value beyond which the contact area starts increasing and the contact line moves. Furthermore, any realistic surface with non-zero roughness is expected to have a range of apparent water contact angles as the contact line tries to overcome the asperities and move. Based on these considerations, it is understandable why the contact angle in dynamic phenomena cannot be unique, but instead ranges from θ^*_a, which is the advancing contact angle, to θ^*_r, which is the receding contact angle. The difference between those two angles, given that – always – $\theta^*_\mathrm{a} > \theta^*_\mathrm{r}$, is $\Delta\theta = \theta^*_\mathrm{a} - \theta^*_\mathrm{r}$, called hysteresis. Figure 2.4 shows a single drop moving slowly on a tilted hydrophobic surface. Knowing that there is a range of contact angles and based on our definition of hydrophobicity, one expects that extreme hydrophobicity, superhydrophobicity, can be achieved only if both θ^*_a and θ^*_r are very high, meaning that for dynamic phenomena, there is the extra requirement of very low $\Delta\theta$. In fact, surfaces with apparent contact angles >150° are considered superhydrophobic,[60] as long $\Delta\theta$ is small, typically less than 5–10°.

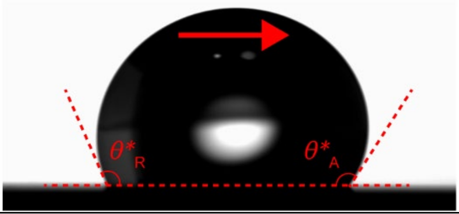

Figure 2.4 Image of a water drop sliding on a tilted silane-treated hydrophobic substrate.

On the basis of dynamic phenomena, liquid water drops are not just formed on or slide off surfaces, but they can be launched from a height and impact on the surface at a certain velocity. Before we proceed, we should define a dimensionless number crucial in explaining the phenomena involved upon drop impact, the Weber number: $We = 2\rho v^2 R_0 / \gamma$, where ρ is the water density, v is impact velocity, R_0 is the initial drop radius and γ is the surface tension of water. We is the ratio of the inertia of a fluid to its surface tension. Assuming we have a surface designed for superhydrophobicity, for low $We \sim v^2$ the drop remains in the Cassie–Baxter state upon impact on the surface. At higher We, a more complicated mechanism is observed. In the first few milliseconds of an impact, the drop deforms while maintaining its advancing contact angle. Subsequently, the drop recedes and retracts, rebounding off the surface as one mass, having stored most of its kinetic energy as surface energy (see Figure 2.5 for a representative drop impact image sequence on a superhydrophobic surface). Due to vibrations, which originate from the different velocities inside the drop, part of its kinetic energy gets dissipated – mostly – internally, and into the substrate and air. The drop bounces lower with each consecutive bounce until it comes to a stop, still in a Cassie–Baxter state. At even higher We, depending on our surface design, the deformation of the drop upon impact is much higher, leading to two possible mechanisms. In the first one, if surface roughness is substantially high, the drop will fragment due to the impact pressure and form multiple smaller drops. For lower roughnesses, the drop will neither rebound nor fragment, rather sticking on the surface upon impalement and transition to the Wenzel state.[61]

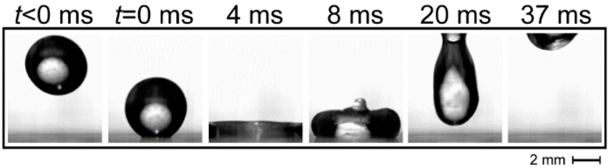

Figure 2.5 Image sequence of a drop impact event on a silane-treated micropillared superhydrophobic surface. The surface was at room temperature.

In order to characterize drop impact events, a first measurable quantity is the time that the drop is in contact with the surface upon impact. Writing the dynamic equation for the drop, taking into account only the capillarity and inertial terms, we get the following relation (for harmonic oscillation):[56] $\tau \propto \sqrt{\rho(2R_0)^3/\gamma}$. The explicit value of τ can be calculated by finding the proportionality constant. For low viscosity liquids, τ is equal to the inertial–capillary time, therefore the correct equation for contact time is:[49]

$$\tau = \frac{\pi}{4}\sqrt{\frac{\rho(2R_0)^3}{\gamma}} \tag{2.5}$$

In the previous paragraph, we discussed about drop impact and the effect of impact velocity (or pressure) on the final wetting state of the drop. As difficult as it might be to design a superhydrophobic surface that can resist pressure-based impalement, for example by increasing surface roughness, through reducing Φ_S, prevention of another possible mechanism of impalement, due to condensation, is far more challenging.[50] Water repellency is maintained if the surface is warmer than the water drop, however the warmer the drop is with respect to the surface the more it is reduced.[62] A hot water impact event causes condensation within the asperities due to diffusive water vapor flow upon supersaturation, which in turn leads to impalement and destroys superhydrophobicity.[50] In order to predict impalement in a condensation-based event, assuming that pressure-based impalement does not simultaneously take place, we need to introduce another measurable quantity, the time required for cavities located between pillars to fill with liquid water. Once a cavity is filled, local superhydrophobicity is compromised. The filling time can be calculated (order of magnitude) by the following equation:

$$\tau_f \sim \frac{\rho h^2}{D\Delta C} \tag{2.6}$$

where h is pillar height, D is the diffusion coefficient of vapor within the air-filled cavity and ΔC is the water vapor mass concentration difference between the drop and the interior of the cavity. In the preferential scenario of filling times lower than the contact time – see equation (2.5) – the water nuclei in the cavity remain small so that the cavity cannot fill entirely, ensuring no contact between the impacting drop and the bottom of the cavity. In the case of $\tau_f \approx \tau$, condensation is pronounced in the pillars closest to the position of initial impact, where the drop stays the longest on. Some cavities might fill with water, which might or might not be enough to compromise macroscopic superhydrophobicity, depending on the type of structures the surface consists of (open *vs* closed structures). In the case that $\tau_f > \tau$, condensation dominates and the cavities fill upon impact, thus compromising superhydrophobicity. Based on equation (2.6), a straightforward way of enhancing condensation-based impalement resistance is increasing pillar height, as $\tau_\mathrm{f} \sim h^2$.

2.2. Nucleation

After introducing the fundamentals of wetting, in this section we will investigate how water can appear on or disappear from a surface by phase change phenomena, which are – per definition – pathways of changing from one state to another. There are six possible phase changes for water, and these are vapor -> liquid (condensation), vapor -> solid (desublimation), liquid - > solid (solidification), liquid -> vapor (vaporization), solid -> liquid (melting) and solid -> vapor (sublimation). Figure 2.6 shows the pressure–temperature equilibrium phase diagram of water.[63] In this work, we investigate phase change phenomena involving cooling at ambient pressure of 1 atm. From the phase diagram, it becomes obvious that the only phase changes possible for isobaric cooling at 1 atm are vapor -> liquid (condensation) and liquid -> solid (solidification), as well as the reverse phenomena. It has to be noted that in the phase diagram the pressure axis corresponds to the partial water vapor pressure. It is thus possible to have other phase changes in atmospheric conditions (total pressure of 1 atm), such as desublimation. However, this would require a very low relative humidity and it is not of relevance at low altitudes. Hereafter, we will use the term freezing for solidification.

Despite the predicted behavior of water when it is in equilibrium with its environment, which is a good starting point in explaining possible phase changes, water in transient metastable states does not exhibit the behavior expected in equilibrium. This is widely exploited in nature; depression of the freezing point is achieved by two methods, colligative and through antifreeze proteins, although the exact mechanisms are not well understood.[64] There are different theories for metastable water, such as the "stability-limit conjecture", according to which the existence of a supercooled region is justified by a single limit of mechanical stability at the liquid–gas triple point, while others suggest that these anomalies are due to a new critical point, above which the two metastable phases of ice cannot be distinguished.[65] This section begins with the fundamentals of freezing, based on the classical nucleation theory, for the cases of homogeneous and heterogeneous nucleation. We discuss the energy barrier to ice nucleation and subsequent nucleation rates, with emphasis on the effect of temperature on nucleation. In the second section, we introduce a similar discussion for condensation and how temperature and surface chemistry affect condensation rates. Parts of the discussion are based on the book by Peter Hobbs entitled "Ice Physics".[66]

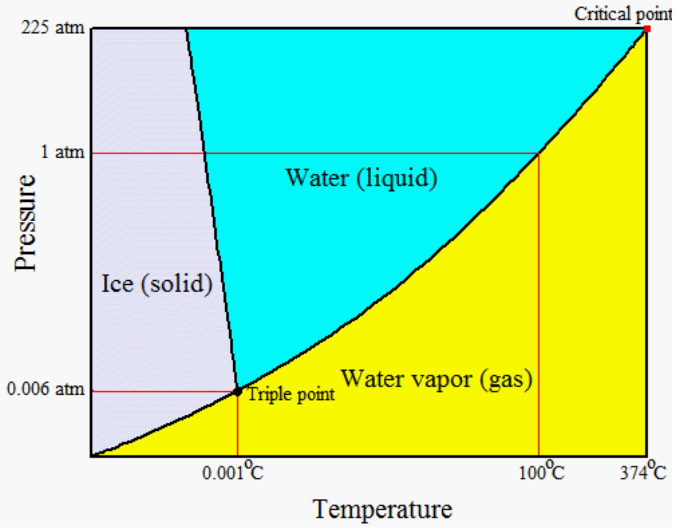

Figure 2.6 Pressure–temperature equilibrium phase diagram of water. Reproduced with permission from Ref.[63].

2.2.1. Ice nucleation

Homogeneous nucleation. As already mentioned, supercooled water can exist due to thermodynamic anomalies. These anomalies cause microscopic variations in its density, temperature and pressure. In freezing, one could envision such anomalies as nanoscopic ice embryos which are born and destroyed continuously in supercooled water, if they are below a certain size, or continue growing if they exceed a critical size. Using the symbols L and S for liquid water and ice, respectively, we can define the Gibbs free energy change associated with the creation of an ice embryo as:

$$\Delta G_{\mathrm{LS}} = n_{\mathrm{S}}\left(\mu_{\mathrm{S}} - \mu_{\mathrm{L}}\right)V + \sigma_{\mathrm{LS}}A \tag{2.7}$$

where n_{S} is the number of molecules per unit volume of ice, μ_{L} and μ_{S} are the chemical potentials per molecule in supercooled water and ice, respectively, σ_{LS} is the water–ice free interfacial energy, V is the volume and A the surface area of the ice embryo. Expressing the chemical potential difference in terms of temperature and pressures, we have:

$$\mu_{\mathrm{S}} - \mu_{\mathrm{L}} = -kT\ln\left(p_{\mathrm{L}} / p_{\mathrm{S}}\right) \tag{2.8}$$

where k is Boltzmann's constant and p_{L}, p_{S} are the saturated vapor pressures of water and ice in the vicinity of the two phases, at temperature T. Substituting (2.8) in (2.7), also accounting for possible geometric deviations from a perfect sphere by using two factors, α and β ($\alpha, \beta \geq 1$), we get to:

$$\Delta G_{\mathrm{LS}} = -\alpha \cdot \frac{4}{3}\pi r^3 n_{\mathrm{S}} kT \ln\left(p_{\mathrm{L}} / p_{\mathrm{S}}\right) + \beta \cdot 4\pi r^2 \sigma_{\mathrm{LS}} \tag{2.9}$$

To find the maximum Gibbs free energy change due to the formation of an ice embryo, we solve equation (2.9) with respect to the embryo radius, r, by taking $\partial \Delta G_{\mathrm{LS}} / \partial r = 0$:

$$r^*_{\mathrm{LS}} = 2\beta\sigma_{\mathrm{LS}} / \left[\alpha n_{\mathrm{S}} kT \ln\left(p_{\mathrm{L}} / p_{\mathrm{S}}\right)\right] \tag{2.10}$$

For radii higher than the one corresponding to the maximum ΔG_{LS}, the energy barrier gets lower and the embryo can be self-sustained, hence we call this radius “critical radius” and symbolize it with r^*_{LS}. We can also calculate the corresponding critical free energy using equations (2.9) and (2.10):

$$\Delta G^*_{\mathrm{LS}} = \frac{16\pi\sigma_{\mathrm{LS}}^3 \xi}{3\left[n_{\mathrm{S}} kT \ln\left(p_{\mathrm{L}} / p_{\mathrm{S}}\right)\right]^2} \tag{2.11}$$

where $\xi = \beta^3 / \alpha^2$. Based on the rate at which ice embryos can overcome the energy barrier, being approximately equal to $\left(kT/h\right)\exp\left(-\Delta g / kT\right)$,[67] where h is the Planck constant and Δg is the activation energy required for transferring a water molecule across the two-phase boundary, the nucleation rate of spontaneously growing ice embryos follows a Boltzmann relation, given by:

$$J_{\mathrm{LS}} \approx \frac{n_{\mathrm{L}} kT}{h} \exp\left(-\frac{\Delta g}{kT}\right) \exp\left(-\frac{\Delta G^*_{\mathrm{LS}}}{kT}\right) = J_0\left(T\right) \exp\left(-\frac{\Delta G^*_{\mathrm{LS}}}{kT}\right) \tag{2.12}$$

where n_{L} is the number of molecules per unit volume of liquid. Numerical values for Δg in equation (2.12) can be obtained from the literature.[68] Values for the saturated vapor pressures p_{S} and p_{L} can be found at Ref.[69]. The dependence of σ_{LS} on temperature is also known.[70] Finally, for the purposes of this section and since we do not know the shape of the ice nuclei in advance, we assume spherical nuclei; $\alpha, \beta = 1 \Rightarrow \xi = 1$ in equation (2.11). Figure 2.7 shows plots of ΔG_{LS} *vs* r for different temperatures. The critical embryo radius, r^*_{LS}, and the corresponding critical free energy, ΔG^*_{LS}, are temperature dependent. For example, a decrease in T by 5 °C, from -10 °C to -15 °C, results in 32% reduction in the critical radius, from 4.2 nm down to 2.8 nm, meaning that the colder it is, the smaller an embryo needs to be to initiate freezing.

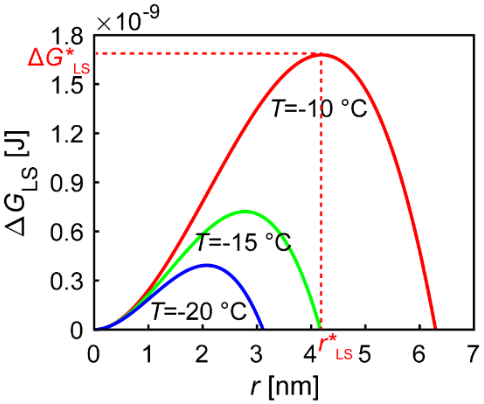

Figure 2.7 Homogeneous ice nucleation: plot of Gibbs free energy, ΔG_{LS} , *vs* critical radius, r , for different temperatures, T .

Figure 2.8 shows a plot of homogeneous nucleation rate, J_{LS} , *vs* supercooled water temperature, T (notice the logarithmic scale on the *y*-axis). J_{LS} exhibits a very strong double exponential dependence on $1/T$.

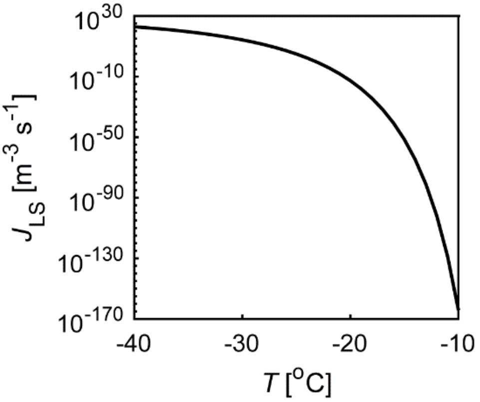

Figure 2.8 Homogeneous ice nucleation: plot of ice nucleation rate, J_{LS} , *vs* temperature, T .

Taking the same temperatures we used before as an example, we have: at $T = -10$ °C, $J_{\mathrm{LS}} \approx 10^{-165}$ m^{-3} s^{-1}, while at $T = -15$ °C, $J_{\mathrm{LS}} \approx 10^{-52}$ m^{-3} s^{-1}, which shows an extraordinary 113 orders of magnitude change in nucleation rate. Even 1 °C can lead to extreme differences in nucleation rates, meaning that every degree is important in delaying freezing. An alternative way of understanding the impact of temperature on ice nucleation is freezing delay, t_{f} , which can now be simply calculated by $1/v^{*}J_{\mathrm{LS}}$, where v^{*} is the volume of metastable water. Assuming a typical water droplet with a volume of 10 µL, at $T = -10$ °C we have $t_\text{f} \approx 10^{173}$ s, while at $T = -15$ °C, $t_\text{f} \approx 10^{60}$ s, showing – once again – the same tremendous change.

Heterogeneous nucleation. If homogeneous nucleation was the only possible mechanism of freezing, this would mean that one needs to wait for – at least – billions of years to make ice in the freezer. In reality, another mechanism is responsible for speeding up freezing, heterogeneous nucleation. In this case, the Gibbs free energy barrier for homogeneous nucleation must be modified by a numerical factor, $f \in [0,1]$, leading to:

$$\Delta G^*_\text{LS,het} = f \cdot \Delta G^*_\text{LS} \tag{2.13}$$

with f being a function of foreign particle size, contact angle of ice on the surface and lattice misfit,[66] or in other words a function of surface energy and topography. For simplicity reasons and within the concept of the present thesis, we will only investigate the effect of surface energy, and specifically contact angle. The isolated effect of ice contact angle, θ, can be calculated by the following factor:

$$f(\theta) = \frac{1}{4}\left(2 - 3\cos\theta + \cos^3\theta\right) \tag{2.14}$$

Combining equations (2.11), (2.12), (2.13) and (2.14), one can calculate the heterogeneous nucleation rate, $J_\text{LS,het}$. For example, at $T = -15$ we have: for $\theta = 150°$, $J_\text{LS,het} \approx 10^{-51}$ m^{-3} s^{-1}, for $\theta = 90°$, $J_\text{LS,het} \approx 10^{-8}$ m^{-3} s^{-1}, and for $\theta = 30°$, $J_\text{LS,het} \approx 10^{35}$ m^{-3} s^{-1}. In order to calculate the corresponding freezing delays, we can use the formula $1/\left(v^* J_\text{LS,het}\right)$, where – like above – we assume $v^* = 10$ µL. The freezing delays are $t_\text{f,het} \approx 10^{59}$ s, 10^{16} s and 10^{-27} s, respectively. Two conclusions can be drawn from these results. Firstly, when the contact angle of ice with the surface gets quite low, freezing events can occur instantaneously, here for $\theta = 30°$. Secondly, if we compare this freezing delay for heterogeneous nucleation, $\sim 10^{-27}$ s, to the corresponding value for homogeneous nucleation, 10^{60} s, we notice a tremendous difference. In fact, heterogeneous nucleation is what governs most freezing processes, and now we can understand why we can make ice in the freezer in a finite amount of time. Figure 2.9 shows plots of heterogeneous nucleation rate, $J_\text{LS,het}$, *vs* supercooled water temperature, T, for various ice–surface contact angles.

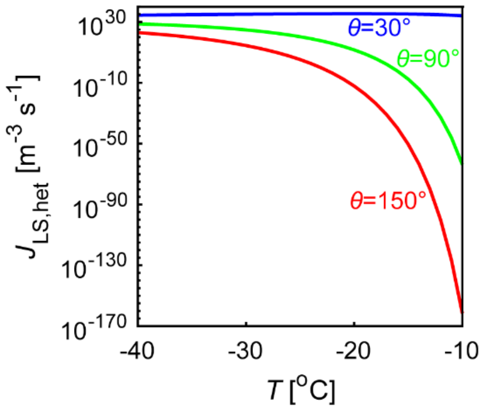

Figure 2.9 Heterogeneous ice nucleation: plot of ice nucleation rate, $J_{\mathrm{LS,het}}$, *vs* temperature, T , for different ice–surface contact angles, θ .

Figure 2.10 shows plots of freezing delay, $t_{\mathrm{f,het}}$, *vs* supercooled water temperature, T , for various ice–surface contact angles, where one can realize the significance of designing icephobic surfaces.

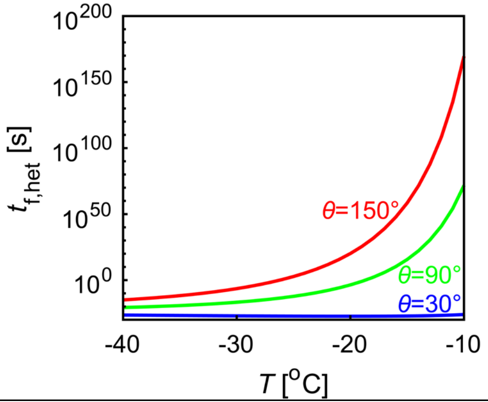

Figure 2.10 Heterogeneous ice nucleation: plot of freezing delay, $t_{\mathrm{f,het}}$, *vs* temperature, T , for different ice–surface contact angles, θ .

2.2.2. Condensation nucleation

Surface condensation is a phenomenon which appears in many practical applications and surfaces when the conditions are suitable, meaning that the surface should be colder than the surrounding moist air. This could be especially pronounced in cold climates, during humid days, and whenever a surface gets in contact with warm water vapor, such as in the vicinity of a swimming pool. Here we will show that with a few simple modifications in the equations described in ice nucleation, one can calculate the necessary quantities (condensation nucleation rate, etc.) for condensation nucleation. These modifications are mostly the outcome of replacing the L and S indices in the equations with V and L, since now we have vapor -> liquid phase transition. The critical energy barrier (Gibbs free energy) for condensation nucleation is given based on the modified equations (2.11), (2.13) and (2.14):

$$\Delta G^*_{\mathrm{VL}} = f\left(\theta_{\mathrm{W}}\right)\frac{16\pi\sigma_{\mathrm{VL}}^3}{3\left[n_{\mathrm{L}}kT_{\mathrm{S}}\ln\left(p/p_{\mathrm{L}}\right)\right]^2} \tag{2.15}$$

where σ_{VL} is the surface tension of water in contact with air, n_{L} is the number of water molecules per unit area, T_{S} is surface temperature, and the p/p_{L} ratio of partial pressures is called supersaturation (p is the water vapor pressure of the environment and p_{L} is the saturated vapor pressure over a plane surface of water at temperature T_{s}). The prefactor $f\left(\theta_{\mathrm{W}}\right)\in[0,1]$ is a function of the (liquid) water contact angle on the surface, θ_{w} , given by:

$$f\left(\theta_{\mathrm{W}}\right)=\frac{1}{4}\left(2-3\cos\theta_{\mathrm{W}}+\cos^3\theta_{\mathrm{W}}\right) \tag{2.16}$$

We will only consider the case of heterogeneous nucleation as it is the most relevant in explaining real phenomena of condensation on surfaces. Let us investigate the effect of surface energy on water condensate nucleation rate, $J_{\mathrm{VL,het}}$. Figure 2.11 shows plots of $J_{\mathrm{VL,het}}$ *vs* surface temperature, T_{S} , for various water contact angles, θ_{W} . We set the ambient temperature to 30 °C and 100% relative humidity, corresponding to $p=4200$ Pa. The prefactor in the modified equation (2.12) was taken as $J_0\approx10^{29}$ m^{-2} s^{-1}.[70] Let us now study the case of changing T_{S} by 5 °C, from 15 °C to 20 °C. At 15 °C, we have, for $\theta_{\mathrm{W}}=30°$, $J_{\mathrm{VL,het}}\approx10^{28}$ m^{-2} s^{-1}, for $\theta_{\mathrm{W}}=60°$, $J_{\mathrm{VL,het}}\approx10^{21}$ m^{-2} s^{-1}, and for $\theta_{\mathrm{W}}=120°$, $J_{\mathrm{VL,het}}\approx10^{-14}$ m^{-2} s^{-1}. At 20 °C, we have, for $\theta_{\mathrm{W}}=30°$, $J_{\mathrm{VL,het}}\approx10^{27}$ m^{-2} s^{-1}, for $\theta_{\mathrm{W}}=60°$, $J_{\mathrm{VL,het}}\approx10^{11}$ m^{-2} s^{-1}, and for $\theta_{\mathrm{W}}=120°$, $J_{\mathrm{VL,het}}\approx10^{-65}$ m^{-2} s^{-1}. We can draw two conclusions from these results. Firstly, an increase in surface temperature can lead to extremely reduced nucleation rates; for example, for $\theta_{\mathrm{W}}=120°$, we notice an extraordinary 10 orders of magnitude decrease in $J_{VL,het}$ per 1 °C temperature increase. Secondly, surface energy plays an important role in preventing condensate formation. In fact, one can see that hydrophilic surfaces are very prone to condensation nucleation, while at the same temperatures, close to ambient temperature, hydrophobic surfaces show insignificant nucleation rates.

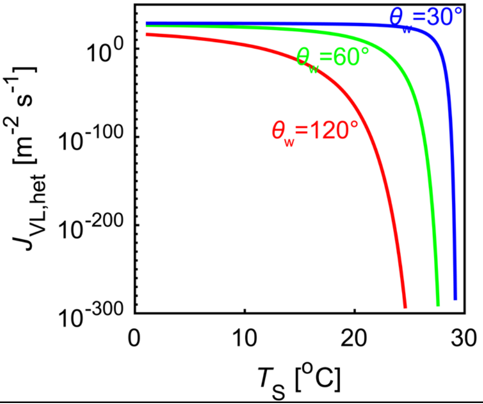

Figure 2.11 Condensation nucleation: plot of condensation nucleation rate, $J_{VL,het}$, *vs* surface temperature, T_S, for different water contact angles, θ_W.

Figure 2.12 shows plots of condensation timescales, $t_{c,het}$, *vs* surface temperature, T_S, for various water contact angles, θ_W. An area of 1 mm² was assumed.

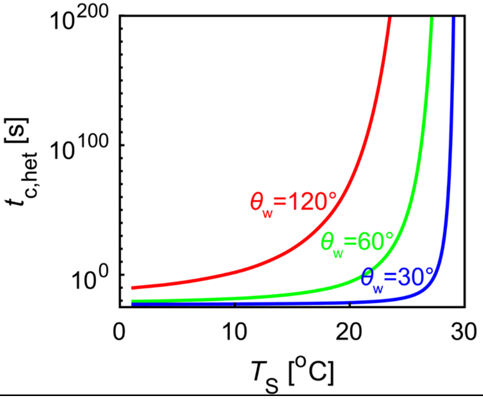

Figure 2.12 Condensation nucleation: plot of condensation time, $t_{c,het}$, *vs* surface temperature, T_S, for different water contact angles, θ_W.

Through these plots, one can realize the important contribution of surface chemistry in delaying or preventing condensation. For example, at $T_S = 20$ °C, just 10 °C below ambient, condensate is predicted to appear almost instantaneously on hydrophilic surfaces, while hydrophobic surfaces show practically no condensate. Of course, this is just a theoretical prediction, as in practice other factors such as surface structure, impurities and latent heat release of condensing water must be taken into account. This analysis is sufficient, though, to emphasize the importance of both increasing surface temperature and reducing surface energy in preventing condensation.

2.3. Principles of heating in metasurfaces

Modern technology and micro/nano-fabrication methods have led to the development of an unprecedented amount of novel approaches to solving everyday life problems while using much lower amounts of materials than in the past and maintaining the same or a higher level of functionality and durability required for commercial exploitation. From computer microprocessors to smartphones, optical components and multifunctional windows, to give a few examples, there is a common denominator, which is nanotechnology. Going one step further, one could say that with global warming and recent undesirable changes on planet Earth, the focus of research should really be on counteracting those changes by focusing on alternative ways of harvesting energy.

Within the scope of this thesis, we use sunlight as the driving force of our experiments and demonstrations. The energy per unit area that the sun can provide at peak, ~1 kW m^{-2}, is more than enough to warm up light-absorbing surfaces by at least a couple of degrees Celsius, proving to have a significant contribution in tackling problems that plague our lives, such as icing and visibility loss due to fogging. Since we solely rely on light for demonstrating anti-icing and anti-fogging capabilities, it is a good strategy to develop a capable surface, in the form of a light-absorbing coating that can be applied on a variety of substrates. In fact, this coating must fulfil a couple of requirements, such as durability and unobtrusiveness of the visibility through surfaces. In this chapter, we will discuss on the easiest way of achieving these, which is through nanotechnology and metamaterials. The chapter begins by enumerating the fundamental equations that govern the optical behavior of the lossy metamaterials we want to design, followed by why these are capable light absorbers (at least within a narrow wavelength range in the visible): localized surface plasmon resonance. We will then discuss about the ways of making this resonance more broadband, by means of creating effective media with a variety of nanoparticle sizes and random positioning, which will logically lead to the underlying mechanism of light-to-heat conversion via dissipation of electron oscillations, caused by interaction of metal nanoparticles with light, in the form of heat. This chapter takes significant inspiration from the book entitled “Optical Metamaterials: Fundamentals and Applications”, written by Wenshan Cai and Vladimir Shalaev.[71] Also, part of the theory mentioned in the following paragraphs can be found in Appendix A.

2.3.1. Optical properties of metals

Nature imposes limits on what is macroscopically possible in terms of interaction of matter with light. However, rational engineering of nanomaterials can make up for natural deficiencies, going beyond nature. This is the origin of the definition of metamaterials, which are artificial material structures getting their properties from the presence of unit structures rather than bulk materials. Metamaterials have inhomogeneity length scales much smaller than the wavelength of light, which – collectively – lead to homogenized material parameters and electromagnetic response. In fact, both the elementary units (nanoparticles or nanostructures) and their distances are below the wavelength of incident light, which means that an accurate tuning of their sizes and interparticle distances are required, since their response to light can change dramatically by tuning these parameters, as we will see in the following pages. The first demonstration of metamaterials dates back to the fourth century AD, with the Lycurgus cup, which contained embedded gold nanoparticles causing a change in color from green to red when changing from reflected light to light transmitted through the cup.[72] The continuation of the concept of metamaterials in the last century was witnessed through the work of Victor Veselago in 1968, who envisioned isotropic substances with negative values in both the dielectric constant and the magnetic permeability. John Pendry realized the metamaterials that Veselago imagined.[73] Later, the field of metamaterials went beyond negative refractive index and nowadays research takes place on a vast number of engineered nanostructures designed for targeted optical properties.[71]

As already mentioned, metamaterials exhibit homogenized responses to impinging light. Since light consists of electromagnetic radiation, two are the quantities that fundamentally describe their interaction with light, the electric permittivity, ε, and the magnetic permeability, μ. Both ε and μ can have a real and an imaginary component, depending on how strongly a metamaterial can absorb, reflect or transmit light. Other material properties, such as the refractive index, n, are direct functions of these two quantities:

$$n = \sqrt{\mu\varepsilon} \tag{2.17}$$

Typically, metals appear reflective and opaque in the visible. This is because there is no energy gap between occupied and empty states, meaning that any incoming photons with sufficient energy can lead to the excitation of electrons. Noble metals, like all metals, have a number of free electrons. However, there are also contributions from bound electrons that cause interband transitions (such as 5d to 6sp orbital in gold). These effects combined, when they take place at visible frequencies, lead to some interesting optical properties. Using the Drude model for the free electrons, the overall dielectric function (relative permittivity) of a metal particle, that contains both the free electron and bound electron contributions, can be written as:

$$\varepsilon(\omega)=\varepsilon'(\omega)+\varepsilon''(\omega)=\varepsilon_{\text{bound}}+\varepsilon_{\text{free}}=\varepsilon_{\text{bound}}+\frac{\omega_{\text{p}}^{2}}{\omega^{2}+i\omega\gamma} \tag{2.18}$$

where ω is the frequency of incoming light, ε' and ε'' is the real and imaginary part of permittivity, respectively, ω_{p} is the plasma frequency and γ is the damping constant, which is affected by size effects at low particle sizes. We will now investigate the effect of particle size (diameter, d) on the permittivity and refractive index of gold (Au) nanoparticles. Au has an electron mean free path of ~ 40 nm [74] and its selection was based on its effective visible light absorption (recall the Lycurgus cup and also see Chapter 3 and Appendix A for the rationale behind choosing Au).

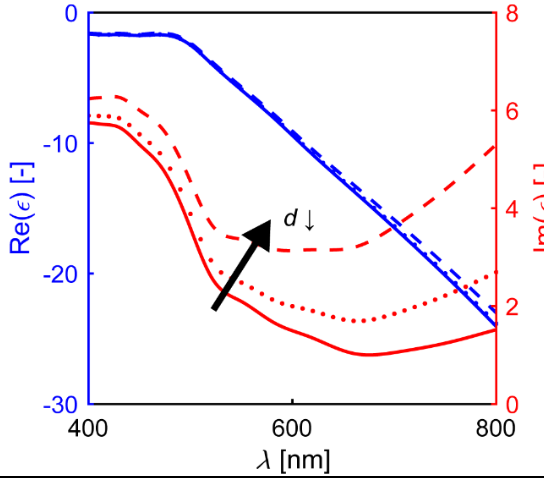

Figure 2.13 Real and imaginary parts of Au permittivity, ε, *vs* wavelength of light, λ, for bulk Au (—— and ——), and Au nanoparticles of diameter, $d = 10$ nm (· · · and · · ·) and $d = 3$ nm (− − − and − − −).

Figure 2.13 shows plots of the real (left axis) and imaginary (right axis) parts of ε for Au, *vs* wavelength of light, λ, in the cases of bulk Au as well as for small particle sizes, d, smaller than the mean free path (the relation between ω and λ is: $\omega = 2\pi c / \lambda$, where c is the speed of light). From Figure 2.13 one can see that at optical frequencies, $\mathrm{Im}(\varepsilon) = \varepsilon'' << |\varepsilon'| = |\mathrm{Re}(\varepsilon)|$, or in other words, based on equation (2.17), the imaginary part of the refractive index is very large. A reduction in d strongly affects ε'' by increasing its magnitude. Furthermore, in contrast with dielectrics (such as glass, polymers), which have a purely real and positive permittivity, Au has a highly negative real part, ε', meaning that that its free electrons oscillate out of phase with the imposed electric field. This means that the majority of impinging photons get reflected at the metal–dielectric interface. This can be proven based on the Fresnel equation, according to which the reflection coefficient is given by $(n_1 - n_2)/(n_1 + n_2)$, where the indices 1 and 2 stand for dielectric and metal, respectively. For real n_1 and imaginary n_2, the reflection coefficient should be equal to unity, therefore most of the incident light on a metal should be reflected. The large imaginary part of the refractive index also results in low penetration depths for light, called the skin depth,[71] which is why one can design an ultra-thin material system based on noble metals. How we can change from a purely reflective behavior into an absorptive one, which is mandatory if we want to heat up a surface, will be discussed in the following sections.

2.3.2. Metal–dielectric nanocomposites: effective medium theories

Up to this point, we investigated the optical properties of bulk noble metals and isolated metal nanoparticles. In an attempt to create interesting properties that go beyond metals, one can make metal–dielectric nanocomposites. The first and seemingly easiest approach is to design a system consisting of alternating periodic layers of a metal and a dielectric. The thickness of each layer has to be much smaller than the wavelength of incident light in order to describe the system with homogenized parameters. The optical properties of layered structures can be predicted by means of the transfer matrix method, in which a propagation matrix accounts for light propagation through each layer.[75] In each layer, part of the incident light can be reflected, absorbed or transmitted. However, implementation of this method requires accurate knowledge of the (complex) refractive index of each layer, which due to lack of data and size effects in thin layers, is often impractical. Also, practical fabrication limitations, such as interfacial roughness when depositing layers, dewetting of metals and impurities render the fabrication of such a system a tedious and time-consuming process.

An alternative approach is removing all well-structured building blocks and replacing them by randomly structured media, arranged in a disordered manner, while keeping the unit sizes well below the wavelength of light, leading to a microscopically heterogeneous, macroscopically uniform system. This is the effective medium approach. Two major theories exist for the homogenized, “effective” optical properties of such nanocomposites, the Maxwell-Garnett theory and the Bruggeman theory. Once again, a good proxy to the optical properties is permittivity, ε . Keeping the notation introduced before, using 1 for the dielectric and 2 for the metal inclusions, the effective permittivity of the system, according to the Maxwell-Garnett approach, is given by:

$$\varepsilon_{\text{eff}} = \varepsilon_1 \left[\left(1 + 2f \frac{\varepsilon_2 - \varepsilon_1}{\varepsilon_2 + 2\varepsilon_1} \right) / \left(1 - f \frac{\varepsilon_2 - \varepsilon_1}{\varepsilon_2 + 2\varepsilon_1} \right) \right] \tag{2.19}$$

where ε_1 and ε_2 is the permittivity of the dielectric and metal, respectively, and f is the volume fraction of the metal, the so-called volume filling factor. This theory assumes that we have a clear distinction between the metal (inclusions) and the dielectric (host), treating them in an asymmetrical manner, which is why it is only valid for $f << 1$. Another theory, which is derived by setting the spatial electric flux deviation in the nanocomposite equal to zero, comes to solve this problem. According to the Bruggeman formula:

$$\varepsilon_{\text{eff}} = \frac{1}{4} \left\{ (2-3f)\varepsilon_1 + (3f-1)\varepsilon_2 \pm \sqrt{\left[(2-3f)\varepsilon_1 + (3f-1)\varepsilon_2 \right]^2 + 8\varepsilon_1\varepsilon_2} \right\} \tag{2.20}$$

The sign of this equation is chosen so that the imaginary part of ε_{eff} remains positive.[76]

Figure 2.14 shows plots of the real and imaginary parts of ε_{eff} as a function of λ for various fill factors, $f \in [0,1]$, for a Au–TiO$_2$ nanocomposite (see Appendix A for more information on the selection of the dielectric), based on Bruggeman’s formula in equation (2.20). We can see that $\text{Re}(\varepsilon_{\text{eff}})$ generally decreases with increasing f . For low f , $\varepsilon_{\text{eff}} \approx n^2$, where n in this case is the refractive index of TiO$_2$, while for large f the nanocomposite behaves similarly to pure Au. The most interesting part of Figure 2.14, though, is the imaginary part of permittivity, $\text{Im}(\varepsilon_{\text{eff}})$. We notice that for $f = 0.2$, $\text{Im}(\varepsilon_{\text{eff}})$ increases dramatically compared to TiO$_2$; in fact, even for 20% Au, the permittivity of the nanocomposite already mostly exceeds the permittivity of Au nanoparticles in the broad wavelength range of 400–1200 nm. Starting from the opposite side in terms of concentrations, we observe that for $f \approx 1$, $\text{Im}(\varepsilon_{\text{eff}})$ resembles the permittivity of bulk Au. Interestingly, when $f \approx 0.4$, $\text{Im}(\varepsilon_{\text{eff}})$ becomes so large and broadband that it exceeds the permittivity of all other concentrations, and definitely the permittivity of gold itself.

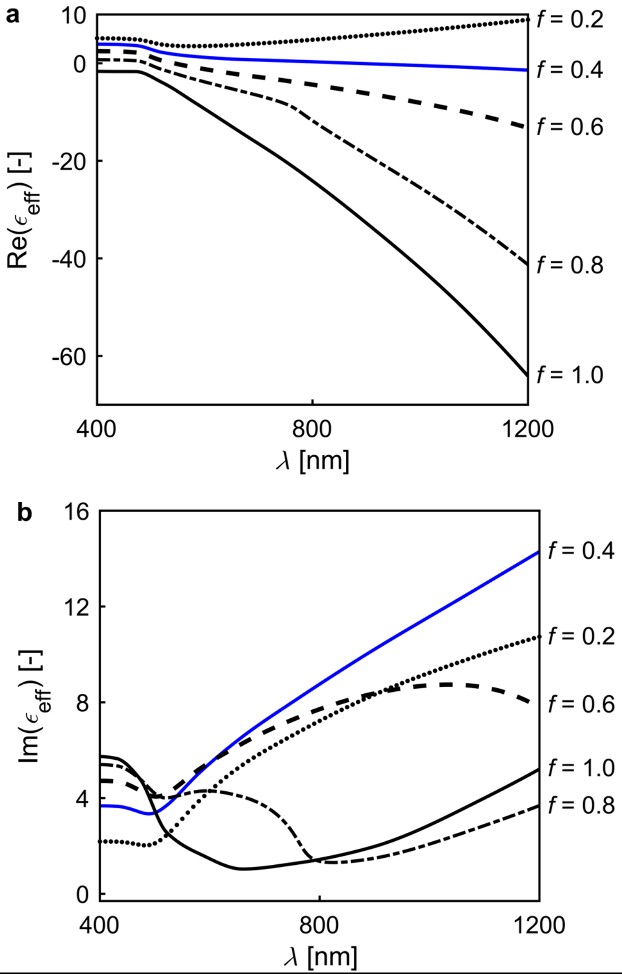

Figure 2.14 (a) Real and **(b)** imaginary parts of effective permittivity, $\varepsilon_{\mathrm{eff}}$, *vs* wavelength of light, λ, for a nanocomposite consisting of Au and TiO_2, for different Au volume filling factors, f, ranging from 0 (pure TiO_2) to 1 (pure Au).

This is because of the expected broadband resonance as one keeps packing metal nanoparticles while keeping them apart. At some concentration, one will have the maximum amount of separated nanoparticles, randomly embedded in the dielectric. This is the so-called percolation threshold, an outcome of simple geometry, which can easily be proven to be at $f = 0.33$ for a bulk nanocomposite and at $f = 0.5$ when we approach a 2D geometry. For f beyond the percolation threshold, the nanocomposite behaves more like a metal. It is exactly the high $\mathrm{Im}(\varepsilon_{\mathrm{eff}})$ close to the percolation threshold that explains why one can use metal–dielectric nanocomposites to construct metasurfaces with very low thickness and very high and broadband absorbance, as will be also discussed later.

2.3.3. Light-to-heat conversion with metasurfaces

In the previous sections, we discussed the optical properties of noble metal–dielectric nanocomposites and their unique property of extremely high $\mathrm{Im}(\varepsilon_{\mathrm{eff}})$ over a very broad wavelength range, including the whole visible spectrum. However, one first needs to understand the mechanism of light-to-heat conversion in such homogenized media on a unit cell level in order to realize how electromagnetic radiation from light can be absorbed and turn into heat, expressed as a temperature increase in a single metal nanoparticle, which is surrounded by the host medium.

Let us assume a single metal particle embedded in a dielectric. Considering a simplified band structure of metals, there are two energy states, E_1 and E_2, below and above the Fermi level, E_{F}, respectively. The difference between these two energies is too large to be simply supplied by a photon, requiring a phonon or imperfection. If or when a state transition from E_1 to E_2 occurs, two "hot" carriers are generated, an electron and its corresponding hole, in order to maintain electroneutrality. As nanofabrication methods continue to evolve and the number of defects gets reduced, other mechanisms become dominant. The first of those is a momentum-conserving mechanism, electron–electron scattering, with which two electrons transition from energy states below E_{F} to states above it. This mechanism is highly frequency-dependent, as higher photon energies result in an increased number of electron–hole pairs.[77] The second mechanism is Landau damping, and it is the dominant dissipation mode in very thin metal structures, resulting in a significant broadening of surface plasmons (coherent electron oscillations at the interface between two materials). Landau damping is the outcome of energy quantization in the individual electron energy levels and electron-hole pairs.[78] Finally, all metals exhibit band-to band transitions in the vicinity of E_{F}, leading to absorption. The band-to-band transition wavelength for Au is below 600 nm, which is the wavelength of yellow color, which is why bulk Au appears yellow. This last mechanism, in combination with Landau damping, are dominant in Au at optical frequencies. Once light energy has caused the generation of hot carriers and led to light absorption, this excess energy must be dissipated, which can happen with two thermalization mechanisms. The first is electron–electron scattering, which happens within a timescale of < 1 ps. The second is equalization of the electron temperature with the lattice temperature, which takes place in ~100 fs.[77]

Up to this point, we realized how single metal nanoparticles interact with light and heat up. Now, classical heat transfer theory can be employed to estimate the magnitude of the heating effect analytically at this single nanoparticle (NP) level. The local temperature increase around a single nanoparticle can be calculated as:[79]

$$\Delta T_{\mathrm{np}}\left(\vec{r}\right)=\frac{V_{\mathrm{np}}Q}{4\pi k_0 r} \tag{2.21}$$

where r is the distance from the center of the NP, Q is heat generation within the NP, V_{np} is the nanoparticle volume and k_0 is the thermal conductivity of the surrounding medium. Assuming that the size of the nanoparticle is much smaller than λ, Q is given by:[80]

$$Q=\frac{\omega}{8\pi}E_0^2\left|\frac{3\varepsilon_1}{2\varepsilon_1+\varepsilon_2}\right|^2\mathrm{Im}\left(\varepsilon_2\right) \tag{2.22}$$

where E_0 is the electric field amplitude of incident light, and ε_1, ε_2 are the permittivities of the dielectric and metal, respectively. We can now calculate the maximum temperature increase, which occurs at $r=R_{\mathrm{NP}}$, where R_{NP} is the nanoparticle radius, combining equations (2.21) and (2.22):

$$\Delta T_{\mathrm{NP,max}}=\frac{\omega}{3k_0 c}R_{\mathrm{NP}}^2\left|\frac{3\varepsilon_1}{2\varepsilon_1+\varepsilon_2}\right|^2\mathrm{Im}\left(\varepsilon_2\right)\frac{I_0}{\sqrt{\varepsilon_1}} \tag{2.23}$$

where I_0 is light intensity.[79] Equation (2.23) leads to two important findings. Firstly, $\Delta T_{\mathrm{NP,max}}\propto R_{\mathrm{NP}}^2$, or in other words a high temperature increase is possible when one increases the particle size (in the ideal scenario of different particles having the same permittivity). Secondly, there is dependence of $\Delta T_{\mathrm{NP,max}}$ on $\mathrm{Im}\left(\varepsilon_2\right)$, which – as we discussed before – is very large in the case of Au–dielectric nanocomposites. Let us take, for example, the permittivity value of an Au nanoparticle with $R_{\mathrm{NP}}=50$ nm and TiO_2 as its surrounding medium, at $\lambda=600$ nm. For $k_0=7.5$ W m^{-1}K^{-1} (thermal conductivity of TiO_2) and a nominal power density of 1 sun ($I_0=1000$ W m^{-2}, we have $\Delta T_{\mathrm{NP,max,50nm}}\approx 10^{-5}$ °C, while if we take smaller nanoparticles, with $R_{\mathrm{NP}}=5$ nm and 1.5 nm, we have $\Delta T_{\mathrm{NP,max,5nm}}\approx 10^{-7}$ °C and $\Delta T_{\mathrm{NP,max,1.5nm}}\approx 10^{-8}$ °C, respectively. The important message through this discussion is that having isolated Au nanoparticles is not enough for heating with sunlight. One needs more heat sources next to each other.

One question remains to be answered now, especially based on the last finding that isolated nanoparticles do not provide enough heating. This is: how much does a Au-based nanocomposite absorb? For simplicity and to avoid the more time-consuming way of solving Maxwell's equations, we will assume that we have a weakly attenuating medium. According to Beer's law, the light intensity, I, coming out of a material layer is related to its thickness via the following equation:[71]

$$I = I_0 \exp(-\alpha z) \tag{2.24}$$

where $\alpha = 4\pi \operatorname{Im}(n)/\lambda$ is the attenuation coefficient. Therefore, light transmittance is given as $T = 1 - I/I_0 = 1 - \exp(-\alpha z)$. Assuming that the nanocomposite is in contact with air, reflectance can be calculated as:

$$R = \left(\frac{1-n}{1+n}\right)^2 \tag{2.25}$$

Energy conservation dictates that absorbance, A, should be equal to $1-T-R$. Figure 2.15 shows plots of A *vs* composite thickness, z, for various volume fill factors, f.

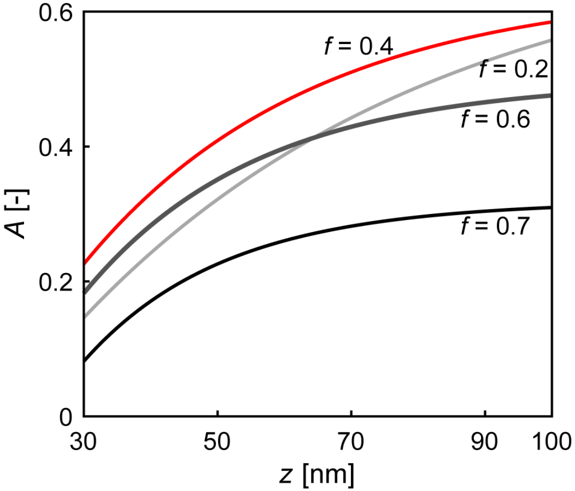

Figure 2.15 Light absorption, A, *vs* nanocomposite thickness, z, for a nanocomposite consisting of Au nanoparticles with diameter of 10 nm and TiO_2, for different Au volume filling factors, f, ranging from 0.2 to 0.7. The calculations are for constant light intensity across the wavelength range of 400–1200 nm.

The important take on message from Figure 2.15 is the one can absorb a significant fraction of the incident light within a nanocomposite layer of tiny dimensions. Furthermore, for the nanocomposite with optimum f, meaning that $\mathrm{Im}(n)$ is large over a broad wavelength range, one can expect the highest absorption level at any thickness. Further increasing f beyond the percolation threshold negatively affects A, starting to resemble the case of reflective pure Au. Definitely, the results of Figure 2.15 should be interpreted with caution, due to the number of assumptions made to extract them. It is highly suggested that one – instead – follows the rigorous approach of – numerically – solving Maxwell's equations using commercially available software and the finite time domain method. All in all, with this simple analysis, one can realize the power of nanocomposites in manipulating light in a lossy but very effective manner, paving the ground towards ultrathin unobtrusive coatings which can be used in multifunctional surfaces. Figure 2.16 shows a schematic representation of the function of such a nanocomposite, which we term "metasurface", through light-enabled collective electron oscillations and dissipation.

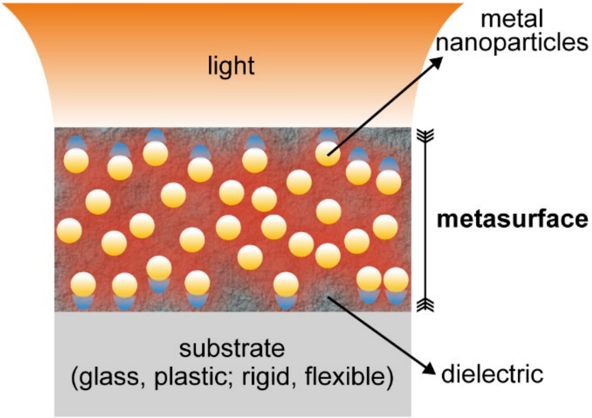

Figure 2.16 Heating in the nanoscale with light through metasurfaces.

3. METASURFACES LEVERAGING SOLAR ENERGY FOR ICEPHOBICITY

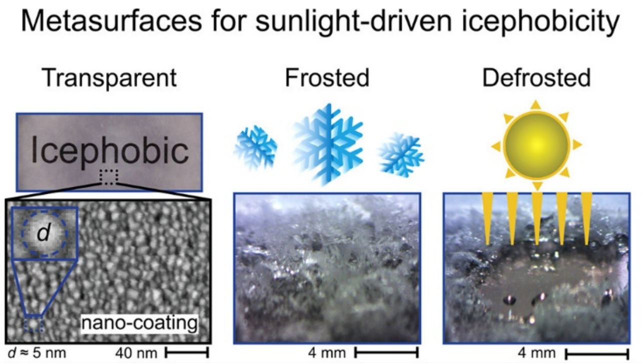

This chapter is reproduced in part with permission from:

Mitridis, E.; Schutzius, T.M.; Sicher, A.; Hail, C.U.; Eghlidi, H.; Poulikakos D.
ACS Nano. 2018, 7, 7009–7017. DOI: 10.1021/acsnano.8b02719

3.1. Abstract

Inhibiting ice accumulation on surfaces is an energy-intensive task and is of significant importance in nature and technology where it has found applications in windshields, automobiles, aviation, renewable energy generation, and infrastructure. Existing methods rely on on-site electrical heat generation, chemicals, or mechanical removal, with drawbacks ranging from financial costs to disruptive technical interventions and environmental incompatibility. Here we focus on applications where surface transparency is desirable and propose metasurfaces with embedded plasmonically enhanced light absorption heating, using ultra-thin hybrid metal–dielectric coatings, as a passive, viable approach for de-icing and anti-icing, in which the sole heat source is renewable solar energy. The balancing of transparency and absorption is achieved with rationally nano-engineered coatings consisting of gold nanoparticle inclusions in a dielectric (titanium dioxide), concentrating broadband absorbed solar energy into a small volume. This causes a >10 °C temperature increase with respect to ambient at the air–solid interface, where ice is most likely to form, delaying freezing, reducing ice adhesion, when it occurs, to negligible levels (de-icing) and inhibiting frost formation (anti-icing). Our results illustrate an effective unexplored pathway towards environmentally compatible, solar-energy-driven icephobicity, enabled by respectively tailored plasmonic metasurfaces, with the ability to design the balance of transparency and light absorption.

3.2. Introduction

Icing is very common in nature and technology, and when not controlled or alleviated, it can have very negative consequences in a broad range of applications including automobiles,[8] aviation,[7] power distribution,[9] shipping,[25] road transportation networks,[10] buildings,[11] wind energy generators[24] and photovoltaics.[81] The energy requirements, cost and environmental impact of de-icing are surprisingly high. A very common example from everyday life is automobile windshield defrosting by means of hot air, that mandates the function of the engine for up to 30 min in cold climates.[82] It is also estimated that the global aircraft de-icing market will be worth $1.30 billion by 2020,[12] while the ice protection systems are expected to amount for $10.17 billion by 2021.[13] A degree of optical transparency is a crucial property in many of these applications,[7,8,11,81] achieved by – often – multifunctional windshields and windows, constituting indispensable architectural elements of commercial and residential buildings.[83,84] Several passive anti-icing strategies, based on scientifically nano-engineered surfaces,[26,85] have been developed since the late 1990s, including hierarchical superhydrophobic surfaces,[15–21] lubricant infused surfaces,[22] and liquid infused polymers.[23] Their icephobic properties are defined by the nucleation delay, droplet contact time reduction, reduced ice adhesion and defrosting time.[15–23] While promising and highly desirable, passive approaches are to date complementary to active systems such as resistive heaters[24] and mechanical scraping.[25] Such active systems, however, are energy intensive (requiring electricity),[86] their operation is intrusive, have limited optical transparency and working temperature,[26,87] or require replenishment.[22,26] What is less explored is harvesting the potential of ubiquitous sunlight to impart icephobicity, here through specifically tailored plasmonic metasurfaces.

We show that by using rationally nano-engineered ultra-thin hybrid plasmonic metasurfaces, one can concentrate naturally occurring solar energy into a small volume, causing a greater than 10 °C temperature increase with respect to ambient at the air–solid interface, where ice is most likely to form, delaying freezing, reducing ice adhesion to negligible levels (de-icing) and inhibiting frost formation (anti-icing). Significant thermal responses can be achieved with transparent metasurfaces, paving the way to a wide range of applications where the benefit of icing resistance must be weighed against loss of transparency. We realize this by engineering an array of nanoscale noble metal particles embedded in a dielectric matrix – an approach that is shown to be capable of tuning absorption and transparency in a systematic way based on film thickness and is well-suited for a fundamental study – on industrially and commercially relevant substrates (*e.g.*, glass, plastic), for a total film thickness in the sub-micron regime, ensuring maximum temperature boost. The use of plasmonics in metal–dielectric composites in applications such as water desalination,[88] photovoltaics,[89] solar water heating[90] and photochemistry[89,91] were explored before. Plasmon resonances in metallic nanostructures can be damped radiatively (photon re-emission) or non-radiatively *via* Landau damping,[78] resulting in rapid localized heating of the nanoparticles.[89,92–94] Here, exploiting the Landau damping of hot electrons[92] in deeply sub-wavelength gold particles, and incorporating them in rationally designed metal-dielectric nanocomposite metasurfaces, we show that a broadband absorption of solar energy, with adjustable levels of absorption and transparency, can be achieved within sub-wavelength films, confined in the surface. We demonstrate that such heating can be considerable and under harsh icing conditions it can significantly delay frost formation (anti-icing) and lead to the swift removal of ice blocks from the surface (de-icing) for several freezing cycles. This is a straightforward approach that leverages naturally occurring sunlight to achieve an impressive anti-icing and de-icing performance that does not rely on chemicals, mechanical action or electricity, translating into environmental and cost savings and operational facility.

3.3. Results and discussion

We designed and fabricated plasmonic metasurfaces consisting of closely-packed, deeply sub-wavelength metal particles, in a dielectric matrix.[71,76] For the metal and dielectric, we chose gold (Au) and titanium dioxide (TiO_2), respectively. Nanoscopic gold particles are very effective absorbers of sunlight at their plasmon resonance wavelengths. Embedding them in a dielectric matrix, with a volumetric concentration close to the percolation limit, leads to a very effective and ultra-broadband absorption. This absorption is attributed to the significantly increased imaginary part of the effective permittivity, $\mathrm{Im}(\varepsilon_{\mathrm{r,nc}})$ – equivalently effective electronic conductivity – over an ultra-broad spectrum,[71] in our designed nanocomposites. The increased conductivity leads to a boost in the photoexcited hot carriers,[92] which generate heat through Landau damping.[78] The selection of TiO_2 as the dielectric is based on previous findings in which high absorption levels of over 80% across the visible wavelength range were demonstrated in Au–TiO_2 thin films. The TiO_2 enhances the plasmon resonance of individual Au nanostructures and the plasmonic coupling of proximal nanostructures, enabling broadband light absorption.[95] Other common dielectric materials, such as silicon dioxide or Teflon, are also employable, albeit using the high-refractive index TiO_2 enables enhancement of the visible light absorption (see Appendix A, section 'Modeling light absorption' and Figure A.1 for a comparison between TiO_2 and other common dielectrics).

Based on our theoretical evaluations and experimental results (discussed below), a metasurface composed of gold particles with sizes, d, of ≈ 5 nm, and a volumetric concentration, v_{Au}, of $\approx 40\%$, embedded in a TiO_2 matrix, exhibits a high level of absorption across the entire visible and near-infrared spectrum, and is the selected material system in this study.

To realize the nanocomposites, we deposited Au and TiO_2 *via* a layer-by-layer sputter deposition process, on fused silica and acrylic (PMMA) substrates. An experimental parametric study by changing the total film thickness (L) and the total number of deposited layers (N_{L}) was conducted for achieving a gold volumetric concentration, $v_{\mathrm{Au}} \approx 40\%$, and a desired level of absorption and transparency. The individual layer thicknesses of Au and TiO_2 were kept constant at 4.6 and 6.9 nm, respectively. Due to the anti-wetting properties of Au, the thin deposited gold layers formed isolated particles instead of a continuous film, effectively leading to a nanocomposite with sub-wavelength, highly-absorptive inclusions (see Appendix A, section 'Modeling light absorption' for the effect of the particle size). N_{L} was varied from 4 to 44, producing film thicknesses ranging from $L = 38 \pm 2$ nm to $L = 270 \pm 5$ nm, respectively, including a 15-nm TiO_2 top-layer that provided identical surface chemistry for all the fabricated samples. To enhance film–substrate adhesion, a 2-nm chrome layer was deposited between the substrate and the metasurfaces.

Figure 3.1a shows a picture of a plasmonic metasurface fabricated by the above procedure ($L = 270$ nm). It also details representative cross-sectional and top-view scanning electron micrographs of the coating. The cross-section consists of layers of Au nanoparticles embedded in a TiO_2 matrix (shown with arrows). The pitch between adjacent Au layers, p , is constant ($p = 11 \pm 1$ nm). To analyze the gold particle size distribution, we acquired a top-view scanning electron micrograph of an Au layer deposited on a TiO_2 layer (Figure 3.1a, bottom-right; 8-layer metasurface, $L = 45$ nm, without a TiO_2 top-layer). Figure 3.1b shows a histogram of the number of Au nanoparticles, N , normalized by the total number of particles, N_0 , *vs* their equivalent diameter, d , assuming spherical particles. We found that the particle size has a gamma distribution with a mean value of 5.4 nm, variance of 2.1 nm and a range of 7.9 nm. The methodology of the particle size analysis is described in Appendix A, section 'Nanoparticle size analysis'; see also Figure A.2. In Figure 3.1c, the transparency of the metasurface (here, $L = 60$ nm) relative to a control sample is demonstrated. The metasurface was placed on top of a printed logo and illuminated with white light on the back side. Figure 3.1d shows the normalized light absorption spectra, $\mathcal{A}$, *vs* wavelength of light, λ , for four metasurfaces with $L = 38$ nm, 60 nm, 95 nm, and 270 nm (wavelength range of 400–800 nm). The mean absorption can be calculated as: $\overline{\mathcal{A}} = \left[\int_{\lambda_{\min}}^{\lambda_{\max}} \mathcal{A}(\lambda) d\lambda \right] / \left(\lambda_{\max} - \lambda_{\min} \right)$, where $\lambda_{\min} = 400$ nm, and $\lambda_{\max} = 800$ nm. From Figure 3.1d we can see that the metasurfaces absorb light broadly across the visible spectrum and have a mean absorption value of $\overline{\mathcal{A}} =$ 28%, 37%, 63%, and 83% for $L =$ 38 nm, 60 nm, 95 nm, and 270 nm, respectively, indicating the tunability of $\overline{\mathcal{A}}$ with L . The broadband absorption is a result of the small sizes of the nanoparticles ($d << \lambda$) and their collective behavior (p and d are comparable) in the nanocomposite with a volumetric concentration close to the percolation limit. Figure 3.1e shows a plot of the normalized transmission spectra, $\mathcal{T}$, *vs* λ , for the same four nanocomposites used in Figure 3.1d. Here we see that for $L =$ 38 nm, 60 nm, 95 nm, and 270 nm, $\overline{\mathcal{T}}$ =51%, 36%, 15%, and 2%, designating also the tunability of $\overline{\mathcal{T}}$ with L . Information regarding the individual reflection and transmission spectra can be found in Appendix A, section 'Optical spectroscopy' and Figure A.3. Figure 3.1f shows the spectra of the absorbed, $\mathcal{A} \cdot I_r$, and transmitted, $\mathcal{T} \cdot I_r$, sunlight (standard solar irradiance at sea level) *vs* λ , for the partially transparent metasurface with $L = 60$ nm. Also shown is the reference standard solar irradiance, I_r ($\mathcal{A} = 0\%$ and $\mathcal{T} = 100\%$). This nano-engineered metasurface exhibits a good balance of transparency and absorption, all within a deeply-subwavelength film.

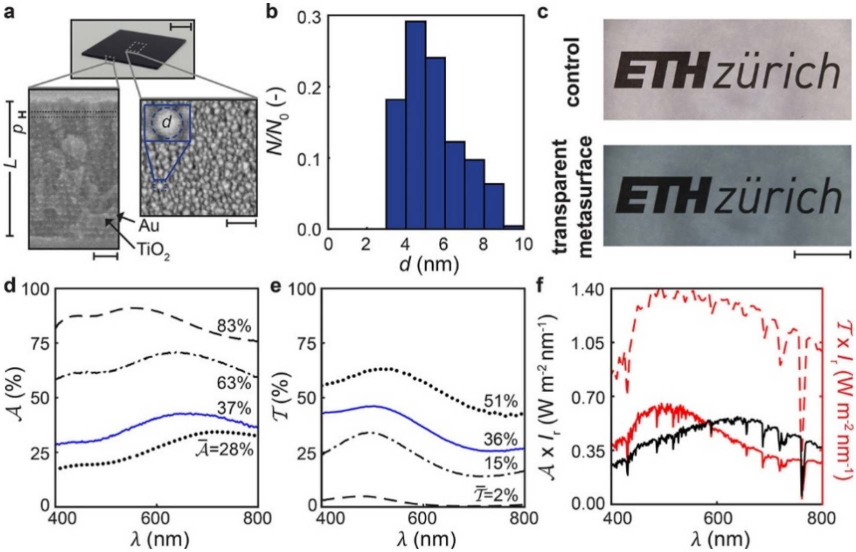

Figure 3.1 Characterizing the topography and optical properties of the plasmonic metasurfaces. (a) Macroscopic (top-row) and microscopic (bottom-row) images of a metasurface; cross-sectional (bottom-left; $L = 270$ nm, $p = 11$ nm) and top-view (bottom-right; $L = 45$ nm) micrographs of the metasurface. Bright regions ($L = 45$ nm, obtained with backscattered and secondary electrons) correspond to gold nanoparticles. The volumetric concentration of gold is $\approx 40\%$. Sample surface is 18 mm by 18 mm. **(b)** Relative frequency of gold nanoparticles, N / N_0, *vs* nanoparticle diameter, d (sample properties: $L = 45$ nm, $p = 11$ nm). **(c)** Demonstration of the transparency of the metasurfaces (here, $L = 60$ nm), *vs* a control sample, placed on a printed logo and under white backlight illumination. **(d)** Normalized absorption, $\mathcal{A}$, and **(e)** normalized transmission, $\mathcal{T}$, *vs* wavelength of light (400–800 nm), λ, for films with varying L: 38 nm (• • •), 60 nm (——), 95 nm (• – •), and 270 nm (– – –). **(f)** Absorbed, $\mathcal{A} \cdot I_r$ (——), and transmitted, $\mathcal{T} \cdot I_r$ (——), sunlight (standard solar irradiance), *vs* λ, for a metasurface ($L = 60$ nm) and reference sample ($\mathcal{A} = 0\%$, $\mathcal{T} = 100\%$, – – –). Scale bars: **(a)** top-row, 5 mm; bottom-left, 50 nm; bottom-right, 30 nm; **(c)** 2 cm.

Figure 3.2a shows a schematic of the experimental setup we used to characterize the temperature change of the nano-engineered metasurfaces (deposited on glass substrates) due to visible light illumination. For illumination we used a halogen light source, which we collimated and focused on the metasurfaces. (See Appendix A, section 'Thermography' and Figure A.4 for further information on characterizing plasmonically enhanced light absorption heating.) The temperature increase in the metasurface relative to ambient, ΔT , was measured with a high-speed infrared camera (spectral range of 1.5 to 5.1 µm). The focused light diameter, D , was 6.0 ± 0.3 mm and the power density, P , was 2.4 ± 0.2 suns (kW m^{-2}). We used a mechanical shutter to rapidly control illumination. Figure 3.2a (inset) also shows the spectrum of the broadband light source used in this study. Figure 3.2b shows ΔT *vs* time, t , for the four samples with different values of $\overline{\mathcal{A}}$ (28%, 37%, 63%, and 83%). Time-zero was when the metasurface was first illuminated. Here, ΔT was measured at the center of the illuminated area on the surface. It is clear that all metasurfaces exhibit an appreciable change in temperature due to visible light illumination, valid even for the highly transparent metasurfaces. We also note that there are transient and steady-state regimes for ΔT . ΔT *vs* t curve is also shown for the reference sample (uncoated glass substrate). Figure 3.2c shows the corresponding spatial distributions of ΔT for the four metasurfaces at $t = 180$ s (steady state). The boundary of the illuminated area is marked with a dashed circle, and it is evident that the maximum value of ΔT occurs at the center of this area and that heat diffuses well beyond the illuminated area.

The time to steady state is controlled by the characteristic length, $L_{\mathrm{C}} = \left(L_2 - D\right)/2$, and the substrate thermal diffusivity, α , where L_2 is the side-length of the square sample. This time can be estimated as $L_{\mathrm{C}}^2 / \alpha$. Substituting appropriate values yields $\left(6\ \mathrm{mm}\right)^2 / 0.43\ \mathrm{mm}^2\ \mathrm{s}^{-1} \approx 84$ s, which is comparable to the order of magnitude of the experimentally determined time (≈ 100 s). The temperature increase at the surface of the sample is determined by light irradiance and absorption as well as heat losses due to conduction (in the film and substrate), convection (in the surrounding air), and radiation (to the surrounding environment); see Appendix A, section 'Heat Transfer' and Figure A.5 for a detailed analysis on the above. In summary, to understand the relative importance of convection and radiation on determining the steady-state value of ΔT , we solved for the temperature distribution (sample with $\overline{\mathcal{A}} = 37\%$) in a two-dimensional semi-infinite plate immersed in a gas that had a heated gas–substrate interface and an adiabatic condition on its bottom interface. The boundary condition at the interface was modified to account for radiation losses. We fixed a value of emissivity ($\varepsilon \approx 0.8$), based on the infrared measurements of ΔT , and varied the position of T_∞ (aspect ratio of L_1 / L_2) until $T_{\mathrm{s}} - T_\infty$ (the temperature difference between the gas–substrate interface and the gas very far away) matched our experimentally determined value of ΔT . Based on the steady-state value of ΔT that we measured, we have determined that the percentage of cooling due to radiation is a mediocre 4% of the amount of heat provided by illumination, but it can also exceed 25% in certain cases and metasurfaces (see Appendix A, section 'Heat Transfer'). To understand the importance of natural convection on cooling, we computed the Rayleigh number, $Ra_{L_1} = g\beta\Delta T L_1^3/(\nu\alpha)$, where g is the acceleration due to gravity, β is the expansion coefficient ($1/T$ for an ideal gas), and ν is the kinematic gas viscosity. Below and above a critical value of Ra_{L_1}, $Ra_c = 1708$,[96] heat transfer is in the form of conduction and advection (convection and conduction), respectively. Substituting appropriate values, we see that the value of Ra_{L_1} in this case is $7\cdot10^{-3}$ ($Ra_{L_1} \approx 7\cdot10^{-3}$ for $T_\infty = 23$ °C, $P \approx 2.4$ kW m^{-2}, $\overline{\mathcal{A}} = 37\%$, $\Delta T \approx 7$ °C, $L_1/L_2 \approx 1.2\cdot10^{-2}$, $\nu = 1.57\cdot10^{-5}$ m^2 s^{-1}, $\alpha = 22.07\cdot10^{-6}$ m^2 s^{-1}, $L_1 = 212$ µm, $\beta = 3.38\cdot10^{-3}$ K^{-1}, $g = 9.81$ m s^{-2}).[97] Therefore, due to the fact that $Ra_{L_1} < Ra_c$, we conclude that heat transfer through conduction is the dominant mechanism and natural convection can be neglected.

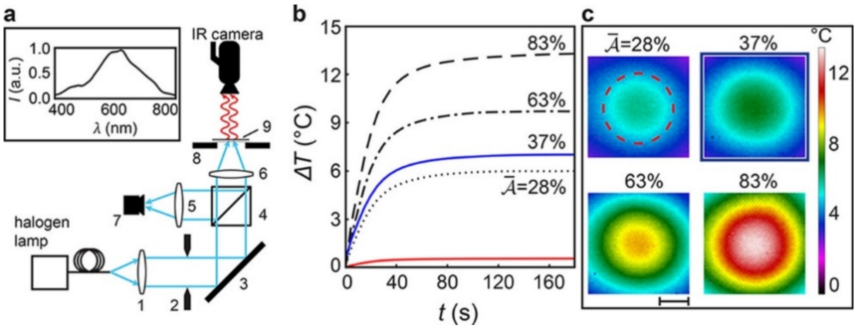

Figure 3.2 Characterizing the heating behavior of the plasmonic metasurfaces (fused silica substrate) due to visible light exposure. (a) Schematic of the setup used to characterize the thermal response of the metasurfaces due to illumination: 1, collimating lens; 2, mechanical shutter; 3, silver mirror; 4, beam splitter; 5,6, focusing lenses; 7, CMOS camera; 8, sample holder; 9, sample. The spectrum of the broadband light source (——) is shown in the inset. **(b)** Temperature change, ΔT, *vs* time, t, for metasurfaces with varying values of $\overline{\mathcal{A}}$ (28% • • •; 37% ——; 63% • – •; 83% – – –) and a control substrate (——) after illumination ($P \approx 2.4$ kW m^{-2}); time-zero is defined as the moment that the mechanical shutter was opened. **(c)** Spatial distribution of ΔT at steady state (t = 180 s). The dashed circle represents the illuminated area, with a diameter of $D \approx 6$ mm. Scale bar: **(c)** 2.5 mm.

Figure 3.3a shows a schematic of the experimental setup used to investigate the effect of illumination (halogen lamp; $D = 6.0 \pm 0.3$ mm, $P = 2.4 \pm 0.2$ kW m^{-2}) on film–ice adhesion (de-icing), on each metasurface, which was held in place by a holder on an x-y piezo stage. A hydrophobic cylinder (inner radius of $R = 1.5$ mm), filled with water, was placed on top of it, concentrically to the illuminated area. The experiments took place at $T=-4$ °C: a pin connected to a piezoelectric force sensor was initially pressed at the base of the frozen ice cylinder parallel to the x-axis inducing a shear stress, τ_{yx}. (The value of τ_{yx}, $\tau_{yx}=90\pm5$ kPa, was selected to be close to, but less than, the mean ice adhesion strength of a PVDF-coated substrate, 131 ± 19 kPa; 3 experiments, in order to prevent premature detachment of the ice cylinder.) Illumination was switched on with a mechanical shutter at $t=0$ and τ_{yx} *vs* t was recorded. The temperature of the chamber was controlled by flowing cold nitrogen gas. All the samples were coated with a thin PVDF top-layer prior to the experiments, to ensure identical wetting properties (see Methods for details). The PVDF protective films exhibit very high optical transparency due to their sub-micron thickness. Moreover, they can act as single-layer anti-reflection coatings. This can be clarified by considering the relationship $n_{\mathrm{ar}}=\sqrt{n_{\mathrm{air}}n_{\mathrm{TiO_2}}}$, where n_{ar} is the refractive index of the single-layer anti-reflection coating, $n_{\mathrm{air}}\approx1$ is the refractive index of air and $n_{\mathrm{TiO_2}}\approx2.5$ is the refractive index of the enclosing TiO_2 layer of the metasurface in the visible wavelength range. This leads to the desired refractive index of the anti-reflection coating of $n_{\mathrm{ar}}\approx1.6$, which is close to the refractive index of PVDF, $n_{\mathrm{PVDF}}\approx1.35$.[95] Therefore, upon top-side illumination, we expect that the PVDF layer decreases the reflectivity on the top side of the surface, thus boosting the level of absorption and the plasmonic heating. This was also confirmed experimentally for a PVDF-coated partially-transparent metasurface with $L\approx60$ nm, resulting in $\overline{\mathcal{A}}=41\%$, *vs* $\overline{\mathcal{A}}=34\%$ for the same uncoated metasurface (see Appendix A, section "Optical spectroscopy" and Figure A.3 for the effect of the protection layer on the absorption, reflection and transmission of the metasurfaces). In our experiments, though, where bottom-side illumination is used, since the incident light does not pass through the PVDF layer before impinging on the metasurface, the levels of absorption and the plasmonic heating should not change considerably in the presence of the PVDF top-layer.

Figure 3.3b shows a plot of τ_{yx} *vs* t for the illuminated metasurface ($\overline{\mathcal{A}}=37\%$, blue line) and control (black line) samples, for several de-icing cycles. The gray and blue shaded regions surrounding the blue (metasurface, 9 experiments) and black (control, 3 experiments) lines, respectively, are the minimum and maximum values of τ_{yx} observed during the experiments. Two regimes appear for the metasurface: almost constant τ_{yx} (prior to illumination) and sharply decreasing τ_{yx} (during illumination) until reaching the minimum measurable stress (2.5 ± 1.0 kPa). For the control case, there is only one regime with constant τ_{yx}. Figure 3.3c shows boxplots of de-icing times (*i.e.* time elapsed from $P>0$ kW m^{-2} until $\tau_{yx}\approx0$), t_{d}, *vs* $\overline{\mathcal{A}}$, at $T=-4$ °C. The mean de-icing times were 394 ± 211 s, 264 ± 80 s, 76 ± 18 s and 34 ± 11 s, for metasurfaces with $\overline{\mathcal{A}}=$ 28%, 37%, 63% and 83% respectively. From the graph, it is evident that there is an order of magnitude decrease in the de-icing time by increasing the amount of solar energy that is absorbed (metasurfaces with $\overline{\mathcal{A}} = 28\%$ *vs* $\overline{\mathcal{A}} = 83\%$). For more information on the setup and calibration process of the force sensor, see Appendix A, section 'Ice adhesion setup' and Figure A.6. In the above, complete de-icing was achieved in all cases, which we attribute to the formation of an intervening melt layer at the surface. We ascribed the de-icing time, t_d, and the gradual reduction of τ_{yx} with time to the formation of a melt layer at the center of the ice–film contact area (warmest region) and subsequent radial outward propagation of the phase boundary towards the edge (coldest region). For considerations on the effect of viscous and capillary forces in resisting the ice–block motion, which we found to be insignificant relative to ice adhesion, see Appendix A, section 'De-icing analysis'.

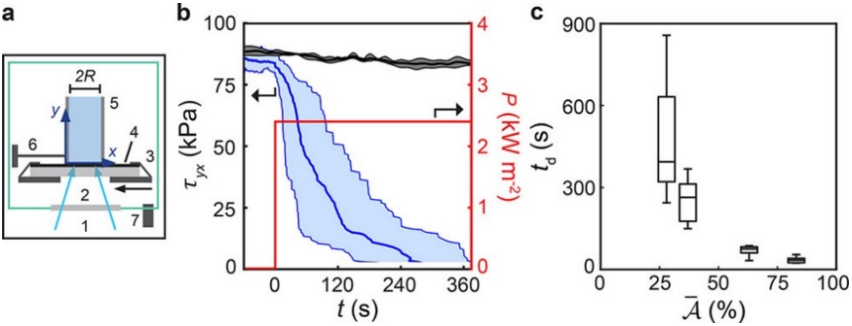

Figure 3.3 Effect of visible light illumination on surface–ice adhesion. (a) Schematic of the setup used for measuring ice adhesion: 1, visible light illumination path, same as in the infrared temperature measurements; 2, glass window; 3, piezo-stage and sample holder; 4, sample; 5, non-wetting ice cylinder, with an inner radius of $R = 1.5$ mm; 6, piezoelectric force sensor (0–2 N, in-house calibration) and force transfer pin; 7, cold nitrogen vapor inlet. **(b)** De-icing curve (shear stress, τ_{yx}, *vs* time, t) of the sample with $\overline{\mathcal{A}} = 37\%$ (——). At $t = 0$ the sample was illuminated. The corresponding τ_{yx} *vs* t of a control sample (——) is also shown. The shaded areas show the minimum and maximum of the experimental measurements. **(c)** Boxplots of de-icing time, t_d (time from maximum $\tau_{yx} \approx F_\mathrm{max} / \left(\pi R^2\right)$ to noise level), *vs* mean absorption, $\overline{\mathcal{A}}$, of the metasurfaces. The substrate was fused silica.

Figure 3.4a shows the cold chamber – integrated with the visible light illumination system – that was used to characterize the plasmonically enhanced light absorption heating in a partially transparent metasurface ($\overline{\mathcal{A}} = 37\%$, $L = 60$ nm) at sub-zero temperatures. For this part of the work, we chose to deposit the metasurface onto a thermally insulating substrate, poly(methyl methacrylate) (PMMA, $k_s = 0.2$ W m^{-1} K^{-1}, $l = 1$ mm), in order to minimize thermal losses due to conduction. Both the control and metasurface were coated with a thin layer of PVDF (transparent) to ensure that the surface chemical composition is similar.

Next, we characterize the freezing behavior of a single supercooled water droplet on the illuminated control and metasurface. We ran the experiments by first placing the coated substrate on the sample holder. Then, we turned on the light source and focused it on the metasurface ($D \approx 6$ mm, $P \approx 2.4$ kW m^{-2}). Boiling liquid nitrogen was then flowed throughout the chamber to cool it down. We continuously measured the environmental gas (T_1) and surface (T_2) temperatures. To run the droplet freezing experiment, we first set $T_1 \approx -26$ °C. Then, a single water droplet, initially at room temperature, was deposited on the substrate at the center of the illuminated spot. Figure 3.4b–c shows representative side-view image sequences of a water droplet on a (b) control and (c) metasurface cooled down at a rate of ≈ 1 °C min^{-1}, until spontaneous nucleation and freezing. This transition is characterized by a sudden change from a transparent to opaque droplet state (recalescent freezing[98]). Also indicated are the time, t, and T_1. Time-zero was considered as the time moment at which the droplet is in thermal equilibrium with the environment (to ensure that, we waited ≈ 5 min after droplet placement and the light was switched on). The change in droplet volume during the experiments was relatively small and we estimated it to be $< 5\%$ h^{-1}. We define the environmental gas temperature just prior to freezing as T_1^*. The metasurface freezes at a much lower T_1^* compared to the control ($t = 910$ s, $T_1^* = -48$ °C, *vs* $t = 230$ s and $T_1^* = -33$ °C). Figure 3.4d shows a plot of T_2 *vs* T_1 for the control (—) and metasurface (- - -). We see that the metasurface has a significantly higher temperature relative to the control case for a range of sub-zero temperatures (-53 to 30 °C). Figure 3.4e shows a plot (calibration curve) of T_1^* *vs* sample type (metasurface and control). For the control and metasurface, we measured T_1^* to be -34 ± 2 °C (16 experiments) and -47 ± 3 °C (14 experiments), respectively. It is clear that there is a significant difference in T_1^* for the two cases – which has equally significant implications in the freezing delay time (explored next) – that we can clearly attribute to the heating effect due to illumination.

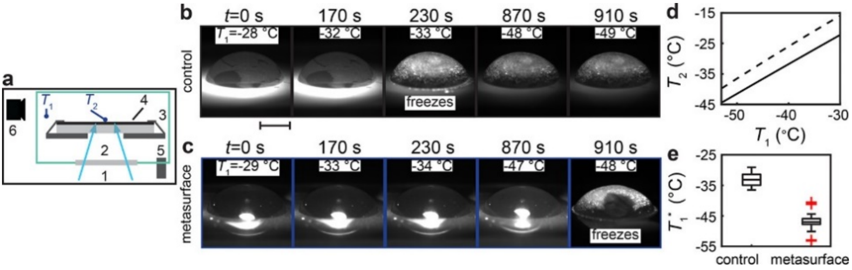

Figure 3.4 Nucleation temperature of illuminated droplets. (a) Schematic of the environmental chamber used: 1, visible light illumination path; 2, glass window; 3, sample holder; 4, sample; 5, cold nitrogen vapor inlet; 6, CMOS camera. Two temperature sensors measured the gas (T_1) and sample (T_2) temperature. The illumination power density was $P \approx 2.4$ kW m^{-2}. Side-view image sequences of water droplets on a **(b)** control and **(c)** metasurface ($\overline{\mathcal{A}} = 37\%$) cooled down at a rate of ≈ 1 °C min^{-1}; the final frames are when the droplets spontaneously nucleated and the second stage of freezing was progressing. The chamber gas temperature, T_1, is also shown. **(d)** Calibration curve: metasurface temperature, T_2, *vs* gas temperature, T_1, in the case of the control (——) and metasurface (– – –). **(e)** Gas temperature at the moment of freezing, T_1^*, *vs* sample type (control and metasurface). The substrate was PMMA. Scale bar: **(b)–(c)** 3 mm.

To understand the significance of these results, we can use the classical nucleation theory.[16,66] We term the supercooled water droplet temperatures on an illuminated control and metasurface as $T_{\mathrm{d,0}}$ and T_{d}, respectively. If we assume that $T_2 \approx T_{\mathrm{d,0}}$ and $T_2 \approx T_{\mathrm{d}}$ on the respective samples, and we set $T_1 \approx -34$ °C, then we have $T_{\mathrm{d,0}} = -26$ °C and $T_{\mathrm{d}} = -20$ °C (from the calibration curve). In the case of the control sample, $T_{\mathrm{d,0}} = -26$ °C is the spontaneous nucleation temperature, T_{N}. The difference in droplet temperatures is then defined as $\Delta T = T_{\mathrm{d}} - T_{\mathrm{d,0}}$. Previously, it was shown that $\Delta T \propto \log_{10}\left(t_{\mathrm{av}}\right)$, where t_{av} is the average time required for ice to nucleate in a supercooled droplet when the droplet is maintained at thermal equilibrium with its surroundings;[16] therefore, for a six degree temperature difference, one can expect a six orders of magnitude increase in t_{av} for the metasurface relative to the control case, which is associated with a very pronounced freezing delay. See also Appendix A, section 'Frosting characterization', Figure A.7 and Figure A.8 for frosting experiments in harsh environmental conditions: ambient humidity and high heat flux to the substrate.

Next, the defrosting potential of the partially transparent metasurfaces is investigated. Figure 3.5a–b shows an image sequence of a (a) frosted control sample and (b) metasurface ($\overline{\mathcal{A}} = 37\%$) samples (substrate: PMMA, $l = 1$ mm) in a cold dry environment ($T_1 = -16$ °C to -15 °C) that are illuminated with a halogen lamp ($P \approx 2.4$ kW m^{-2}) for $0 \le t \le 600$ s. Figure 3.5a shows that the frost on the control sample is unaffected by illumination, while Figure 3.5b shows that the metasurface is completely defrosted at the illuminated area by $t = 140$ s. To eliminate the effects of surface composition on frost growth, both the control and metasurface were coated with a thin layer of PVDF. Frost was grown on both samples under identical environmental conditions and for the same duration, ensuring similar frost thicknesses. Due to the lower thermal conductivity and increased thickness of the PMMA substrate relative to the glass, we should expect that heat transfer into the sample holder should be minimized. Furthermore, we note that there is an insulating frost layer on top of the sample; therefore, one should expect a higher steady-state temperature increase in the illuminated metasurface, allowing defrosting to occur in-spite of the relatively cold surrounding environment.

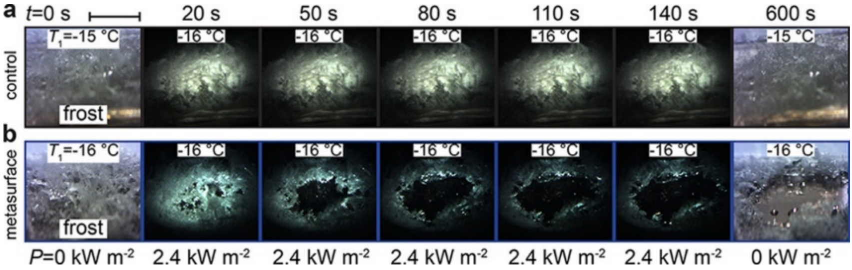

Figure 3.5 Light-induced defrosting. Angled-view image sequences of frosted PVDF-coated **(a)** control and **(b)** metasurface ($\overline{\mathcal{A}} = 37\%$) samples that were illuminated with a halogen lamp ($P \approx 2.4$ kW m^{-2}) for $0 < t < 600$ s. At $t = 0$ s and $t = 600$ s, the samples were in ambient light conditions, revealing the frost before and after illumination. The chamber gas temperature, T_1, is also shown. The substrate was PMMA. Camera tilt angle was ≈ 25 °. Scale bar: **(a)–(b)** 4 mm.

3.4. Conclusions

In closing, we showed that with rationally designed hybrid metamaterial films that balance transparency and absorption, extreme icephobic surface performances can be achieved. Such films, here nanocomposites of gold and titanium dioxide, exhibit broadband visible light absorption, while being sub-wavelength thin, enabling localized ice melting at the film–ice interface. The plasmonically enhanced light absorption heating induced a temperature increase greater than 10 °C, compared to a control surface, for rapid de-icing within 30 s. Furthermore, we achieved a 6 °C decrease in the spontaneous nucleation temperature (resulting in ≈ 6 orders of magnitude increase in droplet freezing delay at -32 °C), and a defrosting time of ≈ 4 min, for a highly transparent metasurface ($\overline{\mathcal{A}} = 37\%$, $\overline{\mathcal{T}} = 36\%$). We presented a viable, passive, anti-icing and de-icing metamaterial platform harvesting the benefit of solar radiation, that can find a broad range of applications, especially where transparency is required, including water solar heating, automotive industry, residential and commercial buildings and construction or machinery infrastructure. We believe that although the present approach demonstrates both anti-icing and de-icing behavior while maintaining transparency, it could be further improved by incorporating other passive icephobicity designs based on surface nanoengineering.[15–23]

3.5. Methods

Substrate preparation. Double side polished, 4-in fused silica wafers ($l = 500$ µm) were sourced from UniversityWafer, Inc. A 5-µm protective photoresist layer was spin coated and developed on each wafer, which was subsequently cut into 18 mm by 18 mm square pieces, using an ADT ProVectus LA 7100 semi-automatic wafer dicer. The cut glass substrates were sonicated in acetone for 3 min, in order to remove the photoresist, followed by an equal-time sonication in isopropyl alcohol. Finally, they were dried in a nitrogen stream. PMMA substrates were prepared by manually cutting a PMMA sheet (Schlösser GmbH, $l = 1$ mm) into rectangular pieces ($\approx$ 18 mm by 18 mm), removing the protective membrane and sonicating in water.

Adhesion layer and thin film deposition. A 2-nm chrome adhesion layer was deposited on the substrates, using an Evatec BAK501 LL thermal evaporator. The multilayer structure was then applied layer-by-layer *via* sputter deposition in argon atmosphere, by employing a Von Ardenne CS 320 C sputter tool. An RF field at a power of 600 W was used at the TiO_2 target, while a 50 W DC field was used in the case of the Au target. Deposition times were 43 s and 3 s, respectively, at a pressure of 6 µbar. A pre-sputtering time of 30 s was necessary for stabilizing the plasma and thus the deposition rate in the chamber. The first layer was TiO_2, followed by Au, and the alternation continued until the desired number of layers was reached. The deposition time for the TiO_2 top-layer was 72 s.

Film characterization. The samples were cleaved after scratching the glass substrate with a diamond tip on two opposite sides. Film thickness was extracted from cross-sectional images of the metasurface with $L = 270$ nm (44 layers), taken by a FIE

Nova NanoSEM 450 scanning electron microscope, at an acceleration voltage of 2 kV. This approach also gave us a visualization of the cross-sectional particle distribution of the same metasurface. In the case of the top-view image of the Au nanoparticles (8-layer metasurface, $L = 45$ nm), acceleration voltage was 0.5 kV. For the particle size distribution (equivalent diameter) analysis of the top-view image, ImageJ and MATLAB software packages were employed. Light absorption measurements took place in two steps: the optical transmission, $\mathcal{T}$, and reflection, $\mathcal{R}$, spectra of the metasurface were individually recorded at the same spot on the sample, over the 400–800 nm wavelength range, by a UV–Visible spectrometer (Acton SP2500, Princeton Instruments), making the assumption of negligible light scattering. The absorption spectra were obtained by $\mathcal{A} = 1 - \mathcal{R} - \mathcal{T}$. Measurements from three different spots per sample were averaged to extract the absorption curves in Figure 3.1d and Figure A.3a–d.

Polymer protective coating and characterization. A polyvinylidene fluoride (PVDF) protective layer was spin coated (Laurell WS-400B-6NPP/LITE) on top of the metasurfaces deposited on fused silica substrates, to minimize surface–ice interactions and provide mechanical durability. For this purpose, a PVDF solution (4 wt.%) in N,N-dimethylformamide (DMF) was prepared under rigorous stirring for 2.5 h. After cleaning the sample with acetone, under sonication, and isopropyl alcohol, the solution was spin coated (30 s at 3000 rpm) onto it, and then it was heated for 3 h at 200 °C, over the melting temperature of PVDF, to reduce surface roughness. The supplier of the PVDF (beads, $M_w \approx 180{,}000$) and DMF (anhydrous, 99.8%) was Sigma-Aldrich Co LLC. Advancing and receding water contact angle measurements were performed in a OCA 35 goniometer (DataPhysics), using the inflation/deflation technique (droplet volume of 8–10 μL), equal to $86.7 \pm 0.9\,°$ (advancing) and $73.0 \pm 1.3\,°$ (receding). The respective contact angles of a PVDF-coated only control substrate were $87.9 \pm 0.5\,°$ and $72.3 \pm 0.9\,°$. In the case of metasurfaces on PMMA substrates, a similar process to the ones on fused silica was followed, with the differences of only cleaning with sonication in water and heating up to 80 °C for 3 h (below the glass transition temperature of PMMA). A 4 wt.% PVDF solution in NMP (anhydrous, 99.5%, Sigma-Aldrich Co LLC) was used in this case.

Simulation software. MATLAB software suite was used to estimate the imaginary part of electric permittivity of our nanocomposite films. The heat transfer simulations were performed numerically in COMSOL Multiphysics Modeling Software.

IR thermal response measurements. The transient thermal response of the unprotected metasurfaces on fused silica substrate ($l = 500$ μm), as well as the one of an uncoated reference fused silica substrate, were measured by means of an infrared camera (FLIR SC7500, 1.5–5.1 um), equipped with a 50 mm F/2 lens, within 320 by 256 pixels (pixel pitch: 30 µm), at a framerate of 50 fps. A visible light illumination source (FLEXILUX 600 Longlife) consisting of a 50 W halogen lamp and a 5-mm diameter gooseneck fiber constituted the power source for the illumination of the samples. Light from the bottom side (substrate), was collimated and focused on the top-surface with two convex, 2-in lenses, using a Thorlabs monochrome CCD camera (DCC1545M-GL). The light spot had a diameter of 6.0 ± 0.3 mm, corresponding to a maximum power density of 2.4 ± 0.2 kW m^{-2} (suns), measured with a Thorlabs S301C, 0.19–25 µm power meter. For calculating the emissivity of the samples, these were heated up on a hot plate to three discrete elevated temperatures, while the hot plate was kept at a low angle (less than 5°) with respect to the IR camera lens, in order to eliminate the Narcissus effect. A fast mechanical shutter (Melles Griot, 04 IMS 001) was used to cut the illumination on and off. The light was switched on at least 15 min prior to the experiments, for stabilization reasons. Five experiments were performed per sample, with a recording time of 200 s.

De-icing time and ice adhesion measurements. A home-built, temperature-controlled, zero humidity chamber was used for the purpose of the de-icing experiments under illumination, consisting of: a bronze cooling pipe, where cold nitrogen at -150 °C was supplied by a Kaltgas cryogenic cooling system; a piezo-actuated stage made by Smaract, consisting of three SLC-1730-S positioners; two 4-wire, class A, RTD temperature sensors (Pt-1000, class B, Sensirion); a humidity module (SHT30, Sensirion); a A201-1 piezoelectric force sensor (FlexiForce QuickStart Board, Tekscan); a force transfer pin; and finally a 3-mm thick glass window that enabled the de-icing experiments due to illumination. The sensor values were recorded through a custom data acquisition box (Beckhoff). A hydrophobic polypropylene cylinder ($R = 1.5$ mm) was filled with fresh deionized water (EMD Millipore Direct-Q 3) and placed on the sample, which was mounted on the stage. The force transfer pin–sample distance was ≈ 1 mm. A vacuum-insulated double shell minimized thermal losses and forced convection inside the chamber was enabled with a fan. Humidity levels were kept at zero throughout the experiments, *via* a cold nitrogen recirculation stream. The force *vs* displacement data were then recorded every 50 ms. The maximum ice adhesion strength measurable with this setup for the given R is ≈ 280 kPa.

Anti-icing and defrosting experiments. The same chamber as in the de-icing experiments was used. A cold nitrogen recirculation stream maintained dry conditions. The exposure time of the camera was necessary to be readjusted, due to severe changes in the intensity of incident light, at the following time moments (defrosting experiments): (a) $t = 0$ s and (b) $t = 600$ s. In the case, again, of the defrosting experiments (control: 3 experiments, metasurface: 3 experiments), frost was grown in ambient humidity conditions, by placing each sample on a cold block, at a temperature of -50 °C, for 45 min. Transfer of the frosted sample to the pre-cooled chamber was done in a fast manner to prevent melting of the formed layer.

Anti-frosting experiments in ambient humidity conditions. An in-house setup was prepared for the anti-frosting experiments, consisting of a xenon light source (300 W 6258 Xe lamp in a 87005 enclosure, Newport), two objectives (4x, 10x) to collimate and focus the light on the sample surface, which was vertically mounted on a peltier element (38.6 W, PE-127-14-25-S, Laird), a cooling system (SST-TD02-LITE, Silverstone) and a Thorlabs CCD camera (DCC1545M-GL). A PID peltier control circuit (TEC-1089-SV, TEC Engineering) was used to regulate temperature (measured with a PT-100 type RTD). The power density of light on the metasurface was $P \approx 1$ kW m^{-2}. The light was switched on for 30 min prior to the experiments for stabilization reasons. Recording framerate was 1 fps. The exposed area on the sample was dried with a nitrogen stream prior and after every frosting cycle.

3.6. Acknowledgements

Partial support of the Swiss National Science Foundation under grant number 162565 and the European Research Council under Advanced Grant 669908 (INTICE) is acknowledged. E. M. thanks Reidt S. and Olziersky A. for their assistance in SEM image acquisition, Stutz R. for the sputtering deposition parameters, Drechsler U. for cleanroom introduction, Caimi D. for wafer dicing, Graeber G. for providing the blackbody sample, as well as Vidic J. and Feusi P. for technical support.

4. TRANSPARENT METASURFACES COUNTER-ACTING FOGGING BY HARNESSING SUNLIGHT

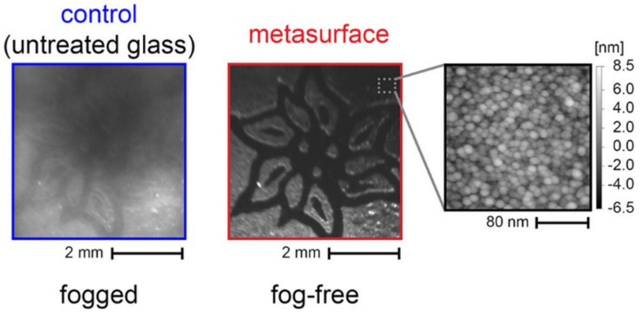

This chapter is reproduced in part with permission from:

Walker, C.*; Mitridis, E.*; Kreiner, T.; Eghlidi, H.; Schutzius, T.M.; Poulikakos D. *Nanoletters*. 2019, 19, 1595–1604. DOI: 10.1021/acs.nanolett.8b04481

***equal contribution**

4.1. Abstract

Surface fogging is a common phenomenon that can have significant and detrimental effects on surface transparency and visibility. It affects the performance in a wide range of applications including windows, windshields, electronic displays, cameras, mirrors, and eyewear. A host of ongoing research is aimed at combating this problem by understanding and developing stable and effective anti-fogging coatings that are capable of handling a wide range of environmental challenges “passively” without consumption of electrical energy. Here we introduce an alternative approach employing sunlight to go beyond state-of-the-art techniques—such as superhydrophilic and superhydrophobic coatings— by rationally engineering solar absorbing metasurfaces that maintain transparency, while upon illumination, induce localized heating to significantly delay the onset of surface fogging or decrease defogging time. For the same environmental conditions, we demonstrate that our metasurfaces are able to reduce defogging time by up to four-fold and under supersaturated conditions inhibit the nucleation of condensate outperforming conventional state-of-the-art approaches in terms of visibility retention. Our research illustrates a durable and environmentally sustainable approach to passive anti-fogging and defogging for transparent surfaces. This work opens up the opportunity for large-scale manufacturing that can be applied to a range of materials, including polymers and other flexible substrates.

4.2. Introduction

The loss of visibility due to surface fogging is a common phenomenon, which presents itself in a variety of daily situations, affecting both transparent and reflective surfaces, such as windows, windshields, electronic displays, cameras, mirrors and eyewear including eyeglasses, safety glasses, ski and scuba goggles, and face masks.[6] This visibility loss is a result of micro-sized water droplets that nucleate and grow on the surface due to either a sudden increase in relative humidity or a sudden drop in surface temperature. These water droplets disperse and reflect the incident light, severely affecting optical clarity.

A number of concepts have been studied and implemented to suppress this undesirable phenomenon. Temporary passive solutions include surfactants or superhydrophilic coatings, both of which increase the relative energy of the surface and shift the equilibrium from a plethora of tiny individual droplets to a very thin and continuous layer.[27,28] In contrast to individual droplets, this thin and continuous water layer does not scatter the incident light, and therefore does not interfere as much with the transparent clarity of the surface. Although improvements have been made to render superhydrophilic coatings more robust,[99] these coatings are more susceptible to contamination due to their increased surface energy[33] and are prone to water inundation, which can reduce visibility. Research aimed at addressing this concern has concentrated on developing zwitter-wettable surfaces, which exhibit either hydrophobic or hydrophilic properties dependent on the water droplet residence time on the surface.[100]

Permanent passive solutions typically take the approach of implementing superhydrophobic self-cleaning surfaces to remove condensed water droplets from the surface. Intricately-engineered superhydrophobicity is here necessary to alleviate nanoscale condensate that nucleates within the textures and destroys the stability of the Cassie–Baxter state and therefore their hydrophobicity property in environments of high relative humidity.[34,35] Both growing condensate droplets as well as new macroscale droplets that come into contact with the surface will be forced into the Wenzel state, producing pinned droplets, destroying the desirable superhydrophobic characteristics,[101] and thus rendering the surface even more adhesive than an otherwise flat surface of same chemical composition.[102] There have also been approaches to mitigate the loss of hydrophobicity resulting from surface condensate, and therefore render such sustainably hydrophobic surfaces effective for anti-fogging. Many of these approaches, inspired by surface features observed on insect eyes and plant leaves, include creating textured surfaces whose size and rationalized geometry allows condensate to grow in the Cassie–Baxter state.[29–32] Because the Cassie–Baxter state preserves the droplet mobility, these droplets can be easily removed by small external forces, such as wind or gravity. An additional and extensively investigated approach is to use the excess energy of coalescing droplets, resulting from the reduction in free surface area, to propel themselves off the surface.[103–107] While both of these approaches enhance the anti-fogging performance, they do not reduce the likelihood of the formation of the undesired condensate in the first place, which, in particular over time, can have a detrimental effect for certain applications.

To address this challenging problem, we propose a different approach. As in recent pathbreaking studies revolving around harnessing light and sunlight for new applications,[108–111] including catalysis, materials synthesis, and desalination,[88,112–114] we utilize a sustainable solution by means of rationally designed transparent natural sunlight absorbing surfaces,[115,116] hereafter termed as metasurfaces, designed to inhibit the heterogeneous nucleation of condensate and also exhibit superior anti-fogging performance, while maintaining optical transparency. We begin by showing qualitatively and quantitatively the shortcomings of three different kinds of wetting behavior on a plain glass substrate, ranging from superhydrophilic to hydrophobic. Additionally, we show that the light-absorbing metasurfaces of the present work enhance evaporation rates of already accumulated condensate. To this end, we analyze, both experimentally and theoretically, the condensation and evaporation behavior of a single droplet on control surfaces and our metasurfaces. This fundamental analysis and discussion provide the motivation to subsequently consider condensation and evaporation of multiple droplets. For our metasurfaces, we observe significant reduction in condensate nucleation rate and an increased evaporation rate. We believe that this research, as a stand-alone technology, as well as in combination with the previously described state-of-art research, will lead to more robust and enhanced passive anti-fogging and defogging surfaces.

4.3. Results and discussion

In order to understand and place into perspective the inherently intertwined phenomena of visibility diminution and surface fogging for transparent and reflective media, we began by investigating the behavior of superhydrophilic (the most common state-of-the-art technique to retain visibility), hydrophobic glass, and untreated glass with intermediate wetting behavior ($\theta^* \approx 90°$), under exposure to a supersaturated water vapor environment. Throughout this study we compare these glass surfaces to our sunlight absorbing metasurfaces, made by sputter deposition. This is a flexible coating technique that has been demonstrated in a roll-to-roll multilayer process for depositing transparent conducting oxides on windows at large-area,[117] while its applications also extend to highly-controllable metallization[118] and deposition of tiny amounts of noble metals with subsequent cost reduction.[119] By using this coating technique, we fabricated a metal-dielectric nanocomposite of gold nanoparticles embedded in titania on glass substrates (for more information on the fabrication and characterization of the metasurface, see Methods and Appendix C, Figure C.1 and Figure C.4). Figure 4.1a–c shows superhydrophilic, untreated, and hydrophobic glass samples, respectively (see Methods for further details on sample preparation and experimental procedure, and Appendix C, section “Advancing and receding water contact angles of the tested surfaces” and Figure C.1, for contact angle measurements on all samples used in our study). The samples were placed on a background consisting of an array of dots, before (t = 0 s) and after exposure for 10 min (t = 600 s) to an environment of supersaturated water vapor (supersaturation (p/p_{L}) equal to 1.3 where p and p_{L} are the partial and saturation pressure of water vapor, respectively). We used the array of dots as a reference to both qualitatively and quantitatively observe the clarity and distortion caused by condensate on the samples upon exposure to supersaturated vapor conditions.

Figure 4.1a compares a superhydrophilic glass surface before being exposed to supersaturated vapor (t = 0 s) and after exposure for 10 min (t = 600 s) (see Methods, section “Setup and experimental protocol” for further details). Comparing this to the same conditions for untreated and hydrophobic samples in Figure 4.1b–c, respectively, we clearly observe that the superhydrophilic glass retains similar clarity as before exposure to supersaturated conditions, while the array of dots under the untreated and hydrophobic substrates suffers from significant blurriness due to the microdroplets scattering incident light. This supports the motivation for using superhydrophilic surfaces where maintaining transparency is important even when exposed to supersaturated vapor environments. Although the superhydrophilic glass sample retains the highest clarity among the three types of glass, it appears to suffer from distortion, apparent by the asymmetry of the array of dots at t = 600 s. In contrast, this asymmetry is not observable when inspecting the untreated and hydrophobic samples in Figure 4.1b–c.

To quantify our visual observations, we determined the parameters C and δ (see also illustration in Figure 4.1d). We quantified C by measuring the mean intensity of each dot, I ($N=25$ dots in total), and normalizing it to the respective mean background intensity, I_b , at $t=0$ and $t=600$ s (subscripts 0 and t denote time zero and t, respectively). We measured the respective intensities by taking the mean grayscale value of the pixels in either the dot or the background. We calculated C per dot at time t by:

$$C=1-\log_{10}[(I_\mathrm{t}/I_{\mathrm{b},t})/(I_0/I_{\mathrm{b},0})] \tag{4.1}$$

We quantified δ by measuring the position of each dot, ($x_{i,0}, y_{i,0}$), at $t=0$ s and ($x_{\mathrm{i},t}, y_{\mathrm{i},t}$), at $t=600$ s, and using this to calculate the distance that each of the dots moves. We normalized this distance with the mean diameter of the dots, d , yields:

$$\delta=\Delta s/d=\frac{1}{d}\sum_{i=1}^{N}\sqrt{(x_{i,t}-x_{i,0})^2+(y_{i,t}-y_{i,0})^2} \tag{4.2}$$

C and δ are reported in Figure 4.1e and Figure 4.1f, respectively, as box plots, where the values of each box and whisker are made up of six experiments ($n=6$) and $N=25$ dots per experiment for a total of 150 measurements. As expected, Figure 4.1e confirms that the clarity of the untreated and hydrophobic glass surfaces is significantly reduced when compared to that of the superhydrophilic glass. We attribute the slightly better performance of the hydrophobic glass compared to the untreated glass to the reduction in nucleation density of the hydrophobic glass and therefore the reduction in the number of drops that scatter the light (see Appendix C, sections "Theoretical effect of surface wettability on fogging resistance", Figure C.2, and "Observed effect of surface wettability on fogging resistance", Figure C.3). Furthermore, Figure 4.1f confirms that the distortion in the case of the superhydrophilic sample is considerable, especially when compared to the untreated and hydrophobic samples. An ideal hydrophilic surface should produce a perfectly continuous water film across the entire sample; however this is not what we observed. We attribute this to the high surface energy of the treated glass, making it more susceptible to contamination[120] that creates pinning points, acts to break up the continuous film, and results in the observable distortion. Even if the surface remained completely clean, additional pinning points from the edges would also create a curved water interface at the edges and also result in distortion. In order to quantify and compare the overall visibility retention of the three surfaces (superhydrophilic, untreated and hydrophobic glass), we introduced a performance factor, $P=(1-\delta)C$, that combines the values of both clarity and distortion. The higher the performance factor the better the visibility retention through the sample. We furthered our comparison to also consider the performance of our metasurface, assuming it remains condensate free (which we demonstate later). Figure 4.1g shows that the untreated glass is the worst performer, followed by the hydrophobic surface and the superhydrophilic surface. Finally, the metasurface achieves maximum performance (100%). It is important to understand that C does not take total light transmittance through the surface into consideration, therefore although our metasurface has a visible light transmittance of 36% compared to the glass transmittance of $\approx 87\%$, this does not affect P . We chose not to incorporate transmittance into P because for many applications, a reduction in visible light transmittance is a desirable property to optimize user visibility comfort and performance. Applications such as car windows, building windows, and sun-protective eyewear utilize transmittance ranging from 15-50%,[121,122] 2-70%,[123] and 15-25%,[124,125] respectively. Advantageously, we designed the metasurfaces studied in this work to harvest both visible and near infrared light in order to obtain the most efficient anti-fogging performance. What is important here is that although the metasurface reduces the sample transmittance, the maximum clarity and lowest distortion are achieved due to the deeply subwavelength gold nanoparticles used to create the metasurface.

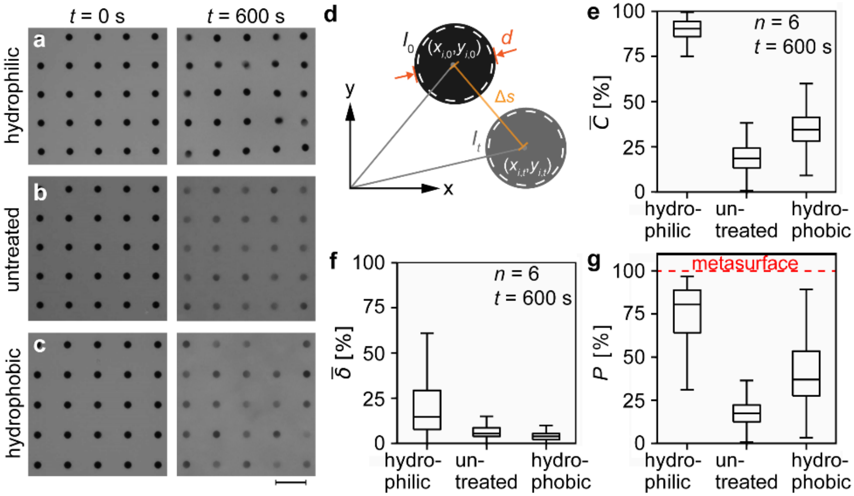

Figure 4.1 Effect of fogging on the clarity and distortion for differing wetting behavior of transparent surfaces. We characterized both the clarity and distortion of transparent glass surfaces by using a dot array placed under the surfaces. **(a–c)** Darkfield micrographs of the surfaces and the dot array were taken before ($t = 0$ s) and 10 min after ($t = 600$ s) the samples were exposed to supersaturated vapor conditions. The before and after for the **(a)** superhydrophilic, **(b)** untreated (neutrally wetting), and **(c)** hydrophobic glass are shown. We quantified the clarity and distortion by analyzing the dot array for each sample type as illustrated in **(d)** using Eqs. (4.1) and (4.2). The quantified effect of fogging on **(e)** clarity, C , and **(f)** distortion, δ , on each of the three surfaces is illustrated as box plots, where each type of surface was tested using six different samples ($n=6$). We also estimated the visibility retention through the three surfaces by introducing a performance factor, P , and compared them to a sunlight absorbing metasurface ($P=1$), as shown in boxplot **(g)**. Scale bar **(a–c)**: 100 µm.

In order to demonstrate the design of our metasurfaces, we proceeded with characterizing their topography in the microscale and nanoscale. Figure 4.2a shows a schematic illustration of the different layers constituting the metasurfaces. In principle, they consist of repeated ultrathin bilayers of Au nanoparticles and a TiO_2 nanolayer. There is also an additional protective TiO_2 top-layer. Our metasurfaces have $k+1=4$ bilayers in total and a total thickness of ≈ 60 nm. The cross-sectional composition of the metasurfaces is demonstrated in the scanning electron micrograph, which reveals that the layers of Au nanoparticles are embedded in and spaced apart by the TiO_2 layers.

For improving image quality and emphasizing on the flexibility of the multilayer design, here we show the micrograph of a metasurface consisting of 22 bilayers.

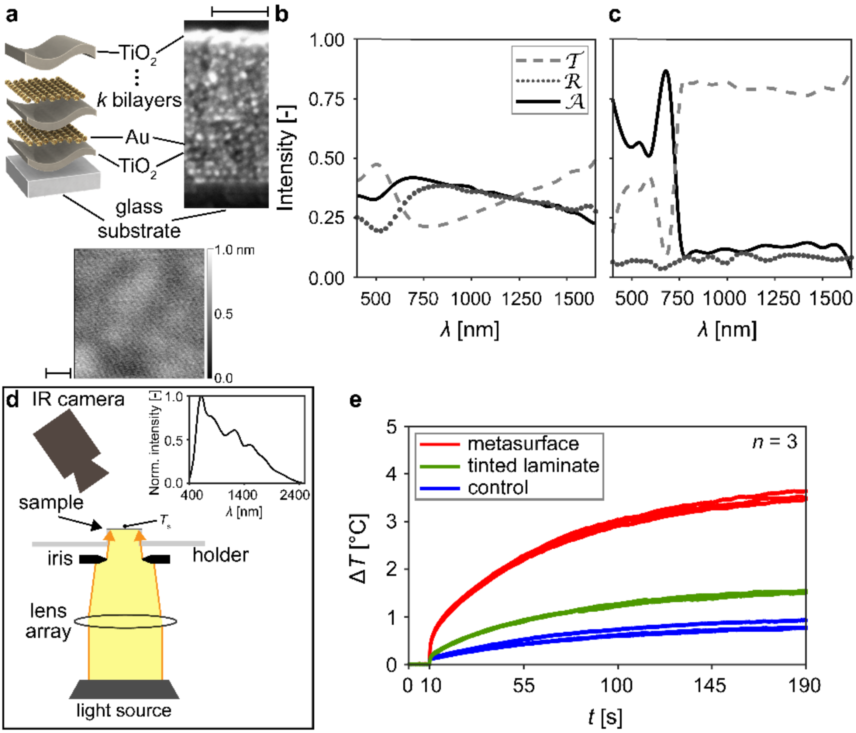

Figure 4.2 Topographical, optical and light-induced heating characterization of the metasurface and comparison to commercially available tinted laminate with similar transmittance in the visible spectrum. (a) Top left: Schematic representation of the multilayer structure of Au nanoparticles and TiO_2, which make up the metasurface; top-right: scanning electron micrograph of the metasurface cross-section, acquired with secondary electrons, where the bright circular spots are the Au nanoparticles; bottom row: atomic force micrograph of the metasurface. **(b–c)** Reflectance $(\mathcal{R})$, transmittance $(\mathcal{T})$, and absorbance $(\mathcal{A})$ spectra of the **(b)** metasurface and **(c)** commercially available tinted laminate for visible and near infrared wavelengths (400–1650 nm). **(d)** Experimental setup showing how the temperature increase of the samples upon illumination was measured. **(e)** Sample temperature increase, ΔT, over time, t, for the metasurface, tinted laminate, and control glass samples. Sample thickness was ≈ 4 mm. Scale bars **(a)**: 50 nm.

In Figure 4.2a, bottom-row, the atomic force micrograph of our metasurface indicates that the surface is in fact very smooth, with RMS roughness <1 nm. We then compared the performance of our metasurface to a glass substrate with a commercially available tinted laminate having similar level of transmittance in the visible spectrum. Figure 4.2b–c shows the reflectance $(\mathcal{R})$, transmittance $(\mathcal{T})$, and calculated absorbance $(\mathcal{A} = 1 - \mathcal{T} - \mathcal{R})$ of both samples in the 400–1650 nm wavelength range. The visible light transmittance (400–750 nm) for the metasurface and tinted laminate was 36% and 33%, respectively. Figure 4.2b shows that the metasurface has a relatively constant broadband absorption in the measured wavelengths. On the other hand, Figure 4.2c shows that the commercially available tinted laminate has high absorption in the visible wavelengths (400–750 nm); however, in the near infrared range (750–1650 nm) its absorption drastically decreases. The broadband absorption of the metasurface is advantageous because it allows for increased absorbance of sunlight in the near infrared and therefore a higher temperature response to inhibit fogging or encourage evaporation (see Figure C.5 for the spectra of the control sample). Figure 4.2d shows a schematic of the experimental setup and the light source spectrum that we used to illuminate the samples and measure their temperature. Figure 4.2e shows a plot of sample temperature above ambient, $\Delta T = \overline{T}_{\mathrm{s}}(\mathrm{t}) - \overline{T}_{\mathrm{s,0}}$, *vs* time, t, upon illumination, for the metasurface and the tinted commercially available laminate, where $\overline{T}_{\mathrm{s}}(\mathrm{t})$ and $\overline{T}_{\mathrm{s,0}}$ are the average sample temperatures at time t and $t = 0$ respectively. The steady-state value of ΔT for the metasurface was 130% higher than that of the commercially available tinted laminate (see also Appendix C, section “Infrared thermography and temperature response measurements” for more information on the temperature response of the samples due to light-induced heating).

In order for the metasurfaces to achieve best performance in a supersaturated vapor environment, they must inhibit the formation of condensation on the surface. To this end, we studied the efficacy of our metasurfaces to use naturally occurring sunlight to generate plasmonic surface heating in order to aid in defogging and anti-fogging of surfaces exposed to supersaturated vapor environments, to maintain C and limit δ. Here we compared our metasurface to glass (hereafter referred to as control) for defogging and anti-fogging applications. Figure 4.3a illustrates the setup that we employed. It consisted of a sun-mimicking light source and lens to focus the light onto the sample plane (the metasurface was facing upwards) with a spot diameter of 7 mm that fully illuminated our 5 x 5 mm samples at a power density of 4 suns. We mounted two cameras to extract data in order to quantify the experiments; a CMOS angled side view camera to observe the droplet’s contact angle and a top view infrared (IR) camera to construct the temperature profile of the sample and droplet. It is well-known that the contact angle progression of an evaporating droplet can have a significant effect on the evaporation time,[126–128] therefore in order to isolate the effect of the illuminated metasurface we treated both surfaces with a vapor-deposited trichlorovinylsilane (TCVS). This resulted in a consistent receding contact angle of approximately 50°, allowing consistent measurements between surfaces, beginning when the droplets reached the receding angle and then continued evaporation in the constant contact angle mode. Figure 4.3b quantifies the contact angle progression of the evaporating droplets as a function of time for both the control (red curves) and metasurface (blue curves) samples. We observed that the receding angle for both samples is the same and the constant contact angle mode becomes the mode of evaporation for the duration of the experiments. By establishing the same contact angle progression during evaporation for both surfaces, we show in Figure 4.3c that the metasurface increases the droplet evaporation rate by approximately four-fold for a droplet that is of the same order of magnitude compared to the sample size. This is caused by the considerable light absorption and heating of our metasurface, which is observable by examining Figure 4.3d and Figure 4.3e (see Appendix C, section “Infrared thermography and temperature response measurements” and Figure C.4 for more information on the temperature response of the samples due to light-induced heating). Here we show synchronized side-view (visible) and top-view (IR) image sequences of illuminated droplets on a control and metasurface sample, respectively, before and for the duration of evaporation. The leftmost IR images ($t < 0$ s) show the surfaces at steady state under illumination before a droplet is placed on the surface. While the control sample in Figure 4.3d remains very close to room temperature, the metasurface takes advantage of light induced localized surface plasmon oscillations on the nanometer-scale gold particles, resulting in heating of the surface by > 10 °C. When placing a droplet on the surface, we observed a reduction in the temperature of the surface, shown in the IR images ($t = 0$ s) of Figure 4.3d and 2e. This can be explained by the effect of evaporative cooling, which causes the droplet, and subsequently the surface it is in contact with, to cool due to energy required by water molecules to overcome the latent heat of evaporation and change from liquid into vapor. Advantageous to the evaporation, the metasurface is able to transfer more heat into the droplet, while the droplet maintains a temperature lower than the surface temperature. Near the end of evaporation, the metasurface returns to its steady state temperature as in the case without the droplet, and so does the control, observable at $t = 200$ s and 800 s in the IR images of Figure 4.3d and Figure 4.3e, respectively.

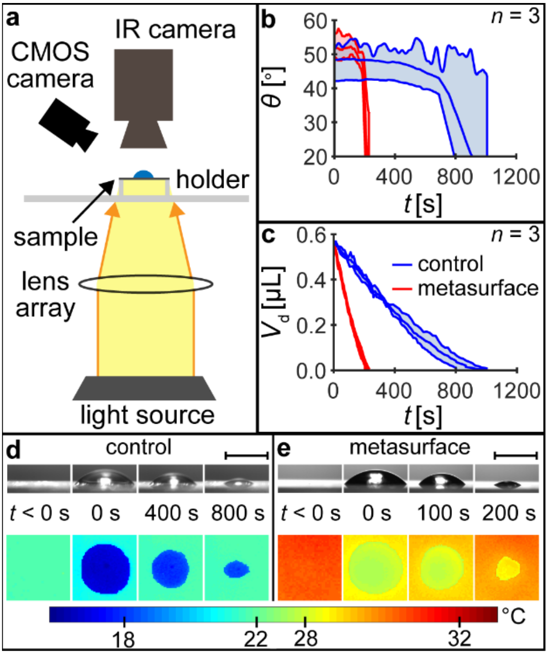

Figure 4.3 Sunlight absorbing metasurfaces drastically reduce evaporation time of a single droplet. (a) Experimental setup consisting of a sun-mimicking light source and a lens system to focus the light on the sample with a power density of 4000 W m^{-2}. We used an angled side-view CMOS camera to observe the contact angle progression of the droplets and a top-view IR camera to record the sample and droplet temperature profiles. **(b)** Plot of contact angle, θ, *vs* time, t, for control samples (red curves) and metasurfaces (blue curves). The evaporation rate of the metasurfaces was approximately four times higher than the control, as seen in plot **(c)**, droplet volume, V_d, *vs* t. **(d–e)** Side view and infrared top view of a single droplet evaporating on a **(d)** control surface and **(e)** metasurface. Scale bars **(d–e)**: 1 mm.

Using the ability of our metasurfaces to effectively harness sunlight energy over a broad spectrum and turn it into heat, we showed that we could reduce the drying time of single droplets. We proceeded to focus on the drying of fogged surfaces, as such an investigation is more relevant for surface defogging and anti-fogging. One would expect the enhanced evaporation rate in the case of the metasurface to also be present for multiple droplets, albeit to an extent that remains to be shown. We investigated this by conducting defogging experiments on four different samples. As before, the control surface was plain untreated glass (untreated control), which we initially compared to plain glass coated with poly(perfluorodecyl acrylate) (pPFDA; hydrophobic control) to render it hydrophobic (see Methods, section “Surface preparation” for further details). The third and fourth samples consisted of an untreated metasurface and a metasurface treated with pPFDA (hydrophobic metasurface) to render it hydrophobic (see Appendix C, section “Advancing and receding water contact angles of the tested surfaces” and Figure C.1 for details on wetting behavior). We initially exposed each surface to supersaturated conditions by cooling the surface. This caused a layer of condensate to form. The samples were then transferred to the experimental setup depicted in Figure 4.3a. To better mimic real-world conditions, we changed the power density to 1 sun (1000 W m^{-2}). We then measured the evaporation time for seven different samples of each sample type (see Methods, section “Setup and experimental protocol” for further details). We found that both untreated and hydrophobic metasurfaces outperformed the untreated and hydrophobic control samples by reducing the time necessary for complete surface defogging.

Figure 4.4a–b show image sequences of the untreated control and the untreated metasurface, respectively. Qualitatively, one observes that the condensate surface coverage remains similar for the first 70 s, followed by a faster reduction of condensate surface coverage on the untreated metasurface, and hence a reduced defogging time. Figure 4.4c shows a box plot of the defogging time (t_{df}) for seven individual runs on the two sample types depicted in Figure 4.4a–b. Figure 4.4c additionally shows t_{df} for the hydrophobic control and metasurface. As expected, the quantitative analysis indicates that there is a clear improvement in t_{df} for the metasurfaces when compared to the plain glass, illustrated by a two sample t-test p value < 0.001, indicating that the difference between the two population means is statistically significant. Here we note that the untreated metasurfaces have a slightly lower receding contact angle, by approximately 10°, than the untreated control surfaces (see Appendix C, section “Observed effect of surface wettability on fogging resistance for further details” and Figure C.1). However, the significant reduction of t_{df} should not be attributed to this small difference in wettability and can only be due to the metasurface heating and corresponding evaporation enhancement by increasing the saturation vapor pressure above the droplets.

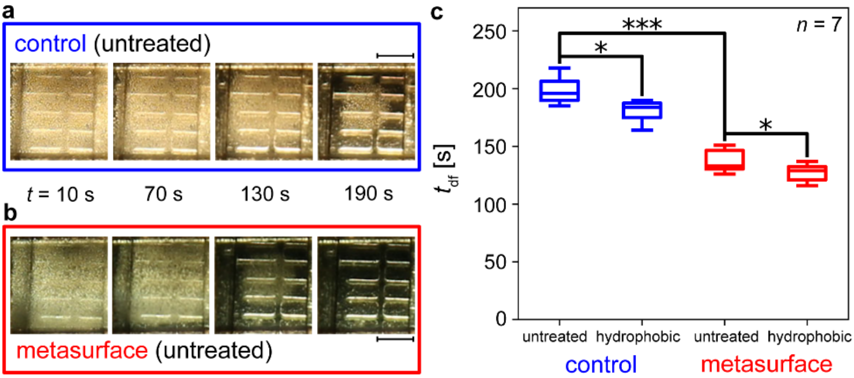

Figure 4.4 Using metasurfaces to enhance visibility restoration by reduced defogging time. Using metasurfaces that efficiently turn the absorbed light into heat, we were able to reduce the defogging time compared to a control surface. The transparency *vs* t is shown for an **(a)** untreated glass surface (untreated control) and an **(b)** untreated glass metasurface (untreated metasurface). Statistically, the metasurfaces reduced the defogging time (t_{df}) by approximately 25% as shown in **(c)**. We tested both the control and metasurface samples against their hydrophobic counterparts to see if hydrophobicity also has an effect on t_{df} . For both pairs of samples we obtained two sample t-test p values < 0.05 to prove this was the case. Significance bars in **(c)** are represented by * for $p < 0.05$ and *** for $p < 0.001$. Scale bars (**a–b**): 2 mm.

Additionally, our results in Figure 4.4c show that the hydrophobic surfaces have better performance in comparison to their respective untreated samples, both of which have a two sample t-test p value < 0.05. On the one hand this seems surprising because it is well known that droplets on a surface with a larger receding angle have a slower evaporation rate than neutrally wetting or hydrophilic droplets,[126–129] at least in the µL volume range. On such scales it is probable that, independent of the macroscopic receding angle, the droplets evaporate in a constant contact radius (see Figure 4.3b, the tail end of contact angle progression; see also Ref.[127]). On the other hand, we observed that the volume of liquid on the surface in the form of condensate droplets is approximately 10% less for hydrophobic glass than for the control glass (see Appendix C, section “Observed effect of surface wettability on fogging resistance”). This means that there is simply less water on the surface to vaporize and offers the most rational explanation as to why we observed a decrease in t_{df} for the hydrophobic samples.

As mentioned, the ability to inhibit fogging is an important quality of our metasurfaces and could be used to an advantage in many applications, particularly for specialized outdoor eyewear, which can suffer from visibility loss from fogging even during sunny weather. We tested the efficacy of our metasurfaces by comparing them to control samples, both untreated and superhydrophobic, exposing each sample to the same supersaturated conditions. We created a supersaturated environment by modifying our experimental setup, illustrated in Figure 4.5a, to include a chamber housing the sample and including a water bath and a small fan. Additionally, the camera was tilted at a shallow angle with respect to the sample plane in order to avoid direct light expose to the sensor (see Methods, section "Setup and experimental protocol" for further details). The fogged surfaces appear brighter due to light scattering by the droplets, to which the slightly tilted camera with respect to the incident light is sensitive. Figure 4.5b–d show image sequences of the fogging behavior of the untreated control, superhydrophilic state-of-the-art, and untreated metasurface samples, respectively, under supersaturated conditions. The first, and perhaps most important observation is that the metasurface remains, for the most part, condensate free. Although one observes slight condensate bursts on parts of the surface, it quickly evaporates again and at steady state the metasurface remains condensate free. In contrast to the metasurface, the untreated control and superhydrophilic state-of-the-art surfaces in Figure 4.5b–c show immediate condensate formation. On the one hand, the condensate on the untreated control takes the form of many droplets that scatter the light and almost completely eradicate the visibility of the background. On the other hand, the condensate on the superhydrophilic state-of-the-art surface results in a film of water that distorts the background. Both of these surfaces significantly reduce the visibility retention of the background in comparison to the metasurface. Remarkably, the metasurface remains condensate free. Even though the metasurface is able to more efficiently turn the broadband illumination into heat and significantly raises the temperature of the surface in comparison to the control samples, the approximately 3 °C temperature increase due to the heat response of the metasurface combined with the convective heating inside the chamber produces a p/p_{L} of approximately unity (1.01 ± 0.01) for the aforementioned experimental conditions. The control sample also profits from the convective heating inside the chamber, however the heat response from the light irradiance is considerably less resulting in a p/p_{L} of 1.22 ± 0.01 and the necessary conditions for fogging to occur.

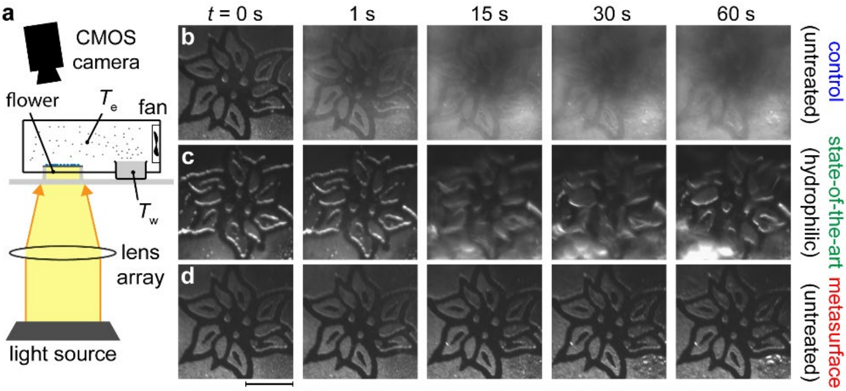

Figure 4.5 Anti-fogging performance enhancement by efficient sunlight absorbing metasurfaces. We tested the anti-fogging performance of our metasurfaces and compared it to the performance of untreated control and superhydrophilic state-of-the-art samples, using the setup illustrated in **(a)**. We enhanced the setup with the inclusion of a simple environmental chamber in which we placed a bath of warm water at a temperature T_w while also measuring the environmental temperature (T_e) and the sample temperature (T_s), in order to achieve a supersaturated environment. We used a fan to ensure that the water vapor inside the chamber was well mixed. The results for 60 s of supersaturation are shown in the image sequences for the **(b)** untreated control, **(c)** superhydrophilic state-of-the-art, and **(d)** untreated metasurface samples. In order to better demonstrate the distortion effect of the superhydrophilic sample, we slightly increased the distance between the surface and the flower illustration. Scale bar **(b–d)**: 2 mm.

4.4. Conclusions

Surface fogging is a common hindrance, especially when considering the clarity and distortion of light travelling through transparent or back from reflective surfaces. Due to the importance of the phenomenon there are a variety of existing approaches to mitigate this loss in optical efficiency, however we demonstrated that the most widely used solution, superhydrophilic surfaces, does not retain all optical efficiency aspects, resulting in significant image distortion, while untreated and hydrophobic surfaces result in significant loss of clarity. Both of these methods change the inherent surface energy of the substrate, which continues to prove to be a difficult characteristic to maintain for long periods. We demonstrated a novel approach by employing plasmonic metasurfaces harnessing the broadband spectrum of the sun, to efficiently heat up a surface, thereby significantly improving defogging and anti-fogging properties, without a marked loss of transparency. For applications that require reduction of light transmission, the broadband absorption of our metasurfaces offers a favorable property compared to commercially available products used for reducing light transmission, such as tinted laminates. This approach would result in considerable performance gains for applications such as windows, windshields, electronic displays, cameras, mirrors, and eyewear. The variety of substrates, including polymers and flexible surfaces, which can be coated with our metasurfaces as well as the potential manufacturing scalability of the metasurface coating process make this technology a viable solution for anti-fogging and defogging in commercial applications.

4.5. Methods

Surface preparation. We used double side polished, 4-in, 500-µm thick wafers (UniversityWafer, Inc.) made of fused silica. We cut the wafers into 5 mm x 5 mm square specimen, using a wafer dicer (ADT ProVectus LA 7100) with a diamond head. Prior to cutting, a 3.3 µm polymer top-layer was applied to protect the glass surface. After the dicing process, the protective layer was removed by sonication in acetone for 2 min, followed by an equal-time sonication in isopropyl alcohol, and water. We also treated each specimen with oxygen plasma (Oxford Instruments, Plasmalab 80 Plus) for 7 min. Shortly after, we prepared 7 different sample types:

a. *Untreated control*. We stored freshly-diced and cleaned glass wafer pieces in a dust-free environment, under ambient temperature (≈23 °C) and relative humidity (RH = 40 – 60 %), for several days (>5 d), enough time for the adsorbed hydrocarbon layer to approach equilibrium with the surfaces (therefore providing stable advancing and receding contact angles).

b. *Hydrophilic control*. We immediately (<1 hr) used the plasma-treated glass specimen in the clarity and distortion evaluation, as well as in the defogging experiments.

c. *Untreated metasurface*. We used sputter deposition (Von Ardenne CS 320 C) to fabricate the light-absorbing metasurface on top of the fused silica substrates, in line with previous research.[130] Two component materials were used, gold nanoparticles (Au) and titanium dioxide (TiO_2), with the following deposition parameters: 50 W DC field, 6 µbar pressure, 3 s duration, and 600 W RF field, 6 µbar pressure, 43 s duration, respectively. We fabricated a structure of 8 alternating Au and TiO_2 layers in total, with the first layer being TiO_2. The metasurface was finalized with an extra TiO_2 top-layer (deposition time of 72 s). The thickness of the metasurface has been estimated ≈60 nm, with a mean absorption of 37% and transmission of 36% (see also Figure 4.2) in the wavelength range of 400 – 750 nm.

d. *Silane-treated control*. For the single droplet evaporation experiments, we used a homebuilt vacuum chamber for physical vapor deposition of trichlorovinylsilane (TCVS; 97%, Sigma-Aldrich) on our glass substrates. For this purpose, we first transferred 1 mL of TCVS into a glass container, under nitrogen atmosphere. With the container connected to the chamber and its valve closed, we then evacuated the chamber until a stable pressure of 100 µbar was reached, at which moment the valve was opened, while the chamber was also isolated from the vacuum pump. Deposition time was 20 min, at a temperature of ≈23 °C. In the end, we removed the excess of TCVS with a prolonged evacuation and purging cycle.

e. *Silane-treated metasurface*. We followed the same process as in (d) to deposit TCVS on our glass specimen already coated with metasurfaces.

f. *Hydrophobic control*. We utilized initiated chemical vapor deposition method (iCVD; iLab^{TM} Coating System, GVD Corporation) to deposit ultrathin conformal films of poly(perfluorodecyl acrylate) (pPFDA) on clean glass substrates, in order to render them hydrophobic (see Appendix B for detailed information on the optimization process followed to determine the optimum deposition parameters). The advantage of pPFDA over other fluoropolymers lies on its low surface energy (9.3 mN/m), which is half of the surface energy of the widely-used poly(tetrafluoroethylene) (18 mN/m).[131] Silane-treatment of the substrates according to (d) precedes iCVD. The covalently bound surface vinyl groups in TCVS react with the vinyl groups in perfluorodecyl acrylate monomers and bind them chemically to the substrate.[132] For the iCVD deposition we used 1H,1H,2H,2H-perfluorodecyl acrylate (PFDA; 97%, with *tert*-butylcatechol as inhibitor, Sigma-Aldrich) and *tert*-butyl peroxide (TBPO; 98%, Sigma-Aldrich) as monomer and initiator, respectively.[58] The main deposition parameters are reported here: TBPO flow rate was 2.6 sccm, PFDA flow rate was 1.0 sccm, substrate temperature was ≈20 °C, filament temperature was ≈300 °C, PFDA container temperature was 80 °C, process pressure was ≈100 mbar, and deposition time was 15 min. We stabilized all temperatures for 5 min prior to each deposition; we also purged the vacuum chamber with nitrogen for 10 min after deposition.

g. *Hydrophobic metasurface*. We followed the same procedure as in (f) to deposit pPFDA on our glass, metasurface-coated specimen.

Surface characterization. The cross section of the metasurface was imaged by a Hitachi SU8230 scanning electron microscope, while the top-view image was acquired with a Brooker Dimension Fastscan atomic force microscope. We measured the reflection and transmission spectrum of the metasurface, tinted laminate (LLumar Esprit Series ATC 35 CH SR HPR), and control samples for the 400–1650 nm wavelength range using a home-built spectroscopic system.[133] We measured the advancing and receding contact angles of each sample type using a DataPhysics OCA 35 goniometer and their SCA software, by the inflation/deflation method (droplet volume of 2–3 µL). The observations of the condensing droplets under the microscope used for the Appendix C were performed using an upright microscope (Olympus BX60), with a 5x objective (Olympus MPlan 5x/0.10 BD JAPAN) and a 20x objective (LMPLanFI 20x/0.40 BD JAPAN) in bright-field configuration.

Setup and experimental protocol. We carried out the clarity and distortion measurement experiments using an upright microscope (Olympus BX60) and a 5x objective (Olympus MPlan 5x/0.10 BD JAPAN) in dark-field configuration. We placed the matrix of dots, which served to quantify the clarity and distortion, on top of a Peltier element. We then placed the sample in question on top of the dotted matrix and blew a steady stream of nitrogen onto the sample while cooling it down to 6 °C with the peltier element in order to create a locally dry environment, to prevent premature condensate formation on the sample. After the temperature had stabilized, we stopped the nitrogen stream, exposing the sample to 40% relative humidity at 24 °C ($p/p_\mathrm{L} = 1.28$), at time $t = 0$ s. We then recorded the fogging process on the sample exposed to the abovementioned supersaturated conditions for a duration of 10 min ($t = 600$ s).

We conducted the single droplet evaporation experiments using the setup depicted in Figure 4.3a. Using two lenses, we collimated and focused a broadband (sun-mimicking) halogen light source (Schölly Fiberoptic GmbH, Flexilux 600 longlife 1.25 A) onto each test sample at a power density of 4000 W m-2 (corresponding to 4 suns). In order to get the most representative results for the aforementioned applications, it was important that the surface of each sample was fully irradiated by the focused light source and that as little contact with the holder as possible was made in order to limit heat diffusion from the metasurface to the surrounding media. Our focused light had a diameter of ≈ 7 mm and we used 5 mm x 5 mm samples. We irradiated the sample with light until its temperature reached steady state (see Appendix C, section “Infrared thermography and temperature response measurements”). We recorded the temperature of the sample using an infrared (IR) camera (FLIR SC7500, spectral range of 1.5–5.1 µm) before the droplet was placed on the sample ($t < 0$ s) as well as after placing the droplet and throughout its complete evaporation period. After placing an approximately 1 µL droplet on the sample, we additionally began recording a side view using the CMOS camera. In order to allow each droplet to reach a constant receding contact angle and therefore give comparable data between sample types, $t = 0$ s corresponds to the moment when each droplet reached a volume of 0.6 µL. Starting at $t = 0$ s, we computed the contact angle and volume of the droplet until it had completely evaporated. For both sample types (untreated control and untreated metasurface), we carried out three experiments on different samples. For the IR images in Figure 4.3d–e we note that images of the surface and the droplet were separately calibrated (due to differing emitted signal for the same temperature) and overlaid in order to enable usage of a single temperature scale bar. We carried out all the experiments in an environment with RH = 64%, at 21.8 °C. We also acquired the transient thermal response of an untreated control, an untreated metasurface, and a commercial absorber (Thorlabs, NE504B; unmounted absorptive neutral density filter; optical density of 0.4) using the infrared camera, with a 50 mm F/2 lens, at a framerate of 10 fps, and for two different power densities (1 sun and 4 suns). We kept the optical axis of the camera at a 5° angle with respect to the out of plane vector of each surface under test in order to alleviate the Narcissus effect.

For the multidroplet defogging experiments shown in Figure 4.4 we used the same setup as depicted in Figure 4.3a, mounting a Canon 5D Mark III DSLR camera at an angle of approximately 45°. We placed a fishbone pattern on the holder below the sample in order to improve contrast and illustrate the sample transparency. We fogged each sample by cooling it down to 0 °C for 5 min in an environment with a relative humidity of 60% at 23.0 °C ($p/p_{\mathrm{L}} = 2.75$). We proceeded to take the sample off the peltier element and transferred it to the holder, which was then irradiated with light at a power density of 1000 W m^{-2} (approximately 1 sun) in an environment with a relative humidity of 60% at 23.0 °C. We measured the time and visually recorded the samples using the camera until the condensate had completely evaporated. We conducted 7 experiments on different samples for each sample type (control untreated, control hydrophobic, metasurface untreated, metasurface hydrophobic). We tested each sample population for a standard normal distribution using the Kolmogorov-Smirnov test and validated the improvement in defogging time using the two-sample t-test.

We carried out the anti-fogging experiments using the setup depicted in Figure 4.5a. We placed a small printed illustration (edelweiss flower) below the sample holder, to give an enhanced impression of visibility retention. The illustration was sprayed with a passive anti-fogging agent (Aqualung Anti Fog Spray) to reduce condensation on the flower (not completely effective as condensate is slightly visible for $t = 30 - 60$ s in Figure 4.5d, behind the otherwise fog-free metasurface). The experiments were conducted by setting the temperature of the water bath (T_{w}) and measuring the environmental air temperature inside the chamber (T_{e}). We also measured the sample temperature (T_{s}) to determine p/p_{L} . We used the fan in order to get a homogeneous distribution of p/p_{L} throughout the chamber. When T_{w} reached 65 °C, we turned the fan on and the experiments began, corresponding to $t = 0$ s. We recorded the process for 60 seconds. In order to determine the supersaturation of the vapor in the chamber with respect to the sample we ran three individual experiments both for the metasurface and control samples. For the metasurface we obtained an average environmental temperature across the three experiments of 35.9 ± 0.3 °C and an average surface temperature of 35.8 ± 0.4 °C. These three experiments resulted in an average supersaturation above the metasurface of 1.01 ± 0.01. For the glass surface we obtained an average environmental temperature across the three experiments of 37.3 °C ± 0.5 °C (the increase in environmental temperature was due to the slow warming of the chamber after repeated experiments) and an average surface temperature of 33.7 °C ± 0.6 °C. These three experiments resulted in an average supersaturation above the glass surface of 1.22 ± 0.01.

4.6. Acknowledgments

We thank J. Vidic and P. Feusi for assistance in experimental setup considerations and construction; U. Drechsler and D. Caimi for assistance in surface fabrication; and Dr. F. Dähler and Prof. A. Steinfeld for access and assistance with spectroscopy measurements. We acknowledge support by the European Research Council under Advanced Grant 669908 (INTICE).

5. TRANSPARENT METASURFACES NATURALLY BOOSTING THEIR OWN SUPERHYDROPHOBICITY BY ABSORBING SUNLIGHT

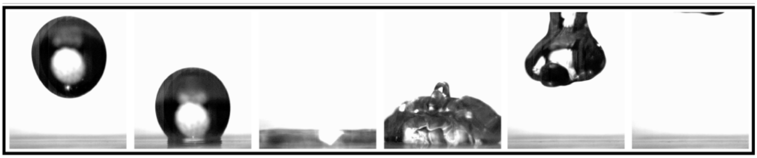

This chapter contains preliminary results with the intent of subsequent publication:

Mitridis, E.; Lambley, H.; Tröber, S.; Schutzius, T.M.; Poulikakos D.
Transparent metasurfaces naturally boosting their own superhydrophobicity by absorbing sunlight.

(*under preparation*)

5.1. Abstract

Imparting and maintaining superhydrophobicity has received increasing attention as a research topic in the last few decades, driven by a broad range of applications and enabled by advancements in rational surface micro and nanoengineering. Repelling hot water has proven challenging due to ensuing condensation into the surface texture that compromises its anti-wetting behavior. Researchers have tried to mitigate nucleation condensation by creating surfaces with multiple tiers of roughness and tuning their geometrical features to hinder the propagation of condensate. However, the solutions proposed are limited by working temperatures and often obstruct visibility through transparent surfaces. Here we introduce a novel and scalable method employing plasmonics to harvest sunlight and naturally heat the surface, able to sustain water repellency also under challenging environmental conditions of high temperature and humidity, which strongly promote condensation. We demonstrate that with our superhydrophobic metasurfaces, illuminated by a sunlight equivalent source, we can completely prevent impalement of dynamic hot water droplets with temperatures higher than 70 °C by suppressing condensate formation within the texture. All this is done while maintaining optical transparency. Our work can find numerous applications as a sustainable solution against impacting water on surfaces such as eyewear, optical components and windows.

5.2. Introduction

Inspired by natural manifestations (lotus leaf,[134] butterfly wings,[135] water strider legs[136]), superhydrophobic surfaces have received significant attention in recent years for their unique self-cleaning,[137] anti-fouling,[138] and anti-icing[139] properties. This extreme water repellency, especially for dynamic impacting droplets, can be achieved by introducing open and closed microstructures[40–42], hierarchical surface roughness,[43–47] low-surface-energy materials,[36–39] and substrate flexibility.[37,48,49] Such surface and substrate properties act to stabilize an intervening, lubricating air layer that is responsible for high droplet mobility (so-called Cassie-Baxter wetting state[140]) and prevent a transition to the sticky Wenzel wetting state (i.e., impalement).[141] For real-world applications, the ability to repel impacting droplets is critical and numerous studies have investigated it under a range of environmental conditions and droplet temperatures ranging from supercooled droplets[49] and surfaces[40,142] to ambient[143,144] to hot droplets.[50] Typically, impalement is prevented by ensuring that the antiwetting, capillary pressure, P_c, is greater than the wetting, droplet pressure, P_w.[145] However, departing from ambient conditions yields a plethora of additional mechanisms for the loss of superhydrophobicity including condensation within the microtexture when exposed to hot vapor[34,50,51] and increased viscosity and freezing in the case of supercooled droplets.[40,49,146–148] Condensation resistant superhydrophobic surfaces have been demonstrated using nanotexturing through droplet coalescence[106,149] and scaling texture to prevent filling within the droplet contact time[52,53] and minimizing the adhesion force of filled cells.[50] Yet, all of these approaches fail to prevent the initial nucleation of condensation embryos, limiting their working envelope.

Another important aspect of superhydrophobicity, for droplets that are already impaled, is the highly desirable ability of a surface to facilitate reversing of the Wenzel-to-Cassie-Baxter wetting transition.[54,55] This can be achieved by means of substrate heating (embedded Joule heating or heating stage),[55,150] droplet coalescence,[54] substrate vibration (in combination with two-tier roughness and impalement only at the microscale),[43,151,152] gas generation via electrolysis,[153,154] electrowetting,[155,156] depressurization,[157,158] water density fluctuations (nonclassical pathway, lower resistance to dewetting),[159] transient intervening layers,[160] and backpressure.[161] Many of these techniques rely on active methods or other droplets and fluids to dislodge a pinned droplet and it is a major challenge to achieve such a transition passively, in a natural manner. Moreover, providing multifunctionality by maintaining optical transparency,[162,163] an important property in many practical applications, is counteractive to imparting superhydrophobicity, since surface roughness obscures light by causing scattering.[164]

To address these challenging problems of condensation enhanced impalement and the limitations of surface texturing, energy, and flexibility on resisting impalement, we propose a novel additive approach exploiting different aspects of the involved physics. As with other innovative studies based on using sunlight for new applications,[108–111,113] including catalysis,[112] desalination,[88] materials synthesis,[114] and ice/fog repellency,[130,165] here we present rationally designed transparent solar absorbing superhydrophobic metasurfaces as a solution.[130,165] These surfaces are designed to repel water droplets and condensate across a range of temperatures all while maintaining optical transparency, critical to many functional water repellent surfaces exposed to natural light.

5.3. Results and discussion

To study the phenomenon of condensation-based impalement of hot droplets on superhydrophobic surfaces, in line with current research on impalement resistance under ambient (isothermal) conditions, we begin by fabricating transparent low surface energy polyurethane acrylate (PUA) micropillared samples using soft-lithography. We then compare these to our light absorbing plasmonic metasurface-coated samples designed to enhance repellency of hot water through sunlight-driven heating while maintaining transparency.[130,165] The plasmonic coating was applied by means of sputter deposition and the surfaces were rendered superhydrophobic by means of an ultra-thin conformal low surface energy polymer coating made with initiated chemical vapor deposition (iCVD). Both the plasmonic and the iCVD coatings do not change the underlying geometrical features of our micropillared surfaces. (See Methods, Appendix D, section "Topography of the control", and Figure D.1 for fabrication steps and topography for all types of samples used in this study.)

Figure 5.1a shows a scanning electron micrograph of an iCVD-coated PUA micropillared metasurface sample, hereafter termed superhydrophobic metasurface. We observe that both the plasmonic and iCVD coatings cover the entire surface homogeneously, making them practically indistinguishable from the bare pillars. (For the control surface, which is a superhydrophobic micropillared sample, see Appendix D, section "Topography of the control", and Figure D.1.) Some sub-micron features visible are the outcome of the soft lithography replication process; however, no significant local nanoroughness is observed (≤ 15 nm RMS), on our single-tier rough surfaces. We measured an advancing contact angle, θ_{a}, of 160.2° ± 2.5°, and a receding contact angle, θ_{r}, of 140.5° ± 3.1°. As a reference, in the case of smooth metasurface- and iCVD-coated surfaces we measured θ_{a} =125.4° ± 1.0° and θ_{r} =118.7° ± 0.7°. Figure 5.1b shows a schematic of the different layers constituting our superhydrophobic metasurfaces: glass substrate, PUA pillars, metasurface coating and iCVD coating. The metasurface coating is a nanocomposite of gold (Au) and titania (TiO_2), sputtered in an alternating manner. The thickness of the coating was estimated at ~60 nm. Our structured surfaces have the following geometrical dimensions: $[d, p, h] = [2.5, 5.0, 3.3]$ µm, where d is pillar diameter, p is pitch and h is pillar height. The cross-sectional view of an identically fabricated metasurface with exaggerated thickness for imaging purposes, Figure 5.1c, reveals a microscopically heterogeneous structure made of discontinuous Au layers in the form of nanoparticles (bright spots) embedded in a TiO_2 matrix. However, the metasurface –

macroscopically and optically – behaves in a homogeneous manner while the small nanoparticle sizes ensure minimum light scattering, which would otherwise lead to visibility impairment.[166] We then characterised the optical and thermal properties of our surfaces. Figure 5.1d shows the transmittance, $\mathcal{T}$, reflectance, $\mathcal{R}$, and absorbance, $\mathcal{A}$, spectra of our superhydrophobic metasurfaces for normal light incidence in the 400–2200 nm wavelength range; covering most of the solar spectrum. The mean values of 62% for $\mathcal{T}$, 14% for $\mathcal{R}$ and 24% for $\mathcal{A}$ indicate that one can maintain a significant transparency level ($\mathcal{T}$ = 51% in the visible) with metasurfaces. (For more information on the optical properties of the control, see Appendix D, section "Transmittance, reflectance and absorbance spectra of control surfaces", and Figure D.2.) It is noted that the absorbance of the metasurfaces is broadband, extending over the entire solar spectrum. Figure 5.1e illustrates a sketch of the experimental configurations used in quantifying the thermal response of the superhydrophobic metasurfaces, consisting of a light source (halogen lamp or solar simulator, for low or high power density respectively; see Methods) illuminating our sample and either an infrared (IR) camera or a pair of thermocouples, measuring sample, T_s, and ambient, T_∞, temperatures. The spectra of both light sources are shown in the inset. Figure 5.1f shows plots of $T_s - T_\infty$ *vs* illumination time, t, for a superhydrophobic metasurface illuminated with the solar simulator, having a power density $P \approx 3.5$ kW m^{-2}, in comparison to a control surface. The maximum temperature increase (at $t = 300$ s) of ~16 °C for the metasurface, compared to ~5 °C for the control surface, demonstrates the profound effect of the metasurface in achieving remarkable heating performances, which can be employed to enhance water impalement resistance.

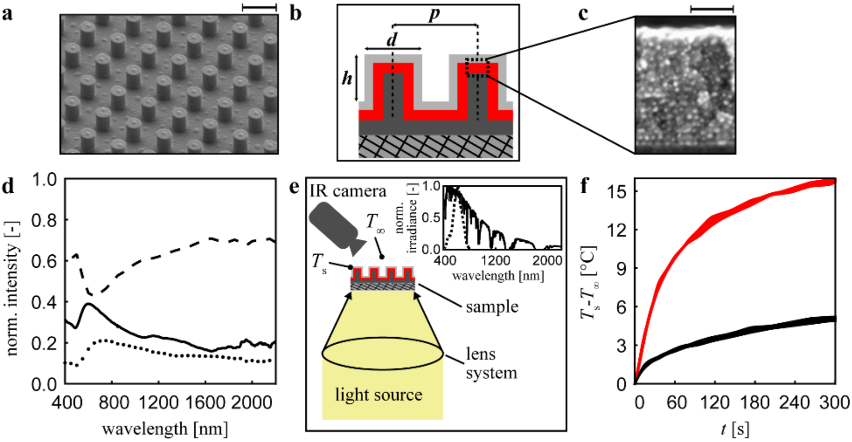

Figure 5.1 Superhydrophobic metasurface. (a) Micrograph showing the superhydrophobic metasurface from a tilted-view perspective. **(b)** Schematic of the superhydrophobic metasurface cross section, revealing its different layers, underlying surface texture (dark gray pillars), and glass substrate (crosshatch). The top layer (light gray) is a hydrophobic coating and the middle layer (red) is the metasurface coating. **(c)** Micrograph showing the cross section of a metasurface; the thickness here is exaggerated to facilitate imaging (the metasurface coating used throughout our study had a thickness of ~60 nm). The pillar diameter (*d*), height (*h*), and pitch (*p*) are shown in **b**. The sample in **a** has [*d*, *p*, *h*] = [2.5, 5.0, 3.3] µm. **(d)** Transmittance (– – –), reflectance (• • •), and absorbance (——) spectra of the superhydrophobic metasurface in **a**. **(e)** Schematic of the experimental setup used to measure the temperature change of the samples upon illumination. The normalized irradiances of the light sources we used in this study are shown as inset plots (solar simulator, ——; halogen lamp, - - -). **(f)** Surface temperature change relative to ambient, $T_s - T_\infty$, *vs* time, *t*, of the control (black curve; no metasurface, superhydrophobic sample) and superhydrophobic metasurface (red curve) samples. The samples are illuminated when $t > 0$ s with a solar simulator at a power density of $P \approx 3.5$ kW m^{-2}. Each line represents the range of values measured for three experiments ($N = 3$). Scale bars: **(b)**, 5 µm; **(c)**, 100 nm.

Figure 5.2a depicts a hot droplet (initial droplet temperature, $T_w = 70$ °C) impacting onto a superhydrophobic metasurface of ambient temperature ($T_\infty = 21$ °C), dispensed at a height of ~8 cm above the surface. The droplet had $We = 2\rho v^2 R_0 / \gamma \approx 26$ where ρ is the droplet density, v is the droplet velocity at the moment of impact, R_0 is the initial droplet radius and γ is the surface tension. The image sequence reveals that after the droplet departed the surface ($t = 37$ ms), a smaller remnant, or daughter droplet, was left behind; indicative of impalement during the contact and in contrast to the ambient droplet case, where no impalement was recorded (see Appendix D, section "Room temperature droplet impact on a superhydrophobic metasurface", and Figure D.3). This is attributed to condensation within the microtexture occurring in the case of the hot droplet and a bridging phenomenon, as discussed in previous works.[50,51] For Figure 5.2b, the experiment was repeated with the substrate now illuminated from below by the solar simulator. Here, we observed no impalement; demonstrating light-induced effective superhydrophobicity enhancement. A micrograph of the superhydrophobic plasmonic metasurface is included as an inset. Figure 5.2c quantifies the impalement probability, Φ, *vs* T_w, in both the light on and light off cases. At lower values of T_w, no impalement is observed for either case. However, for $T_w > 35$ °C, we note the onset of impalement in the light off case with increasing Φ for higher temperatures. Crucially, under illumination, $\Phi = 0$ for all T_w, showcasing the capability of light to hinder condensation-based impalement.

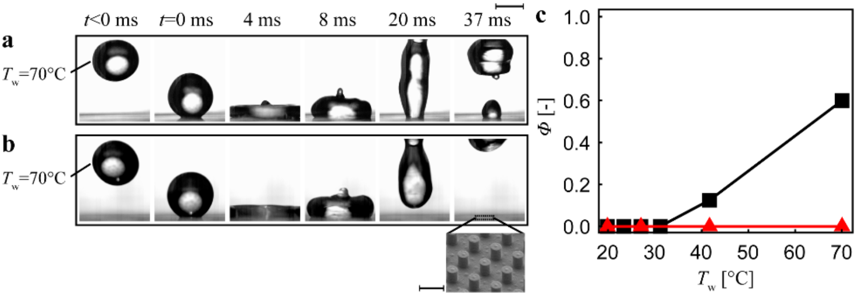

Figure 5.2 Light enhanced superhydrophobicity. Image sequences showing hot droplets impacting on superhydrophobic metasurfaces **(a)** without and **(b)** with illumination (solar simulator). The following parameters were kept constant for all droplet impact experiments here: $We \approx 26$, $P \approx 3.5$ kW m^{-2}, and $T_\infty \approx 21$ °C. A micrograph of the superhydrophobic metasurface is shown as an inset image. **(c)** Probability of droplet impalement, Φ, *vs* water droplet temperature, T_w, for no illumination (black squares) and under illumination (red triangles) conditions. Each data point represents $N \geq 7$ experiments. Scale bars: **(a)–(b)**, 2 mm; inset in **(b)**, 5 µm.

To quantify the dependence of impalement events due to condensation on T_s, we now placed hot droplets on our superhydrophobic metasurfaces and observed their wetting behavior over time. Figure 5.3a–c displays image sequences of single static hot droplets ($T_w = 55°C$), deposited at $t = 0$, for $T_\infty = 22°C \leq T_s \leq 28°C$. We used a halogen lamp to elevate T_s beyond T_∞. It is noticeable from Figure 5.3a–c that the impalement time, t_f, the time at which the contact line moves macroscopically, varies with T_s. As T_s increases, so does t_f. Once a droplet impales, the superhydrophobicity of the surface is compromised. For our square pillar array, we can calculate the theoretical time needed for condensate to fill a cavity, τ_f; it can be proven that with regards to textural features, τ_f only depends on the pillar height, scaling as h^2. Condensation is the outcome of supersaturation due to water vapor diffusion from the hot droplet into the cooler cavity. (For more information on the formula for calculating τ_f, see Appendix D, section "Theoretical basis of impalement criterion".) In Figure 5.3d, t_f *vs* τ_f for all T_w and T_s are plotted and least squares were used to extract the best fit lines. From these, it becomes clear that the slope of the lines, $\alpha = t_\mathrm{f} / \tau_\mathrm{f}$, which we term correction factor, depends on T_s. In agreement with previous research on hot droplets interacting with ambient substrates,[50] we found $\alpha\big|_{T_\mathrm{s}=T_\infty=22°\mathrm{C}} \approx 11$. However, for $T_\mathrm{s} > T_\infty$, we observed that α increases significantly to $\alpha\big|_{T_\mathrm{s}=28°\mathrm{C}} \approx 26$. The same trend was also followed by control surfaces, heated with a hot plate (see Appendix D, section "Effect of surface temperature on condensation nucleation on control surfaces due to warm water droplets", and Figure D.4). This can be attributed to a combination of factors. First, droplets cool down due to contact with the surface (conduction) and diffusion in air. We measured the cooling rate of hot droplets placed on our surfaces at $t = 0$ and used a modified Newton's cooling law to fit the experimental data: $T_\mathrm{w}(t) = T_\mathrm{s} + \left(T_{\mathrm{w},t=0} - T_\mathrm{s}\right)\exp\left(-k_\mathrm{c} t^c\right)$, where k_c and c were determined empirically (see Appendix D, section "Experimental setup and water temperature calibration", and Figure D.5). Here we can see that the cooling profile depends solely on $T_\mathrm{w} - T_\mathrm{s}$ and therefore varies for our different cases. From this it can be inferred that deviations in α accommodate the stronger cooling rate observed at lower initial T_s. Indeed, for the maximum value of $T_\mathrm{w} - T_\mathrm{s}$, a considerable cooling rate of $14\,°\mathrm{C\,s^{-1}}$ was measured leading to the highest α. Second, the differences between t_f and τ_f are also – to a lesser extent – affected by the observation method of contact line motion used for detecting impalement events. When superhydrophobicity is compromised, the kinetics of droplet wetting and creation of new surface area impose a delay on the actual impalement time and increase the values of α. Figure 5.3e schematically summarizes the evolution of condensation impalement over time within micropillared surface textures. For contact times $t << t_\mathrm{f} = \alpha\tau_\mathrm{f}$, the cavities are almost water-free and superhydrophobicity is maintained. As t and τ_f become comparable, water nucleation and condensation take place and the cavity is partially filled with water, while for even longer t, water completely fills the cavity and local superhydrophobicity is compromised.

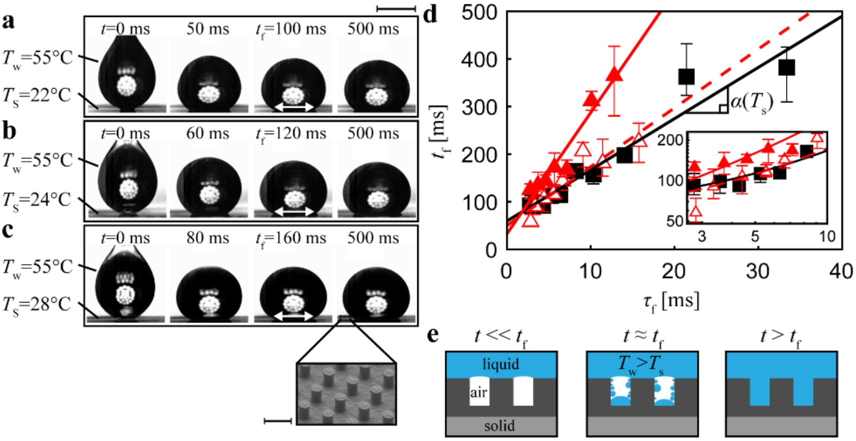

Figure 5.3 Interplay between light coupling, superhydrophobic metasurface, and warm droplet repellency. (a)–(c) Image sequences showing the wetting behavior of warm water droplets on a superhydrophobic metasurface for **a**, $P = 0$ kW m^{-2}, **b**, $P \approx 1$ kW m^{-2}, and **c**, $P \approx 2$ kW m^{-2} ($T_\infty \approx 22$ °C). We used the halogen lamp to illuminate the samples. **(d)** Droplet impalement time, t_f, *vs* theoretical cavity filling time, τ_f, for $T_s = 22$ °C (black squares and line), 24 °C (red open triangles and dashed red line), and 28 °C (red filled triangles and red line). Each data point represents $N = 3$ experiments, and the lower and upper error values represent the minimum and maximum measured values, respectively. The three lines of best fit have slopes of $\alpha \approx 11$ (for confidence $C = 95\%$, $\alpha = [8,13]$), 12 ($C = 95\%$, $\alpha = [8,17]$), and 26 ($C = 95\%$, $\alpha = [18,33]$) corresponding to $T_s = 22$ °C, 24 °C, and 28 °C, respectively. The inset, plotted in logarithmic axes, reveals the behavior of the warmest droplets. **(e)** Schematic showing the mechanism of condensation impalement that occurs when a warm droplet is placed on a superhydrophobic metasurface. Scale bars: **(a)–(c)**, 2 mm; inset in **(c)**, 5 µm.

In order to explore the coupling of pressure and condensation-based impalement mechanisms, we mapped the impalement probability of warm droplets impacting on our superhydrophobic metasurfaces for a range of We. The image sequences in Figure 5.4a–b depict droplets with $T_w > T_s$ impacting on a superhydrophobic metasurface at $We \approx 73$. For $T_s = T_\infty = 21$°C in Figure 5.4a, a slightly warmer droplet ($T_w = 26$ °C) was sufficient to cause impalement. This is in contrast to experimental results for $We \approx 26$, where we observed no impalement up to droplet temperatures of ~35 °C. However, upon illumination by our solar simulator, impalement was again suppressed. To investigate the underlying impalement mechanisms, we performed isothermal droplet impact experiments ($T_\mathrm{w} = T_\mathrm{s} = T_\infty$) at $We \approx 73$, which revealed a non-zero impalement probability. This can be attributed to a pure pressure-driven impalement mechanism. (See Appendix D, section “Effect of light on the pressure-driven impalement mechanism on metasurfaces” and Figure D.6.)

To predict impalement in dynamic droplet impact events, we define the contact time, τ_c, directly proportional to the inertial capillary time, τ, which scales as $R_0^{3/2}$ (see Appendix D, section “Theoretical basis of impalement criterion”). Figure 5.4c shows plots of impalement probability, *Φ*, *vs* $\tau_\mathrm{c} / \alpha\tau_\mathrm{f}$, for hot droplet impacts at $We = [26, 73]$, for both light on and light off cases. The $\tau_\mathrm{c} / \alpha\tau_\mathrm{f}$ ratio is our impalement criterion, with impalement transition expected to occur for $\tau_\mathrm{c} / \alpha\tau_\mathrm{f} \geq 1$. The corresponding droplet temperatures, T_w, for each value of $\tau_\mathrm{c} / \alpha\tau_\mathrm{f}$, are also plotted for both light on and light off cases. It is noted that for any given T_w, the respective $\tau_\mathrm{c} / \alpha\tau_\mathrm{f}$ value is lower in the light on case, signifying a greater impalement resistance. We observed this transition in the light off case at low We; on the other hand, illumination shifts the T_w required for impalement to temperatures higher than we could achieve with our setup. For the high We cases, the transition occurs at $\tau_\mathrm{c} / \alpha\tau_\mathrm{f} \approx 5 \cdot 10^{-2} \ll 1$. Illumination marginally increases *Φ*. This behavior can be explained by comparing the schematics in Figure 5.4d–e, which illustrate the condensation-based (low We) and mixed (high We) impalement mechanisms respectively. A high wetting pressure results in meniscus penetration, to a depth δ, into the texture during impact, effectively reducing the cavity height needed to be filled before impalement occurs to $h - \delta$. This greatly reduces the filling time, $\tau_\mathrm{f} \sim (h - \delta)^2$, resulting in a significant underestimation of $\tau_\mathrm{c} / \alpha\tau_\mathrm{f}$. It is therefore possible to use the same impalement criterion for a mixed mechanism by replacing h with $h - \delta$. Notwithstanding, determining the values of δ is beyond the scope of this study.

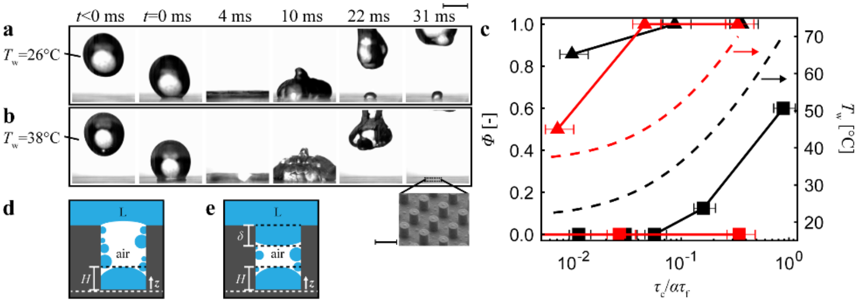

Figure 5.4 Mechanisms of light-enhanced superhydrophobicity. (a)–(b) Image sequences of warm water droplets on a superhydrophobic metasurface ($T_\infty \approx 21$ °C) for **a**, $We \approx 73$, $P = 0$ kW m^{-2}, and **b**, $We \approx 73$, $P \approx 3.5$ kW m^{-2}. A solar simulator was used for illumination. **(c)** Impalement probability, Φ (left axis), *vs* contact time to filling time ratio, $\tau_c/\alpha\tau_f$, for $We \approx 26$, $P = 0$ kW m^{-2} (black squares), $We \approx 26$, $P \approx 3.5$ kW m^{-2} (red squares), $We \approx 73$, $P = 0$ kW m^{-2} (black triangles), and $We \approx 73$, $P \approx 3.5$ kW m^{-2} (red triangles). The error bars are based on the confidence level in α (for confidence $C = 95\%$, $\alpha = [8,13]$ for the non-illuminated and $\alpha = [18,33]$ for the illuminated metasurfaces). Each data point represents $N \geq 7$ experiments. The dashed lines represent droplet temperature, T_w (right axis), *vs* $\tau_c/\alpha\tau_f$, for $P = 0$ kW m^{-2} (black dashed curve) and $P \approx 3.5$ kW m^{-2} (red dashed curve). (**d**)–(**e**) Schematics of impalement mechanisms; **d**, condensation-driven, and **e**, mixed condensation and pressure-driven. Scale bars: **(a)–(b)**, 2 mm; inset in **(b)**, 5 µm.

5.4. Conclusions

Loss of superhydrophobicity due to hot water condensation inside the texture of surfaces specifically designed for water repellency is an unwanted but common phenomenon which seriously inhibits their performance. The current state-of-the-art relies upon complex surface engineering, often at the expense of surface transparency. Here we demonstrated a facile and passive method of achieving superior repellency that can be applied to a broad range of surfaces, relying on the collaborative effect of superhydrophobicity and passive heating through plasmonic exploitation of incident sunlight. Harvesting the power of sunlight with ultrathin metasurfaces while maintaining transparency, we showed that typical microstructured surfaces, armed with our plasmonic coating, can sustain superhydrophobicity in the presence of very hot water by totally preventing or slowing down condensation nucleation due to light absorption heating. Our approach can be used as a stand-alone or additive technology towards counteracting the negative effects of hot water on surfaces, especially when a degree of optical transparency is required. We believe that our technology can make its advantages evident in applications such as glasses, goggles, optical components and a plethora of windows and windshields exposed to hot and humid conditions.

5.5. Methods

Materials. Microscope glass slides (76 by 26 mm, 1-mm thick, with cut edges and plain end) were obtained from VWR. Polydimethylsiloxane (PDMS) silicone elastomer and curing agent (Sylgard® 184, 10 to 1 ratio) were purchased from The Dow Chemical Company, and a UV-curable polyurethane acrylate (PUA) resin (MINS-311RM), composed of a functionalized pre-polymer, a photoinitiator and a UV-curable releasing agent, was obtained from Minuta Technology. Trichlorovinylsilane (TCVS, 97%), 1H,1H,2H,2H-perfluorodecyl acrylate (PFDA, 97%, with tert-butylcatechol inhibitor) and tert-butyl peroxide (TBPO, 98%) were sourced from Sigma-Aldrich.

Surface preparation.

a. *Metasurface-coated micropillared surfaces*. We fabricated a specially designed chrome hard mask consisting of 20 by 20 mm squares filled with circular dots with a target diameter of 2.5 µm and pitches ranging from ≈5 µm to ≈10 µm and used it to pattern 4-in silicon wafers with standard photolithography. We used a positive photoresist (AZ 4512; MicroChemicals GmbH) and the Süss MA6 mask aligner in hard contact mode for the UV exposure, and subsequently etched the wafers (deep silicon etch; PlasmaPro 100 Estrelas, Oxford Instruments) to a depth of 3.2 ± 0.1 µm. We then used initiated chemical vapor deposition (iCVD; iLab Coating System, GVD Corporation) to coat them with a thin and ultra-low surface energy pPFDA (9.3 mN m^{-1}) conformal hydrophobic polymer layer.[58] Upon a 10-min oxygen plasma ashing (100 W power; PCCE, Diener) of a wafer, we placed it in a glass chamber and ran a room temperature TCVS pre-treatment silanization process with initial pressure of ~13 kPa for 20 min, which would later enable chemical bonding of the pPFDA to silicon. For the iCVD deposition, the reactants were PFDA and the initiator TBPO, and the parameters were the following: deposition time of 15 min, process pressure of ≈13 kPa, PFDA flow rate of 1.0 sccm, TBPO flow rate of 2.6 sccm, substrate temperature of 40 °C. A heated filament at 300 °C enabled breakdown of the reactants. The next step consisted of transferring the wafer pattern onto a flexible PDMS mold by means of soft lithography, for the preparation of which we mixed PDMS with a curing agent at a 10:1 ratio, poured it onto the silicon wafer and degassed under vacuum to remove all air bubbles. Curing was done in a convection oven at 70 °C for 2 h. The mold, consisting of microholes, was peeled off the wafer. We then transferred the pattern from the flexible mold onto our substrates. We took microscope glass slides and thoroughly cleaned them, consecutively, in sonicated acetone, isopropyl alcohol and water baths, followed by plasma ashing for 10 min. Subsequently, we placed fractions of the PDMS mold onto thin layers of PUA resin, which we previously deposited on the glass slides. Curing and thus hardening of the pattern (micropillars) took place in a vacuum UV exposure box (Gie-Tec GmbH) for 10 min, followed by peeling off the PDMS molds. In order to deposit our light-absorbing metasurface coating on top of our structures, we employed sputter deposition (CS 320 C; Von Ardenne) method.[130] We first deposited ~20 nm of silicon dioxide by RF-bias and setting the following parameters: 600 W power, 0.2 Pa pressure, 5 sccm argon gas flow and deposition time of 42 s. SiO_2 promotes surface wettability and adhesion of the succeeding metasurface coating, also increasing its homogeneity and reducing the overall nanoroughness. On top of it, we ran deposition cycles with alternating titania (TiO_2) and gold (Au) targets, up to a total number of 8 layers. For each Au deposition burst, we operated the tool for 3 s at 50 W DC-bias and 0.6 Pa pressure, while each deposition of TiO_2 took 43 s, using a 600 W RF field at 0.6 Pa pressure. The metasurface was terminated with an extra TiO_2 layer, deposited for 72 s. Finally, the metasurface-coated PUA microstructured substrates were coated with a hydrophobic pPFDA layer in the same way as previously described in the case of silicon. Out of the pool of samples with different geometrical dimensions, we selected the ones with the following dimensions: $d \approx 2.5$ µm, $p \approx 5.0$ µm and $h \approx 3.3$ µm. The wetting fraction, $\varphi = \pi d^2 / 4p^2$, was ~20%.

b. *Control PUA micropillared surfaces.* We fabricated the control samples in the same manner as the metasurface-coated ones, with the only difference of omitting sputter deposition, meaning that curing of the PUA micropillars was directly followed by iCVD deposition of a hydrophobic pPFDA coating.

c. *Sample for metasurface cross section depiction.* To demonstrate the multilayer nature of our metasurface, we deposited the metasurface similar to the aforementioned procedure on a smooth silicon substrate, omitting the SiO_2 layer, since no dewetting issues were observed in this case. We kept all deposition parameters the same and adjusted the total number of layers to 44.

Characterization. We characterized the topography of the control and metasurface-coated samples by means of stylus profilometry (Bruker Dektak XT) and scanning electron microscopy (SEM; Hitachi SU8230). For the SEM micrographs of micropillars, we set the acceleration voltage at 1 kV and utilized the secondary electron and lower detectors to collect surface and topographic information. For the cross-sectional micrograph, we selected the aforementioned detectors and raised the voltage to 5 kV. We measured the advancing and receding contact angles on control and metasurface-coated samples with an OCA 35 goniometer (DataPhysics), with the tilting method and for droplet volume of 10 µL. We carried out transmittance, reflectance and absorbance measurements on control and metasurface-coated specimen with the help of a V-700 (Jasco) UV-VIS spectrometer with an integrating sphere.

Experimental setup and protocols. We conducted surface temperature calibrations using either a high-speed infrared camera (SC7500, FLIR), for the control and metasurface-coated samples illuminated with halogen light (Flexilux 600 longlife), with $P \approx 1$ kW m^{-2} and $P \approx 2$ kW m^{-2}, or a resistance temperature detector in the case of stronger illumination with a xenon arc source (66902, Newport), equipped with an AM1.5 air mass filter to render it a solar simulator, with $P \approx 3.5$ kW m^{-2}. The diameter of the light spot was ~8 mm for halogen light and >2 cm for the solar simulator. With the latter, we were able to homogeneously illuminate the whole sample. We assumed thermal equilibrium at $t = 300$ s (light was switched on at $t = 0$ s) and each measurement was run three times. Light from the solar simulator was stabilized by waiting for at least 30 min prior to running any experiments. (See Figure 5.1e–f for a schematic of the experimental configuration during calibration and the temperature increase caused by the solar simulator on control and metasurface-coated samples.) We performed the hot droplet experiments on warm surfaces only upon the illuminated surfaces reached thermal equilibrium and waited ~1 min between subsequent droplet dispensations. (See Appendix D, section “Experimental setup and water temperature calibration” and Figure D.5, for more details on the experimental setups used for calibrating the water temperature and running the hot droplet experiments.) The droplet placement or impact position on a sample was shifted after every experiment to ensure minimum effect of surface defects on our experiments and statistics. The relative humidity of the room was kept in the 45%–55% range throughout the studies.

5.6. Acknowledgments

Partial support of the Swiss National Science Foundation under grant number 162565 and the European Research Council under Advanced Grant 669908 (INTICE) are acknowledged. E.M. thanks Vidic J. for technical support in the experimental setups and Drechsler U. for assistance in surface fabrication.

6. CONCLUSIONS

With this thesis, I prove that sunlight can have a significant positive effect in surface anti-wettability, as well as prevention of fogging and icing of surfaces, all while maintaining transparency and solely relying on renewable energy.

In Chapter 3 of my thesis, I demonstrated that rationally engineered metamaterial-coated surfaces with tunable levels of transparency and significant light absorption, ranging from 28% to 83%, show impressive anti-icing and deicing performances. The metasurfaces, engineered for broadband light absorption, can lead to a > 10 °C temperature increase with respect to uncoated surfaces. Deicing can be achieved in as little as 30 s, while their anti-icing performance is equally significant, with 6 orders of magnitude increase in freezing delay in extreme subzero temperatures of < -30 °C. All in all, using intricately engineered metasurfaces to absorb sunlight, I propose a totally passive solution to icing, 100% based on renewable energy from the sun.

In the next chapter, the problems associated with fogging of surfaces and a fresh way of tackling them with sunlight and the technology I previously developed are investigated. Firstly, quantified data of clarity and distortion of light transmitted through surfaces with water condensate on them show that depending on their wettability, one can have different levels of visibility. Importantly, it was found that state-of-the-are superhydrophilic technologies do not retain a good level of surface visibility, resulting in significant distortions over time. Using metasurfaces on transparent substrates, we show that one can harness the broadband sunlight to maintain fog-free conditions for prolonged times. This is due to the temperature increase at the surface–water interface upon illumination. In fact, a reduction in defogging time by up to 4-fold was possible just relying on solar energy. These results open up new opportunities for future transparent and effective anti-fogging coatings.

The final chapter employs the metasurface technology and rational surface engineering to create super-repellent surfaces that work against condensation nucleation of hot water by increasing their temperature with sunlight. Even 1 °C can make a tremendous difference of several orders of magnitude in the probability of nucleation. Not only do I demonstrate significantly improved water repellency with sunlight, but I also investigate the driving forces behind the temperature shift of the onset of impalement that was observed experimentally.

7. OUTLOOK

In my thesis, I tried to provide the scientific community not only with quantitative answers to whether or not sunlight can help mitigate fog, ice and in general any water presence on surfaces, but my intention was also to open up new perspectives on how to solve problems with renewable energy, which will hopefully lead to further research and novel ideas on improving the performance of light-absorbing surfaces.

First and foremost, since the requirement for transparency is vital in many industrial and practical applications, it is wise more research to be conducted on the development of spectrally selective absorbers. Sunlight radiation has a lot of power in the infrared that is invisible to human eyes, roughly 50% or 500 W m^{-2}. Ideally, a surface that absorbs in the whole infrared and is transparent in the visible range would have – at least – the same performance as our metasurfaces while looking like plain glass, not reducing visibility to the slightest extent. This is challenging to make with current technologies without going deep into the field of plasmonics and nanostructures. More research could lead to scalable technologies that can be applied broadly on actual surfaces. This is exactly, in my opinion, what the secondary focus of relevant research should be. It is much more difficult to develop a scalable coating than following a cleanroom process to develop millimeter-scale samples.

In terms of designing surfaces maintaining superhydrophobicity even under adverse conditions (high air temperature and humidity), more research should be conducted to fabricate light-driven hot water-repellent surfaces with multi-tier roughness for reversible wettability by means of water droplet ejection off surface structures with the help of sunlight. This would be crucial in cancelling out visibility loss of surfaces in cases of intermittent sunlight. Such multi-tier micro and nanorough surfaces would enable visibility restoration with a minimal amount of sunlight, while also preventing condensate nucleation within the texture.

It goes without saying that harvesting sunlight is the way to proceed in all of these cases, not only for environmental protection reasons but also for enhanced practicality, as conventional energy is not always available on-site, or the costs associated with transferring it onto surfaces, for example windows, are high and require complicated engineering solutions. However, this is not to say that novel approaches should not be compatible with conventional technologies. On the contrary, only if the current tools that we have are appreciated could one break the records in water repellency, anti-fogging and anti-icing performances.

APPENDIX A

Modeling light absorption. The absorption behavior of the multilayer films can be modeled by treating each film as a homogeneous nanocomposite of Au and TiO₂, since the values of p (distance between adjacent gold particles) and d (mean particle diameter) are of the same order. According to Bruggeman's effective medium approximation, the effective electric permittivity of the nanocomposite – important in determining the electronic and optical properties of the nanocomposite – which is strongly dependent on the wavelength of light, is given by:[71]

$$\varepsilon_{\mathrm{r,nc}} = \frac{1}{4}\left\{\left(3v_{\mathrm{Au}}-1\right)\varepsilon_{\mathrm{r,Au}} + \left(3v_{\mathrm{TiO_2}}-1\right)\varepsilon_{\mathrm{r,TiO_2}} \pm \sqrt{\left[\left(3v_{\mathrm{Au}}-1\right)\varepsilon_{\mathrm{r,Au}} + \left(3v_{\mathrm{TiO_2}}-1\right)\varepsilon_{\mathrm{r,TiO_2}}\right]^2 + 8\varepsilon_{\mathrm{r,Au}}\varepsilon_{\mathrm{r,TiO_2}}}\right\} \tag{A.1}$$

where $\varepsilon_{\mathrm{r,nc}}$ is the relative effective permittivity of the nanocomposite, $\varepsilon_{\mathrm{r,Au}}$ and $\varepsilon_{\mathrm{r,TiO_2}}$ are the permittivities of Au and TiO_2, respectively, and v_{Au} and $v_{\mathrm{TiO_2}}$ are the volumetric concentrations of Au and TiO_2, respectively. We select the sign of equation (A.1) to assure that the imaginary part of the permittivity stays positive. We also assumed spherical Au nanoparticles, with a mean diameter of $d \approx 5$ nm, taken from the measured Au particle size distribution (Figure 3.1b). The volumetric concentration of Au was $v_{\mathrm{Au}} \approx 0.4$, therefore $v_{\mathrm{TiO_2}} \approx 0.6$. The dielectric constant of TiO_2 in the visible and near-infrared wavelength range can be taken as $\varepsilon_{\mathrm{r,TiO_2}} = 6.25$.[95] The calculation of $\varepsilon_{\mathrm{r,Au}}$, which has dependency on the particle size, is discussed below. The permittivity of a bulk metal can be written as:

$$\varepsilon_{\mathrm{r,bulk}} = \varepsilon_{\mathrm{r,bound}} + \varepsilon_{\mathrm{r,free}} \tag{A.2}$$

where $\varepsilon_{\mathrm{r,bound}}$ is the term related to the bound electrons and $\varepsilon_{\mathrm{r,free}}$ is the term related to the free electrons. Furthermore, we have:

$$\varepsilon_{\mathrm{r,free}} = 1 - \omega_{\mathrm{p}}^2 / \left(\omega^2 + i\omega\gamma_{\mathrm{bulk}}\right) \tag{A.3}$$

where $\omega_{\mathrm{p}} = 1.3\cdot 10^{16}$ s^{-1} is the bulk plasma frequency, ω is the frequency of incident light and $\gamma_{\mathrm{bulk}} = 1.64\cdot 10^{14}$ s^{-1} is the damping constant according to the Drude model. From (A.2), (A.3), and the known bulk permittivity function of gold, the term $\varepsilon_{\mathrm{r,bound}}$ can be calculated.[167] For $d < 50$ nm (mean free path of electrons in Au), surface properties become important and the corrected damping constant is given by:[168]

$$\gamma^* = \gamma_{\mathrm{bulk}} + 2Cv_{\mathrm{F}} / d \tag{A.4}$$

where $v_F = 14.1 \cdot 10^{14}$ nm s^{-1} is the Fermi velocity and a scattering constant, $C = 0.33$,[169] was assumed. Replacing γ_{bulk} with γ^* in (A.3) gives us the size-dependent permittivity of Au nanoparticles (A.2). Finally, from equation (A.1), the relative effective permittivity of the metasurface, $\varepsilon_{\text{r,nc}}$, can be calculated.

The same analysis is also valid for other common dielectrics used in metal-dielectric nanocomposites, such as silicon dioxide (dielectric constant of ≈ 2.25) and Teflon (dielectric constant of ≈ 1.8).[95]

Figure A.1a shows a plot of the imaginary part of the relative permittivity, $\text{Im}(\varepsilon_{\text{r,bulk}})$, of bulk Au and Au nanoparticles ($d \approx 5$ nm), *vs* wavelength of light, λ ($400-1200$ nm).

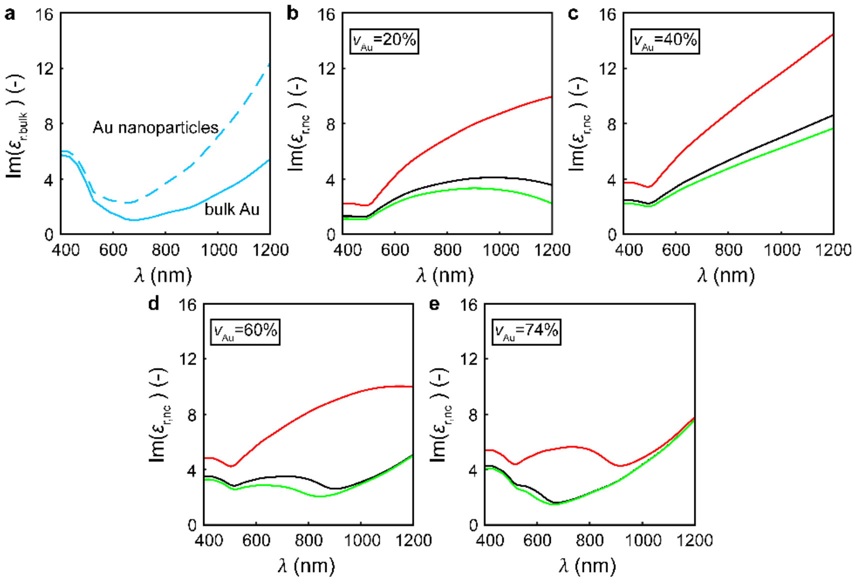

Figure A.1 (a) Imaginary part of the relative permittivity, $\text{Im}(\varepsilon_{\text{r,bulk}})$, of bulk Au (——) and Au nanoparticles ($d \approx 5$ nm, – – –), *vs* wavelength of light, λ. **(b)–(e)** Imaginary part of the relative effective permittivity of Au–dielectric nanocomposites, $\text{Im}(\varepsilon_{\text{r,nc}})$, *vs* λ, for different volumetric concentrations of Au nanoparticles ($d \approx 5$ nm), v_{Au}: **(b)** 20%, **(c)** 40%, **(d)** 60%, **(e)** 74%, each for three commonly used dielectrics (TiO_2 ——, silicon dioxide ——, and Teflon ——).

Figure A.1b–e show plots of the imaginary part of the relative effective permittivity, $\mathrm{Im}(\varepsilon_{\mathrm{r,nc}})$, of nanocomposites consisting of Au nanoparticles ($d \approx 5$ nm) and commonly used dielectrics (here shown for TiO_2, silicon dioxide and Teflon), *vs* wavelength of light, λ ($400-1200$ nm), for different Au volumetric concentrations, ranging from 20% up to 74% (maximum packing factor for close-packed, equal-size spheres). We observe that the size effects on Au nanoparticles lead to a significantly increased imaginary part of the permittivity, compared to bulk Au. The target for broadband visible light absorption in a nanocomposite is maximization of the value of $\mathrm{Im}(\varepsilon_{\mathrm{r,nc}})$ across the whole visible wavelength range.[71] This is equivalent to maximizing the effective electronic conductivity of the nanocomposite, $\sigma_{\mathrm{c,nc}}$ ($\sigma_{\mathrm{c,nc}} = \omega \mathrm{Im}(\varepsilon_{\mathrm{r,nc}})$). Close to percolation, for $v_{\mathrm{Au}} = 40\%$, $\mathrm{Im}(\varepsilon_{\mathrm{r,nc}})$ becomes very large over the whole wavelength range, and so does $\sigma_{\mathrm{c,nc}}$. The percolation threshold (volumetric concentration) for 3D nanocomposites is 1/3, while for deeply sub-wavelength, 2D films, it is approximately equal to 1/2.[71] From the calculated curves (Figure A.1b–e) as well as the above-mentioned theoretically expected v_{Au} at percolation, we see that the optimum v_{Au} is $\approx 40\%$, for all the considered dielectrics. Moreover, it is notable that for the above-mentioned volumetric concentration, the Au–TiO_2 nanocomposite exhibits the highest and most broadband imaginary part of the permittivity, as compared to the nanocomposites with silicon dioxide and Teflon, which led us to select TiO_2 as the dielectric in all of our studies.

Nanoparticle size analysis. The particle size distribution of the gold nanoparticles was extracted from an 8-layer ($L = 45$ nm, without a TiO_2 top-layer) sample. Figure A.2a shows the first approach, which is a manual measurement process. The length of the drawn (yellow) line segments gives the equivalent particle diameter, d. A total of 241 particles were measured in the displayed image.

The second approach is facilitated by using ImageJ software package. First, we threshold the 8-bit image using Yen's thresholding method.[170,171] This method is an improvement over the triangle method, being able to detect data skewness to the one side or the other. Then, for the particle size calculations, we apply a limit of 1–100 nm^2 in the area and 0.1–1.0 in the circularity, to prevent merging artifacts of neighboring nanoparticles. Finally, the area (red contours in Figure A.2b) is converted into equivalent diameter, assuming spherical nanoparticles. OTSU method[172] was also tried but the detection was not up to par with Yen's method. The quantitative comparison between manual and automatic measurements is shown in the particle size distribution bar plot (Figure A.2c). The average particle diameter is ≈ 5 nm in both cases. The automatic method enables fast processing of much bigger areas. For low contrast images, though, it is intuitive that manual measurements are the most reliable.

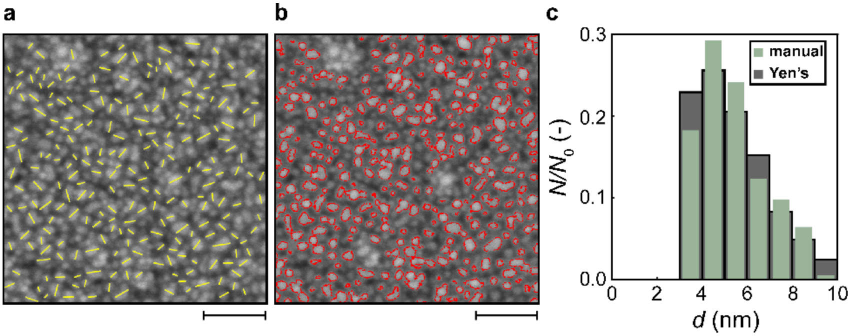

Figure A.2 Particle size distribution of the gold nanoparticles (top-view of the $L = 45$ **nm, 8-layer metasurface, without TiO_2 top-layer). (a)** Manual counting: the length of the line segments is the equivalent diameter. **(b)** Automatic measurement using Yen's thresholding method. The equivalent diameter is calculated from the area of each nanoparticle, assuming unity sphericity. **(c)** Particle size distribution comparison bar graphs (relative frequency, N / N_0, *vs* particle diameter, d) between the two methods. The mean particle diameter is ≈ 5 nm in both cases. Scale bar: **(a)–(b)** 40 nm.

Optical spectroscopy. Figure A.3a–d shows the experimental absorption ($\mathcal{A}$), reflection ($\mathcal{R}$) and transmission ($\mathcal{T}$) spectra of metasurfaces with $L = 38$, 60, 95 and 270 nm over the wavelength range: $\lambda = 400 - 800$ nm. Figure A.3e shows the corresponding spectra of $\mathcal{A}$, $\mathcal{R}$ and $\mathcal{T}$, *vs* λ, for a semi-transparent, PVDF-coated metasurface with $L \approx 60$ nm, and the same uncoated metasurface. The mean values of $\mathcal{A}$, $\mathcal{R}$ and $\mathcal{T}$ over the whole spectrum, denoted as $\overline{\mathcal{A}}$, $\overline{\mathcal{R}}$ and $\overline{\mathcal{T}}$, respectively, are also shown.

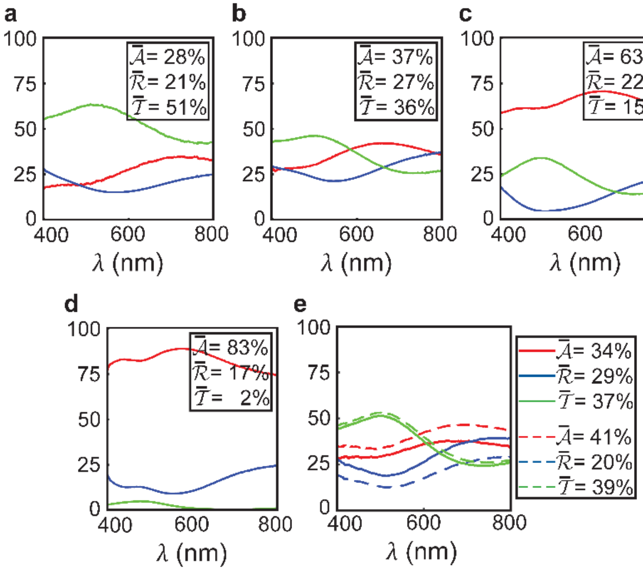

Figure A.3 Percent absorption, $\mathcal{A}$ (—), reflection, $\mathcal{R}$ (—) and transmission, $\mathcal{T}$ (—), *vs* wavelength of light, λ, for metasurfaces with varying *L*. (a) 38 nm, **(b)** 60 nm, **(c)** 95 nm, **(d)** 270 nm, and **(e)**, ≈ 60 nm, uncoated (solid curves) and PVDF-coated (dashed curves). $\overline{\mathcal{A}}$, $\overline{\mathcal{R}}$, $\overline{\mathcal{T}}$ are the mean values of $\mathcal{A}$, $\mathcal{R}$ and $\mathcal{T}$, respectively.

Thermography. The methodology of measuring the surface temperature of our samples (fabricated on fused silica substrates) under visible light illumination with non-contact infrared measurements, is described in this section. The total, spatially changing signal (C_{tot} , expressed in digital counts) collected by the IR camera at each time moment can be formulated as:

$$C_{\mathrm{tot}}(x,y)=\varepsilon(x,y)C_{\mathrm{s}}(x,y)+\left[1-\varepsilon(x,y)\right]C_{\mathrm{amb}}(x,y) \tag{A.5}$$

where ε is the sample emissivity, C_{s} is the number of counts (signal) that the sample would exhibit if it was a blackbody (emissivity of 1), and the term $C_{\mathrm{amb}}(x,y)$ is due to the ambient contribution. Here, we made the assumption that the infrared transmittance of air is unity, therefore, its contribution can be neglected (IR camera lens–sample distance was 30 cm). Moreover, the assumption of zero infrared transmittance through the sample should also be made so that equation (A.5) remains valid. The validity of this assumption for all the samples will be discussed later. We consider each metasurface as an effective medium, therefore ε has no spatial distribution, so that equation (A.5) becomes:

$$C_{\mathrm{tot}}(x,y)=\varepsilon C_{\mathrm{s}}(x,y)+(1-\varepsilon)C_{\mathrm{amb}}(x,y) \tag{A.6}$$

Applying (A.6) for two different temperatures, T_{amb} (ambient temperature) and $T_{\mathrm{i}}>T_{\mathrm{amb}}$, and subtracting the resulting equations, leads to:

$$C_{\mathrm{tot}}^{\mathrm{T_i}}(x,y)-C_{\mathrm{tot}}^{\mathrm{T_{amb}}}(x,y)=\varepsilon\left[C_{\mathrm{s}}^{\mathrm{T_i}}(x,y)-C_{\mathrm{s}}^{\mathrm{T_{amb}}}(x,y)\right] \tag{A.7}$$

This is because the ambient term is temperature independent.

In order to calculate the unknowns in equation (A.7) starting with ε , we ran a series of calibration experiments: each sample was placed on a hot plate (without illumination); the temperature was increased in steps; the resulting total counts per sample and temperature increment were recorded with the IR camera. A type T thermocouple (accuracy of ±0.5 °C) was used to measure the surface temperature of the samples. The range of surface temperatures was 23–46 °C. To minimize the effect of sample transmittance on the reading of total counts, a low emissivity polished aluminum bottom plate ($\varepsilon_{\mathrm{Al}}\approx 0.1$) [173] was used in all cases. (The same experiments were also run on a high emissivity bottom plate made of PMMA ($\varepsilon_{\mathrm{PMMA}}\approx 0.95$) [174], for maximum error estimation reasons, as discussed below.) We tried to minimize any convective heat transfer that could take place, as well as the noise level (temporally and spatially changing signal from external IR sources, like the human body) by encapsulating the surroundings of each sample and the camera prior to its calibration. There are three unknowns in equation

(A.7) ε, $C_{\mathrm{s}}^{\mathrm{T_i}}$ and $C_{\mathrm{s}}^{\mathrm{T_{amb}}}$. The latter two can be calculated by taking into account the internal calibration curve of the IR camera, shown in Figure A.4a; digital level in the case of blackbody, expressed in counts, C_{cal}, *vs* temperature, T :

$$C_{\mathrm{cal}} = f_{\mathrm{cal}}\left(T\right) \tag{A.8}$$

Combining equation (A.7) with (A.8), and setting $C_{\mathrm{cal}} = C_{\mathrm{s}}$, the unknown sample emissivity, ε, can be calculated. In our case, ε was in the 0.68–0.90 range.

In order to extract the spatial and temporal evolution of the temperature of each sample under illumination, the first frame (ambient term) from each image sequence was subtracted. After finding the average pixel coordinates with the maximum intensity from the whole sequence, a circular geometric place with a radius of 5 pixels around the maximum was considered and its average intensity (signal) per frame, $C_{\mathrm{s}}^{\mathrm{T_i}}$, was calculated. Finally, signal was converted into temperature by using the expressions (A.7) and (A.8).

Figure A.4b shows the spatial temperature profile of an IR measurement (metasurface with $L = 270$ nm) at $t = 180$ s (steady state). Figure A.4c is a plot of temperature increase, ΔT, *vs* radial position, r, with respect to the position of the maximum temperature ($r = 0$) of the aforementioned metasurface, at $t = 180$ s (steady state).

The main sources of error affecting the infrared measurements are, first of all, the uncertainty in the sample calibration (emissivity calculation), due to the uncertainty in the temperature measurements (± 0.5 °C), secondly, the effect of the transmittance of the samples used in the calibration, thirdly, the systematic error in the camera internal calibration curve. To account for the error due to transmittance of the samples during calibration, we compared the maximum ΔT upon illumination, between the cases in which an aluminum bottom plate (low emissivity) was used for calibration and the ones in which a PMMA bottom plate (high emissivity) was used. We obtained a maximum error of ± 0.4 °C for the sample with the highest transparency, indicating some IR transmittance through the sample, which contributes to the total error. Moreover, the influence of the temporal fluctuation of the ambient radiation should be taken into account.[175] We minimized this effect by carefully shielding the setup throughout the measurements. Based on the above considerations, a maximum uncertainty of ± 0.6 °C is calculated for the infrared temperature measurements in the temperature range of our experiments.

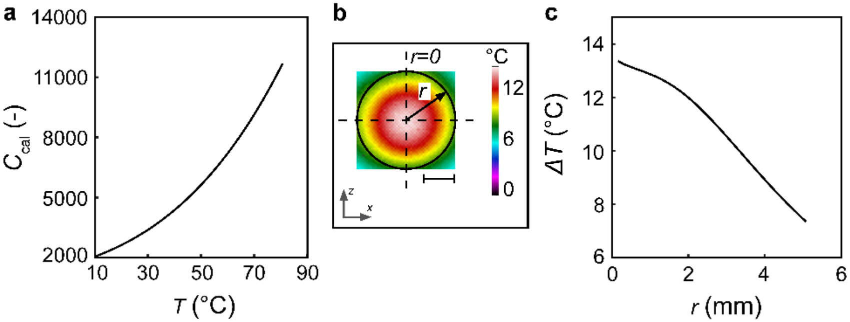

Figure A.4 Infrared temperature calculations. (a) Calibration curve of the IR camera, in the $10-80$ °C temperature range (digital level, C_{cal}, *vs* temperature, T). **(b)** Surface temperature calculations: a circle with a radius of r (exaggerated) is drawn around the maximum; the geometric place defined by it gives the average temperature per frame. **(c)** Temperature increase, ΔT, at a radial distance, r, from the position of the maximum temperature (metasurface with $L = 270$ nm). Scale bar: **(b)** 3 mm.

Heat transfer. For horizontal upward facing heated plates, the three-dimensionality of the buoyancy driven flow limits the ability to develop generalized correlations in order to determine *h*, therefore we computed the steady-state value of ΔT using COMSOL Multiphysics Modeling Software.

In order to understand the importance of heat transfer from the heated substrate into the gaseous environment in determining the steady-state value of ΔT, we solved the two-dimensional energy, momentum, and continuity equations using COMSOL Multiphysics Modeling Software. Figure A.5a shows a schematic of a gas cavity of height L_1 and width L_2 subjected to gravity, with a heated bottom, adiabatic side-walls, and a constant temperature top wall. The energy, continuity, and momentum equations can be written as:

$$\frac{\partial T}{\partial t} + \mathbf{u}\cdot\nabla T = \alpha\nabla^2 T,$$
$$\frac{\partial \rho}{\partial t} + \nabla\cdot(\rho\mathbf{u}) = 0,$$
$$\rho\frac{\partial \mathbf{u}}{\partial t} + \rho(\mathbf{u}\cdot\nabla)\mathbf{u} = \nabla\cdot\left\{-p_v\mathbf{I} + \mu_a\left[\nabla\mathbf{u} + (\nabla\mathbf{u})^{\mathrm{T}}\right] - \frac{2}{3}\mu_a(\nabla\cdot\mathbf{u})\mathbf{I}\right\} + \mathbf{F} + \rho\mathbf{g} \tag{A.9}$$

with the following initial and boundary conditions, $T(x,y,0)=T_\infty$, $\frac{\partial T}{\partial y}(x,0,t)=-\left(P\overline{\mathcal{A}}-P^*\right)/k_\mathrm{s}$, $\frac{\partial T}{\partial y}(0,y,t)=\frac{\partial T}{\partial y}(L_2,y,t)=0$, $T(x,L_1,t)=T_\infty$, $u(x,0,t)=0$, $u(0,y,t)=0$, $u(x,L_1,t)=0$, $u(L_2,y,t)=0$, and $u(x,y,0)=0$, where α, ρ, and μ_a are the thermal diffusivity, density, and dynamic viscosity of the gas, u is gas velocity, p_v is pressure, P^* is the total irradiated power from the sample, $\mathbf{I}$ is the identity matrix, $\mathbf{g}$ is the acceleration due to gravity, and $\mathbf{F}$ is the force per unit volume. P^* is temperature-dependent and can be calculated by the Stefan-Boltzmann law, $P^*=\varepsilon\sigma_\mathrm{B}\left[T_\mathrm{av}^4(y=0,t)-T_\infty^4\right]$, where σ_B is the Stefan-Boltzmann constant. For simplification reasons, the average sample temperature, $T_\mathrm{av}(y=0,t)$, per time step is considered in the calculation of P^*. Plugging in appropriate values ($L_2=1.8$ cm, $P\approx 2.4$ kW m^{-2}, $\overline{\mathcal{A}}=37\%$, $T_\infty=23$ °C, $\varepsilon=0.8$, $p_\mathrm{v}=1$ atm, $g=9.81$ m s^{-2}), we run the simulations for various cavity heights, L_1. Here, heat in was simplified as $\approx P\overline{\mathcal{A}}$ due to the broadband $\mathcal{A}$ *vs* λ spectrum of the metasurface; no renormalization with respect to the spectrum of the light source was applied. This simplification will also be used further on.

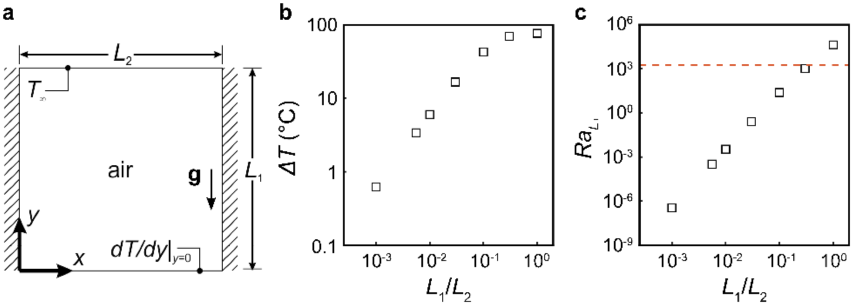

Figure A.5 Modeling steady-state temperature of a heated surface in contact with a two-dimensional rectangular gas cavity. (a) Schematic of the air cavity subjected to gravity with a heated bottom, adiabatic side-walls, and a constant temperature top-wall. **(b)** Temperature differential at steady state, $\Delta T=T(x,0)-T_\infty$, *vs* cavity aspect ratio, L_1/L_2 ($L_2=1.8$ cm), for $dT/dy|_{y=0}=-(P\overline{\mathcal{A}}-P^*)/k_\mathrm{s}$ ($P\approx 2.4$ kW m^{-2}, $\overline{\mathcal{A}}=37\%$, $P^*\approx 34$ W m^{-2} and $k_\mathrm{s}=0.2$ W m^{-1} K^{-1}). **(c)** Rayleigh number, Ra_{L_1} ($Ra_{L_1}=g\beta\left[T(x,0)-T_\infty\right]L_1^3/(\nu\alpha)$), at steady state, *vs* cavity aspect ratio, L_1/L_2. The dashed line represents the critical Rayleigh number, $Ra_\mathrm{c}=1708$.

Figure A.5b shows a plot of $\Delta T=T(x,0)-T_\infty$ *vs* cavity aspect ratio, L_1/L_2, at steady state conditions. It is clear that by increasing L_1/L_2 an increase in ΔT is observed, indicating that we are primarily in a conduction regime, and that the experimentally measured value of $\Delta T \approx 7$ °C corresponds to $L_1 / L_2 \approx 1.2 \cdot 10^{-2}$. L_1 can be estimated from Fourier's heat conduction law, subtracting the power lost due to radiation, as $L_1 \approx \Delta T k_\mathrm{a} / \left(P\overline{\mathcal{A}} - P^*\right)$, where k_a is the thermal conductivity of air. Substituting appropriate values ($\Delta T \approx 7$ °C, $k_\mathrm{a} \approx 2.63 \cdot 10^{-2}$ W m^{-1} K^{-1}, $P \approx 2.4$ kW m^{-2}, $\overline{\mathcal{A}} = 37\%$) yields $L_1 \approx 216$ µm. Here, $P^* \approx 34$ W m^{-2} ($\varepsilon = 0.8$, $\sigma_\mathrm{B} = 5.6704 \cdot 10^{-8}$ W m^{-2} K^{-4}, $T(x,0) \approx 30$ °C, $T_\infty = 23$ °C). In order to predict the worst-case scenario, we also consider the metasurface with $\overline{\mathcal{A}} = 83\%$, which leads to a surface average temperature increase, $\Delta T_\mathrm{s} \approx 8$ °C, based on the infrared temperature measurements, and also the fact that only a fraction of the sample is illuminated. In that case, heat in is $P_\mathrm{f}\overline{\mathcal{A}} \approx 180$ W m^{-2}, where P_f is the surface average power density, and heat out is $P^* \approx 49$ W m^{-2}, so that $P^* \approx 0.27 P_\mathrm{f}\overline{\mathcal{A}}$. Therefore, heat transfer through radiation, typically in the order of $< 10\%$ for low temperature differences, can become important. The temperature in the sample must be determined by a balance of heat in due to light absorption and heat out due to conduction into the surrounding gas layer and radiation to the environment. To estimate the contribution of convection (metasurface with $\overline{\mathcal{A}} = 37\%$), we calculate the Rayleigh number, a measure of the importance of heat convection and conduction, as $Ra_{L_1} = g\beta\left(\mathrm{T}(x,0) - T_\infty\right) L_1^3 / (\nu\alpha)$, where ν is the kinematic viscosity of air and β is the volumetric expansion coefficient which for an ideal gas can be approximated as $1/T_\infty$ (conservative estimate for the maximum value of Ra_{L_1}; $\beta \approx 3.38 \cdot 10^{-3}$ K^{-1}, $v \approx 1.57 \cdot 10^{-5}$ m^2 s^{-1}). Figure A.5c shows a plot of Ra_{L_1} *vs* L_1 / L_2; for the values we are interested in ($L_1 / L_2 \approx 1.2 \cdot 10^{-2}$ and $\Delta T \approx 7$ °C), $Ra_{L_1} \approx 7 \cdot 10^{-3}$, which is well within the regime where heat conduction dominates convection ($Ra_{L_1} \approx 7 \cdot 10^{-3} < Ra_\mathrm{c} = 1708$).[96] In total, we showed that heat conduction to the surrounding gas, as well as, in certain cases, radiation, are the dominant mechanisms of heat transfer, apart from conduction to the substrate (it was shown before).

Ice adhesion setup. In Figure A.6a, the in-house ice adhesion chamber that was used for the ice adhesion measurements and the de-icing experiments is depicted. The applied force results in an interfacial shear stress. The distance between the force probe and the surface of the sample was the lowest possible, ≈ 1 mm, being the same throughout all experiments. This is of high importance, as it has been previously shown that increasing this distance results in a transition from a pure shear mode to a mixed shear and tensile mode.[176] All samples had a PVDF-coated surface, ensuring no water leakage from the bottom side of the polypropylene cylinder, in case that the weight of the cylinder was not overcome by the hydrostatic pressure of water. The cylinder was filled up to a height of 1 cm. Figure A.6b shows the calibration curve (force, F, *vs* voltage, U) of the piezoelectric force sensor, that was constructed by placing different test weights on a base probe with a diameter of 3 mm, the same as the diameter of the force probe, as the output signal exhibits a slight dependence on the area that the force is applied.

Figure A.6c shows a typical ice adhesion measurement (shear stress, τ_{yx}, *vs* displacement, δ) on a PVDF-coated control sample, at $T = -4$ °C and a constant displacement rate, $V = 1$ μm/s. The detected maximum force at the moment of adhesive failure gives the ice adhesion strength. The values of τ_{yx} are calculated by dividing the determined force with the projected ice–substrate contact area.[21] This contact area, for a cylinder radius $R = 1.5$ mm, equals to: $A_c = \pi R^2 \approx 7.1$ mm^2. It has to be noted that a reduction of $< 10\%$ in the measured value of a constant force is to be expected, related to the sensor specifications: drift of $< 5\%$ per logarithmic time scale and linearity error of $< 5\%$. This behavior is characteristic in piezoelectric sensors.

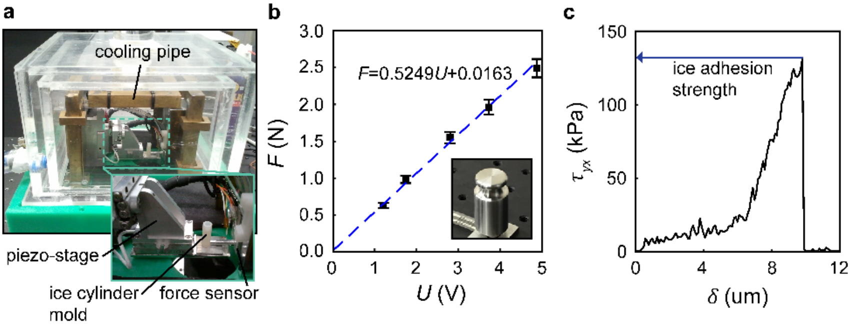

Figure A.6 Ice adhesion setup, calibration and measurements under visible light illumination ($P \approx 2.4$ kW m^{-2}). (a) Photo of the experimental ice adhesion chamber, with zoom in on the piezo-stage/sample holder. **(b)** Calibration curve of the force sensor in the highest sensitivity mode: force, F, as a function of voltage, U, using a series of test weights. The least-squares-fit is represented by the dashed line. **(c)** Representative ice adhesion curve; shear stress, τ_{yx}, *vs* displacement, δ, of an illuminated PVDF-coated control surface on fused silica substrate, at $T = -4$ °C and a constant displacement rate of $V = 10$ µm s^{-1}.

De-icing analysis. While the melt layer between the ice block and substrate is formed due to light-induced heating, it is important to understand the contributions to the measured stress, τ_{yx}. The stresses resisting the ice block movement are due to ice–substrate adhesion, liquid viscosity, and capillarity; the question is which one dominates. The stress due to viscosity can be estimated as $\approx \mu V / h_\mathrm{c}$, where μ is the viscosity of water, V is the velocity of the ice block, and h_c is the height of the melt layer. For the case of $\overline{\mathcal{A}} = 37\%$ ($\overline{\mathcal{T}} = 36\,\%$), we can estimate V with the displacement of the ice block, δ (≈ 260 µm), and mean t_d of 264 s, as $V \approx \delta / t_\mathrm{d}$. For $\tau_\mathrm{yx} = 2.5$ kPa, $V \approx 1$ µm s^{-1}, we estimate that $h_\mathrm{c} \approx \mu V / \tau_\mathrm{yx} =$ (0.001 Pa s)(10^{-6} m s^{-1})/(2500 Pa) = 0.4 µm. We can see if this height is reasonable by solving the one phase Stefan problem, $h_\mathrm{c}(t) \approx \left[P\overline{\mathcal{A}} / (\rho_\mathrm{s} H_\mathrm{f}) \right] t$. For simplification, we neglected the effect of conduction to the substrate and radiation losses within the scope of this order of magnitude analysis. The pre-factor, $P\overline{\mathcal{A}} / \rho_\mathrm{s} H_\mathrm{f}$, where H_f is the heat of fusion of water and ρ_s the ice density, is the liquid–solid phase boundary velocity. Substituting appropriate values yields 2.9 µm s^{-1}, so within ≈ 1 s, the melt layer has grown sufficiently thick to negate the importance of viscous forces in resisting ice block displacement ($P \approx 2.4$ kW m^{-2}, $\overline{\mathcal{A}} = 0.37$, $\rho_\mathrm{s} = 917$ kg m^{-3}, $H_\mathrm{f} = 334$ kJ kg^{-1}).[97] We can now estimate the stress due to capillarity: $p_\gamma \approx \sigma / R =$ (0.072 N m^{-1})/(1.5 mm) = 48 Pa, where σ is the surface tension of water. The value of p_γ is well-below the minimum value that can be measured with our setup. So, in order to explain why the mean t_d is equal to 264 s, it is clear that the melt layer must not be uniform, but rather, it grows radially with time.

Frosting characterization. Next, we investigate the anti-frosting potential of the plasmonic surfaces proposed here under sun-like illumination, in open-air environmental conditions. We consider the worst-case scenario in which the sample is in direct contact with a cold, thermally conductive surface, thus resistance to heat transfer is minimized, giving the lowest possible $\Delta T \approx 0.3$ °C (here the substrate material was fused silica, $l = 500$ µm).

Figure A.7 shows a schematic of the setup used to characterize the frosting behavior of the control and metasurface upon solar-like illumination. We used a xenon lamp, which has a sepctrum that resembled the one from the sun. The power density was also similar to that of the sun (≈ 1 kW m^{-2}). To perform the experiment, the sample (either PVDF-coated metasurface or PVDF-coated control) was first mounted on a thermoelectric cooling stage. Surface temperature was measured with an RTD temperature sensor that was mounted on a PVDF-coated control sample, which was in turn mounted on the cooling stage at a distance of ≈ 2 cm from the tested sample. By doing this, a comparative study of the metasurface *vs* control was enabled, since the impact of the heating effect of the metasurface on the temperature reading was minimized. Regions of the sample that were not illuminated were covered with an insulating teflon mask to prevent ice nucleation in those colder regions. The mask was perforated in the illuminated area.

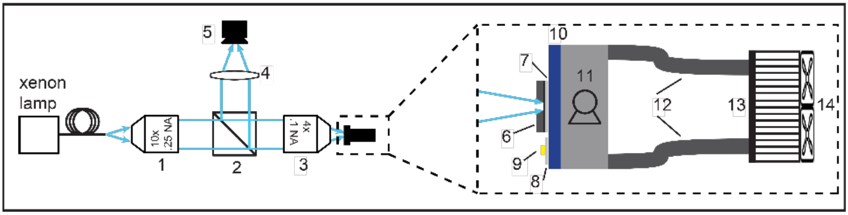

Figure A.7 Schematic of the anti-frosting setup under sun-like illumination. 1, 10x objective; 2, beam splitter; 3, 4x objective; 4, focusing lens; 5, CMOS camera; 6, thermal insulation, perforated at the illuminated area; 7, sample; 8, reference sample used for temperature measurements; 9, RTD temperature sensor; 10, thermoelectric cooling plate; 11, block with integrated pump; 12, tubing filled with coolant, hermetically sealed; 13, radiator; 14, heat dissipation by forced convection. The power density of light was $P \approx 1$ kW m^{-2}.

Figure A.8a–b shows a representative image sequence of a frosting experiment on a (a) control and (b) metasurface ($\overline{\mathcal{A}} = 83\%$, $L = 270$ nm) samples. In the case of the metasurface, the dry sample (in ambient T) was cooled down to $T = -15$ °C within ≈ 3.5 min; the surrounding environment was at 23 °C and relative humidity (ambient conditions) was in the range of $50 - 58\%$. Simultaneously, the sample was illuminated with the xenon light source (diameter of the focused beam: $D \approx 3$ mm). The temperature was then kept constant throughout the whole experiment. Water condensation started and smaller droplets coalesced ($t = 200$ s). At $t = 1000$ s, the surface remained ice-free. Finally, at $t = 1600$ s, a spontaneous event caused frost formation and propagation (dark droplet tips *vs* reflective in the liquid state before). In contrast, the control sample exhibits a vastly different behavior; it froze at a much earlier time, $t = 480$ s. There is a significant difference both in the condensation rate (water surface coverage is higher in the control), and in the freezing delay time (time from $t = 0$ to the frozen state).

Figure A.8c shows boxplot graphs of the time to freezing for the metasurface (t_{f}) and control ($t_{\mathrm{f,0}}$) samples, corresponding to mean values of $t_{\mathrm{f}} = 1937 \pm 891$ s and

$t_{f,0} = 538 \pm 289$ s respectively. The presence of the metasurface granted a $t_f / t_{f,0} \approx 3.6$ times better anti-frosting performance in terms of freezing delay time.

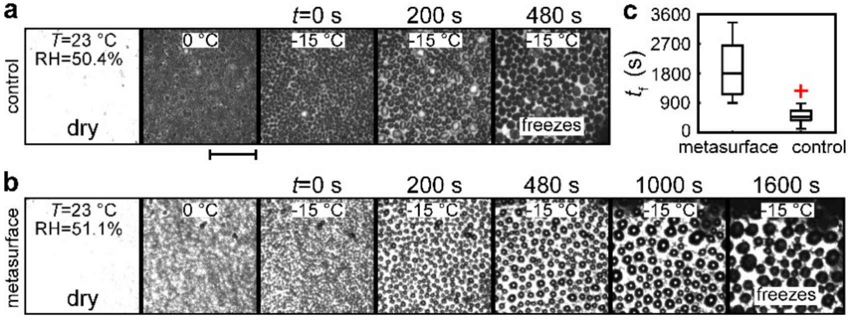

Figure A.8 Anti-frosting under sun-like illumination and ambient humidity conditions. Image sequences of: **(a)** PVDF-coated control and **(b)** PVDF-coated metasurface ($\overline{\mathcal{A}} = 83\%$), on fused silica substrates. Left to right: Illumination (xenon lamp, $P \approx 1$ kW m^{-2}) was switched on; cooldown of the sample from room temperature to $T = -15$ °C at an average rate of 10 °C min^{-1}; at $t = 0$, the temperature set point was achieved; at $t = 480$ s, the condensing water droplets on the control sample coalesced spontaneous freezing occurred; the metasurface remained ice-free for a prolonged period of time, until spontaneous freezing ($t = 1600$ s). **(c)** Boxplots of freezing time, t_f, for the metasurface and control samples. Scale bar: **(a)–(b)** 1 mm.

APPENDIX B

Initiated chemical vapor deposition (iCVD) is a novel and solvent-free deposition technique for coating surfaces with low surface energy polymeric thin films in which the pendant chemical species are kept intact. This all-dry technique has the important advantage (over standard CVD methods) of coating substrates in a very conformal manner, following the geometrical features of the substrate.[58] iCVD is our critical asset in rendering smooth surfaces hydrophobic in Chapter 4 and making superhydrophobic surfaces in Chapter 5, applied on a variety of substrates, glass, polymer or metasurface, having a smooth geometry or rationally engineered microfeatures.

iCVD has been used to deposit a plethora of vinyl monomers, with a peroxide as the initiator. The proposed mechanism is free radical polymerization of vinyl monomers. The monomer and the initiator are evaporated and simultaneously fed to the reaction chamber, where they are forced to go through an array of resistively heated wires. The heat from the wires decomposes the initiator into free radicals, which then adsorb onto the substrate. The monomer molecules are in turn adsorbed and free radical polymerization occurs on the surface to create a very thin polymer film.[58]

Figure B.1 shows a simplified instrumentation diagram of our laboratory equipment, the *iLab™* coating system, manufactured by GVD Corporation. A set of small containers are used to store the initiator and monomer in liquid form. During the process, a vacuum pump is used to control process pressure by keeping it down to low values. An external heat exchanger and a circulating water loop control the substrate temperature. The flow rates of the initiator and monomer are regulated by precise mass flow controllers (MFC), while a plethora of temperature (TC) and pressure PID controllers keep all process parameters near the set values. There is also the possibility of live indirect thickness measurement of the deposited polymer with an interferometric setup, however this is limited to reflective substrates. In our cases, we have optically transparent substrates with relatively low reflectivity, thus we cannot rely on this technique.

In order to ensure chemical connection between the substrate and the deposited polymer, there is one important step that precedes iCVD: pre-treatment of the substrate with a silane. More specifically, we used trichlorovinyl silane (TCVS) as our coupling agent. The surface vinyl groups of TCVS, which are covalently tethered, react with

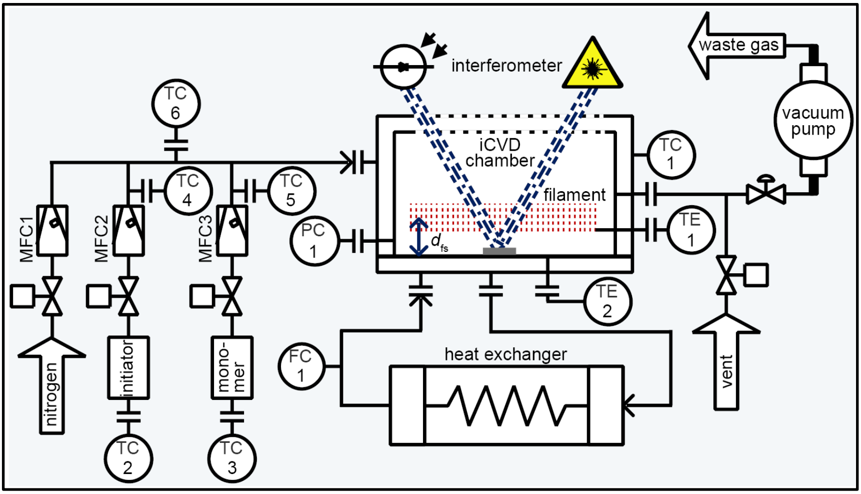

Figure B.1 Instrumentation diagram of the *iLab™* coating system. The iCVD reaction chamber walls and floor are temperature controlled. A series of temperature, pressure and mass flow controllers regulate the process parameters.

the monomer that we will use in the next step, forming strong covalent chemical bonds.[132] To find the optimum deposition conditions for TCVS, we ran a set of room temperature depositions in a separate, in-house designed, inert chamber made of glass, for different amounts of time, t_{e}, ranging from 5 to 40 min, using – at this first stage – plasma-ashed silicon substrates. We set the process pressure at ≈ 100 mTorr. After deposition, we measured the advancing contact angle, θ_{a}, receding contact angle, θ_{r} and contact angle hysteresis, $\theta_{\mathrm{a}} - \theta_{\mathrm{r}}$, for all samples. We observed that for $t_{\mathrm{e}} = 5$ min, θ_{a} and θ_{r} are much lower compared to all other depositions, while $\theta_{\mathrm{a}} - \theta_{\mathrm{r}}$ is also significant. Considering that contact angle hysteresis gives information not only on the chemical composition of a surface but also on its morphology, one could say that it is a quick measure of the quality of a surface. Therefore, we used a simple criterion for choosing the optimum conditions. This was minimum $\theta_{\mathrm{a}} - \theta_{\mathrm{r}}$. This is the case for $t_{\mathrm{e}} = 20$ min, which is the condition used throughout this thesis. We then ran further tests on the samples made at the optimum deposition condition, by testing their chemical stability. We immersed surfaces fabricated separately in acetone and subsequently in hexane, for 5 min each. We observed that even though both θ_{a} and θ_{r} increased upon immersion in acetone, the hysteresis after the second chemical treatment remained practically the same compared to as-deposited samples, proving the stability of the TCVS monolayer coating.

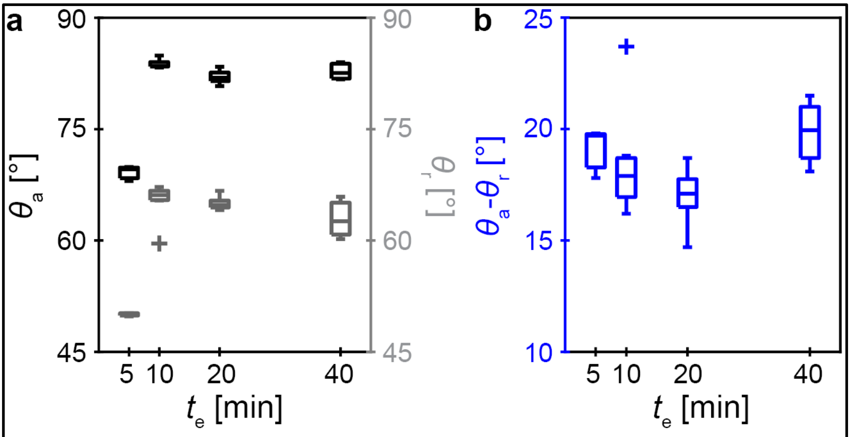

t_d [min]	θ_a [°]	θ_r [°]
5	69.2 ± 1.0	50.1 ± 0.2
10	83.8 ± 0.6	65.3 ± 2.6
20	82.0 ± 0.9	65.0 ± 0.9
40	82.7 ± 1.1	62.9 ± 2.5

t_d [min]	θ_a - θ_r [°]
5	20.0 ± 1.1
10	18.5 ± 2.5
20	17.0 ± 1.3
40	19.9 ± 1.4

Figure B.2 Wettability of substrates treated with trichlorovinyl silane. (a) Advancing, θ_a, and receding, θ_r, contact angles *vs* deposition time, t_e, of TCVS-treated silicon substrates. **(b)** Calculated contact angle hysteresis, $\theta_a - \theta_r$, of the TCVS-treated samples. The contact angle ranges shown in the boxplots are also tabulated below each plot. The number of measurements was $N \geq 6$ in all cases.

Figure B.2 shows the advancing, θ_a, and receding, θ_r, contact angles, and contact angle hysteresis, $\theta_a - \theta_r$, of the silicon substrates coated with TCVS for various amounts of time. Figure B.3 shows the same contact angles for the sample deposited at the optimum condition of $t_e = 20$ min, as well as the contact angles after immersion in acetone and hexane.

In the next step, we proceeded with optimizing the iCVD deposition process itself, conducting an exhaustive parametric study. We selected 1H,1H,2H,2H-perfluorodecyl acrylate (PFDA) as the monomer, due to its extremely low surface energy, and *t*-butyl peroxide (TBPO) as the initiator, in line with previous research on this material system.[58] The process begins by taking a TCVS-treated substrate and setting it onto the floor of the iCVD chamber. Then, after some pre-heating steps and purging with nitrogen to remove any water traces from the chamber volume and its walls, the process is run for 15 min (this time was fixed throughout the optimization) and ends with a post-purging with nitrogen step.

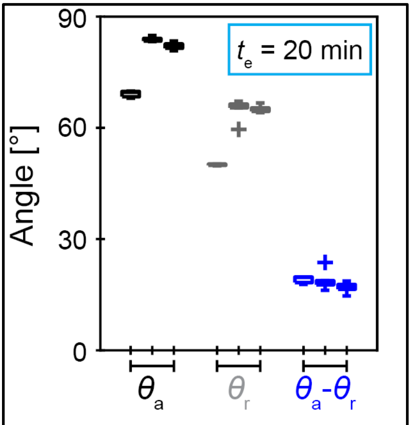

treatment	θ_a [°]	θ_r [°]	θ_a - θ_r [°]
1*	69.2 ± 1.0	50.1 ± 0.2	19.1 ± 1.1
2*	83.8 ± 0.6	65.0 ± 2.7	18.8 ± 2.6
3*	82.0 ± 0.9	65.0 ± 0.9	17.0 ± 1.3

* 1: as-prepared, 2: acetone (5 min), 3: +hexane (5 min)

Figure B.3 Wettability of substrates treated with the optimum trichlorovinyl silane deposition protocol and chemical stability tests. Advancing, θ_a, and receding, θ_r, contact angles, and contact angle hysteresis, $\theta_a - \theta_r$, for as-deposited (left increment), acetone-treated (middle increment) and acetone+hexane-treated (right increment) TCVS-treated silicon substrates. The contact angle ranges shown in the boxplots are also tabulated. The number of measurements was $N \geq 6$ in all cases.

Table B.1 shows all deposition and process parameters. It has to be noted that this optimization was based on varying the hot wire (filament) temperature, T_f, ranging from 240 °C to 300 °C, the substrate (sample) temperature, T_s, ranging from 20 °C to 60 °C, and also the distance between the filament and the sample, d_{fs}, ranging from 1 cm to 3 cm. In fact, these three parameters can change the outcome of the deposition dramatically, strongly affecting deposition rates or the number of nucleation sites on the substrate.

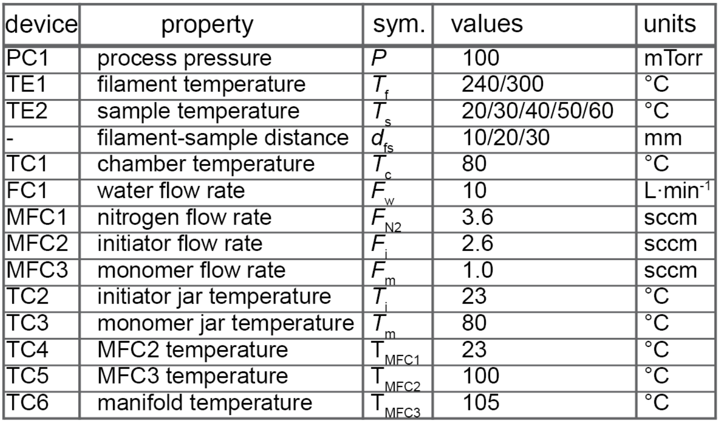

device	property	sym.	values	units
PC1	process pressure	P	100	mTorr
TE1	filament temperature	T_f	240/300	°C
TE2	sample temperature	T_s	20/30/40/50/60	°C
-	filament-sample distance	d_fs	10/20/30	mm
TC1	chamber temperature	T_c	80	°C
FC1	water flow rate	F_w	10	$\mathrm{L \cdot min^{-1}}$
MFC1	nitrogen flow rate	F_N2	3.6	sccm
MFC2	initiator flow rate	F_i	2.6	sccm
MFC3	monomer flow rate	F_m	1.0	sccm
TC2	initiator jar temperature	T_i	23	°C
TC3	monomer jar temperature	T_m	80	°C
TC4	MFC2 temperature	$\mathrm{T_{MFC1}}$	23	°C
TC5	MFC3 temperature	$\mathrm{T_{MFC2}}$	100	°C
TC6	manifold temperature	$\mathrm{T_{MFC3}}$	105	°C

Table B.1 Process parameters for the parametric study of the iCVD deposition of perfluorodecyl acrylate. All values of the process parameters used in the parametric study, and the corresponding units of the quantities, are reported here.

We then characterized the quality of the fabricated samples, as previously, by means of contact angle measurements. In this case, we used the tilting method to acquire slightly more reliable contact angle data. Figure B.4 shows the advancing contact angle, receding contact angle and contact angle hysteresis for all iCVD depositions run in the spirit of the parametric study. We observe many different values of θ_a, θ_r and $\theta_\mathrm{a} - \theta_\mathrm{r}$, however there are some general (not necessarily monotonous) trends. First of all, at both filament temperatures, T_f, tested, 240 °C and 300 °C, a low substrate temperature, T_s, results in unstable contact angles, expressed either by high $\theta_\mathrm{a} - \theta_\mathrm{r}$ or – suddenly – falling into the superhydrophobic regime. The effect of T_s is generally much more pronounced compared to the filament temperature, and this is to be expected since condensation nucleation rates are strongly dependent on temperature, as we have already seen in the theoretical part of the thesis, while T_f does not play such a significant role once it is high enough to ensure breakdown of the reactants. A similar behaviour is observed at high $T_\mathrm{s} = 50 - 60$ °C, at which contact angles become unstable, expressed in the high values of $\theta_\mathrm{a} - \theta_\mathrm{r}$. This is due to the very low deposition rates, meaning that one would expect isolated islands of polymer at high temperatures, not providing enough surface coverage to have a homogeneously hydrophobic surface. The optimum T_f is at 40 °C, where contact angles are stable, with $\theta_\mathrm{a} \approx 120°$, the maximum one can achieve on smooth hydrophobic surfaces, and $\theta_\mathrm{a} - \theta_\mathrm{r} \approx 10°$. Finally, the highest filament temperature provides generally more stable contact angles, so it is the preferred temperature for the experiments in this thesis.

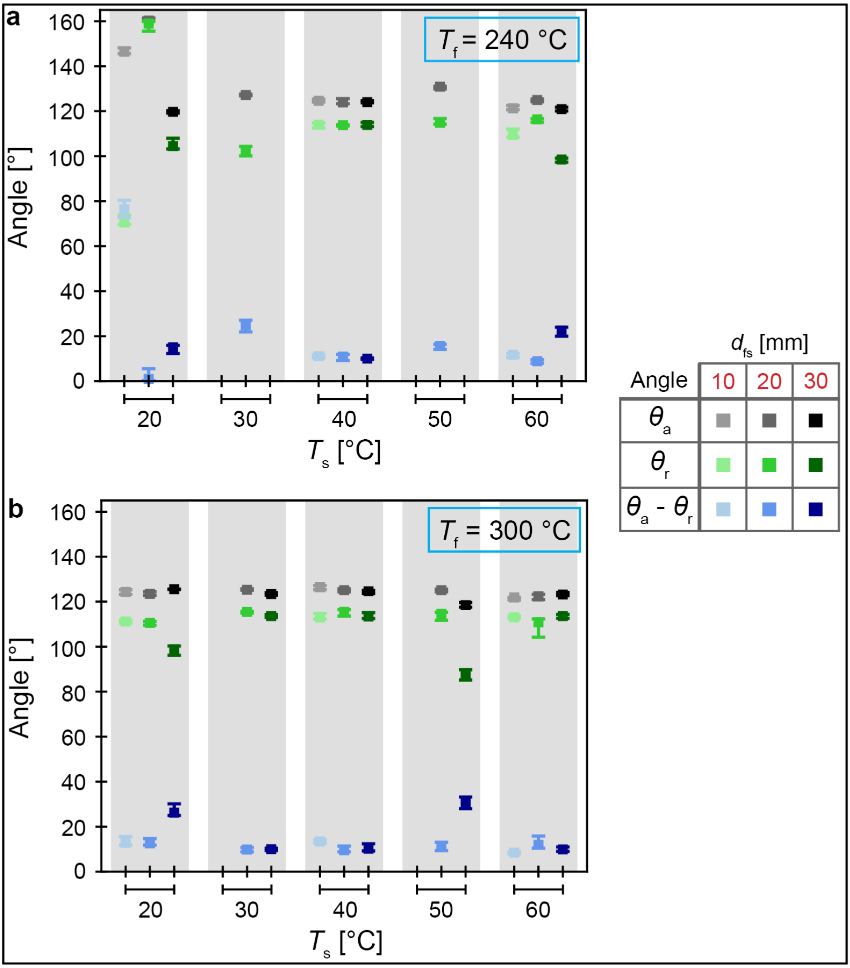

Figure B.4 Post-treatment wettability of substrates used in the parametric study of the iCVD deposition of perfluorodecyl acrylate. Advancing, θ_a, and receding, θ_r, contact angles, and contact angle hysteresis, $\theta_a - \theta_r$, as a function of substrate temperature, T_s, and filament–substrate distance, d_{fs}, for as-deposited iCVD-treated silicon substrates, for depositions at **(a)** $T_f = 240$ °C and **(b)** $T_f = 300$ °C. The number of measurements was $N \geq 5$ in all cases.

All contact angle values related to the parametric study of iCVD are summarized in Table B.2, where the corresponding values after hexane treatment of each iCVD-treated sample for 5 min are also reported.

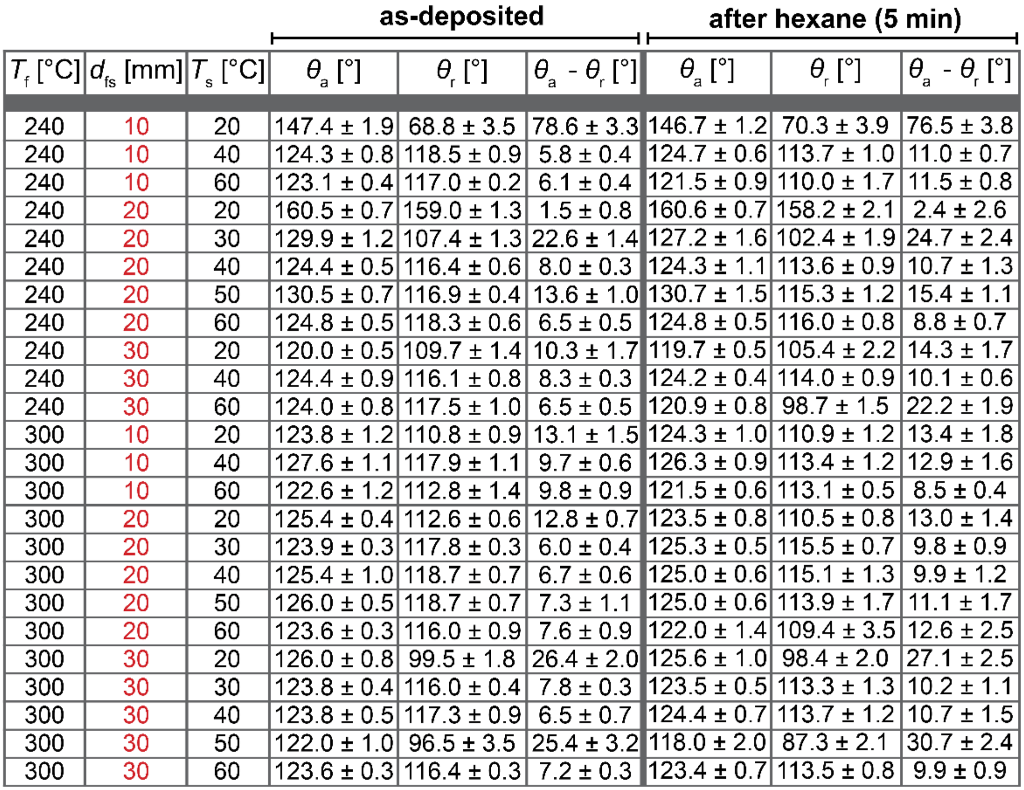

			as-deposited			after hexane (5 min)		
T_f [°C]	d_{fs} [mm]	T_s [°C]	θ_a [°]	θ_r [°]	$\theta_a - \theta_r$ [°]	θ_a [°]	θ_r [°]	$\theta_a - \theta_r$ [°]
240	10	20	147.4 ± 1.9	68.8 ± 3.5	78.6 ± 3.3	146.7 ± 1.2	70.3 ± 3.9	76.5 ± 3.8
240	10	40	124.3 ± 0.8	118.5 ± 0.9	5.8 ± 0.4	124.7 ± 0.6	113.7 ± 1.0	11.0 ± 0.7
240	10	60	123.1 ± 0.4	117.0 ± 0.2	6.1 ± 0.4	121.5 ± 0.9	110.0 ± 1.7	11.5 ± 0.8
240	20	20	160.5 ± 0.7	159.0 ± 1.3	1.5 ± 0.8	160.6 ± 0.7	158.2 ± 2.1	2.4 ± 2.6
240	20	30	129.9 ± 1.2	107.4 ± 1.3	22.6 ± 1.4	127.2 ± 1.6	102.4 ± 1.9	24.7 ± 2.4
240	20	40	124.4 ± 0.5	116.4 ± 0.6	8.0 ± 0.3	124.3 ± 1.1	113.6 ± 0.9	10.7 ± 1.3
240	20	50	130.5 ± 0.7	116.9 ± 0.4	13.6 ± 1.0	130.7 ± 1.5	115.3 ± 1.2	15.4 ± 1.1
240	20	60	124.8 ± 0.5	118.3 ± 0.6	6.5 ± 0.5	124.8 ± 0.5	116.0 ± 0.8	8.8 ± 0.7
240	30	20	120.0 ± 0.5	109.7 ± 1.4	10.3 ± 1.7	119.7 ± 0.5	105.4 ± 2.2	14.3 ± 1.7
240	30	40	124.4 ± 0.9	116.1 ± 0.8	8.3 ± 0.3	124.2 ± 0.4	114.0 ± 0.9	10.1 ± 0.6
240	30	60	124.0 ± 0.8	117.5 ± 1.0	6.5 ± 0.5	120.9 ± 0.8	98.7 ± 1.5	22.2 ± 1.9
300	10	20	123.8 ± 1.2	110.8 ± 0.9	13.1 ± 1.5	124.3 ± 1.0	110.9 ± 1.2	13.4 ± 1.8
300	10	40	127.6 ± 1.1	117.9 ± 1.1	9.7 ± 0.6	126.3 ± 0.9	113.4 ± 1.2	12.9 ± 1.6
300	10	60	122.6 ± 1.2	112.8 ± 1.4	9.8 ± 0.9	121.5 ± 0.6	113.1 ± 0.5	8.5 ± 0.4
300	20	20	125.4 ± 0.4	112.6 ± 0.6	12.8 ± 0.7	123.5 ± 0.8	110.5 ± 0.8	13.0 ± 1.4
300	20	30	123.9 ± 0.3	117.8 ± 0.3	6.0 ± 0.4	125.3 ± 0.5	115.5 ± 0.7	9.8 ± 0.9
300	20	40	125.4 ± 1.0	118.7 ± 0.7	6.7 ± 0.6	125.0 ± 0.6	115.1 ± 1.3	9.9 ± 1.2
300	20	50	126.0 ± 0.5	118.7 ± 0.7	7.3 ± 1.1	125.0 ± 0.6	113.9 ± 1.7	11.1 ± 1.7
300	20	60	123.6 ± 0.3	116.0 ± 0.9	7.6 ± 0.9	122.0 ± 1.4	109.4 ± 3.5	12.6 ± 2.5
300	30	20	126.0 ± 0.8	99.5 ± 1.8	26.4 ± 2.0	125.6 ± 1.0	98.4 ± 2.0	27.1 ± 2.5
300	30	30	123.8 ± 0.4	116.0 ± 0.4	7.8 ± 0.3	123.5 ± 0.5	113.3 ± 1.3	10.2 ± 1.1
300	30	40	123.8 ± 0.5	117.3 ± 0.9	6.5 ± 0.7	124.4 ± 0.7	113.7 ± 1.2	10.7 ± 1.5
300	30	50	122.0 ± 1.0	96.5 ± 3.5	25.4 ± 3.2	118.0 ± 2.0	87.3 ± 2.1	30.7 ± 2.4
300	30	60	123.6 ± 0.3	116.4 ± 0.3	7.2 ± 0.3	123.4 ± 0.7	113.5 ± 0.8	9.9 ± 0.9

Table B.2 Post-treatment wettability of substrates used in the parametric study of the iCVD deposition of perfluorodecyl acrylate. Tabulated values of advancing, θ_a, and receding, θ_r, contact angles, and contact angle hysteresis, $\theta_a - \theta_r$, for as-deposited samples and after hexane immersion of iCVD-treated silicon substrates.

In the previous paragraphs, we suggested that the extent of condensation nucleation is different depending on the temperature, which naturally leads to the need of imaging the majority of actual coatings. This is done with an optical microscope in DIC mode, with a high magnification 100x objective. Figure B.5 shows optical microscopy images of samples deposited while $T_f = 240$ °C, and Figure B.6 shows images of samples deposited while $T_f = 300$ °C.

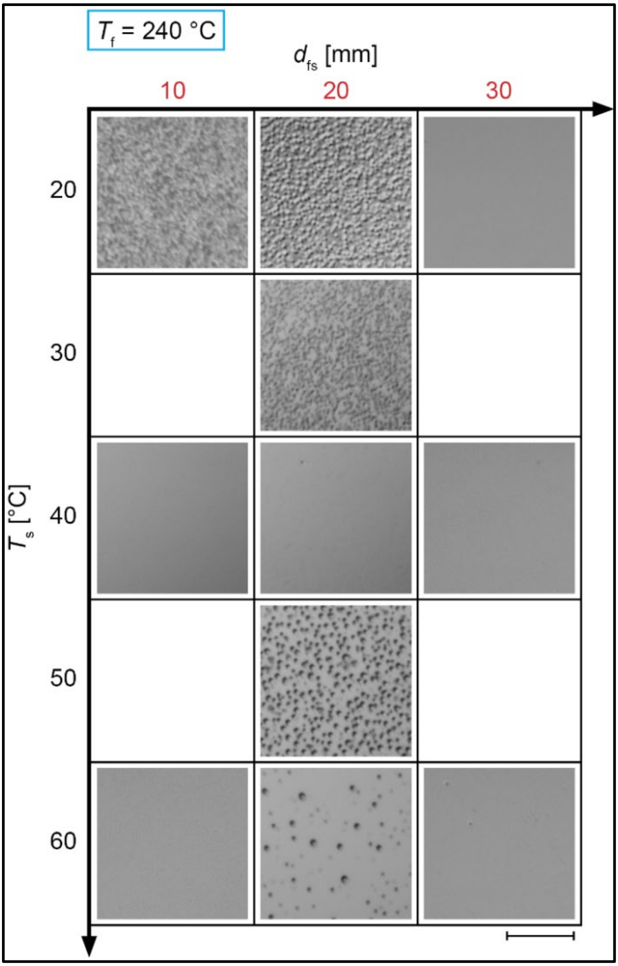

Figure B.5 Optical microscopy images of substrates used in the parametric study of the iCVD deposition of perfluorodecyl acrylate. Filament temperature, T_f, was 240 °C. Scale bar: 10 µm.

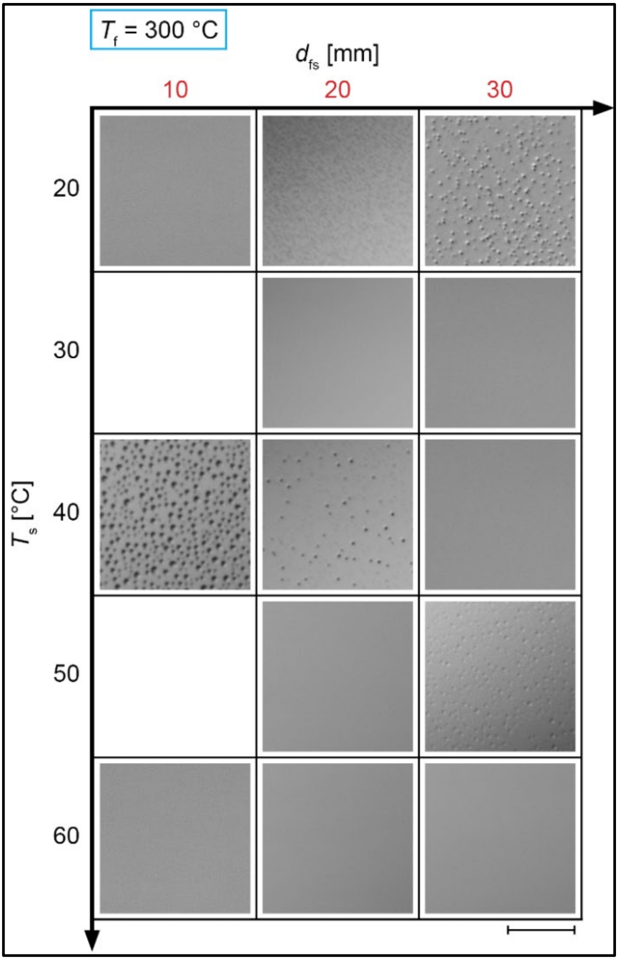

Figure B.6 Optical microscopy images of substrates used in the parametric study of the iCVD deposition of perfluorodecyl acrylate. Filament temperature, T_f, was 300 °C. Scale bar: 10 µm.

Based on the optical microscopy images, we have a less clear trend in the quality of the depositions as a function of the parameters we varied. However, a few claims can be made. Firstly, low substrate temperatures, T_s, generally leave a lot of material behind, in the form of a dense array of randomly nucleated polymer islands. At higher T_s, these islands are not that dense anymore or have completely disappeared. Second, filament temperature, T_f, does have a – different – effect on the appearance of postdeposited surfaces. The highest T_f exhibits fewer cases with dense or large islands. This could be either due to less material getting deposited or improved homogeneity. Based on the contact angle measurements, we can attribute the observed behavior mainly to the second factor. When T_f is high, reactants can break down to small species. The small free radicals coming from the initiator molecules can then be attached to the substrate in a more homogeneous and conformal way compared to the case of fewer radicals and lots of unbroken molecules. Finally, something that was not discussed up to this point is the effect of filament–substrate distance on the outcome of the depositions. It is clear that at the largest d_fs one observes few or no islands on the samples. Although the reason for this behavior was not studied extensively, it is clear from the high contact angle hysteresis that this is not the optimum distance.

APPENDIX C

Advancing and receding water contact angles of the tested surfaces. Both the advancing (θ_a) and receding (θ_r) contact angles for each of the tested surfaces used in this study are an integral part that we use to explain the phenomena that we observed. We measured and summarized both θ_a and θ_r in Figure C.1 for all of the surfaces used in this study, using 3 different samples of each kind and 2–3 measurements for each sample, for a total of 7 measurements ($n = 7$). Figure C.1a–b show the spread across the measurements for each sample type using box and whisker plots. For our study it is important that θ_a and θ_r are comparable between the same sample types of control and metasurface (i.e. the silane-treated control and metasurface must have similar contact angles). This is important in order to rule out any sort of effect on anti-fogging or de-fogging that is not due to the sunlight absorbing properties of the metasurfaces.

Inspecting Figure C.1, one observes that, in spite of the fact that surface chemistry is expected to be identical between metasurfaces and control samples of the same type, θ_a is slightly larger and θ_r is slightly smaller for the metasurfaces. This increase in the contact angle hysteresis is a typical signature for increased surface roughness, assuming that the droplets sit in the Wenzel state.

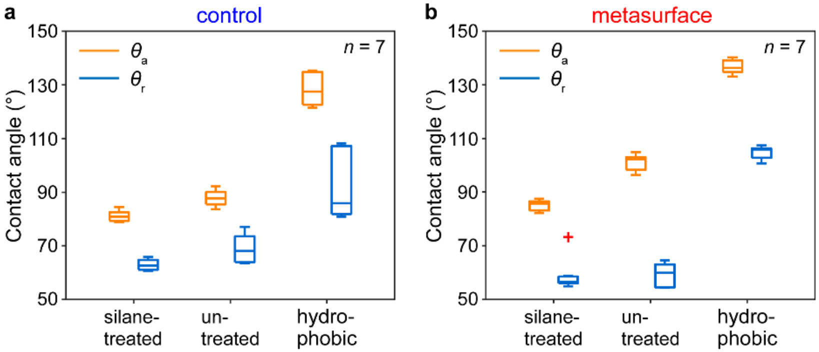

c

control	θ_a	θ_r
silane-treated	81.1 ± 2.0°	63.0 ± 2.0°
untreated	87.8 ± 3.0°	68.7 ± 5.5°
hydrophobic	128.5 ± 6.2°	93.3 ± 13.3°

d

metasurface	θ_a	θ_r
silane-treated	85.1 ± 2.0°	59.0 ± 6.4°
untreated	101.2 ± 3.2°	55.6 ± 11.6°
hydrophobic	136.6 ± 2.7°	104.6 ± 2.4°

Figure C.1 Advancing and receding contact angles of the control samples and metasurfaces used in this study. (a–b) Advancing, θ_a, and receding, θ_r, contact angles of the following samples types: treated with trichlorovinylsilane (silane-treated), untreated and treated with poly(perfluorodecyl acrylate) (hydrophobic), for **(a)** control and **(b)** metasurfaces. **(c–d)** The advancing and receding contact angles shown above tabulated, for **(c)** control and **(d)** metasurfaces.

Theoretical effect of surface wettability on fogging resistance. Using classical nucleation theory one can derive the supersaturation (p/p_L) at which heterogeneous nucleation of liquid water from water vapor should theoretically occur on a surface. This is important for anti-fogging applications as it provides design rules in order to engineer superior fog-resistant materials. We begin the derivation by defining the critical free energy necessary to overcome in order to form a nascent water embryo in the absence of any surface (ΔG^* , homogeneous nucleation) as:

$$\Delta G^* = 16\pi\gamma^3 \Big/ \left(3\left[n_L kT \ln\left(p/p_L\right)\right]^2\right) \tag{C.1}$$

where γ is the surface tension of water in air, n_L is the number of water molecules per unit volume, k is Boltzmann's constant, at temperature T and supersaturation p/p_L , where p is the water vapor pressure of the environment and p_L is the saturated vapor pressure over a plane surface of water. Because of the inverse squared relationship of p/p_L to the natural logarithm, a larger p/p_L results in a significantly lower ΔG^* .

The critical free energy for nucleation on a surface is a modification of this equation by a factor (f), which is a function of the water contact angle on the surface (θ), assuming the surface is flat, given by:[66]

$$\Delta G^{*} = 16\pi\gamma^{3} \Big/ \left(3\left[n_{\mathrm{L}} kT \ln\left(p/p_{\mathrm{L}}\right)\right]^{2}\right) f(\theta)$$

(C.2)

The function $f\left(\theta\right)$ can be expressed as:[66]

$$f\left(\theta\right) = 1/4\left(2 - \cos\theta + \cos^{3}\theta\right)$$

(C.3)

where 0 < $f\left(\theta\right)$ < 1; a larger θ results in larger $f\left(\theta\right)$. This also means that a larger θ results in a higher ΔG^{*}. The final equation that gives us the nucleation rate (J), which allows us to predict the probability of a nucleation event is given by:

$$J = J_{0} \exp\left(-\Delta G^{*}/kT\right)$$

(C.4)

where J_{0} is a rate constant determined by the rate at which vapor molecules strike a unit area of the embryo. Here, it is important to observe that J has an inversely exponential relationship to ΔG^{*} and therefore will grow exponentially larger as ΔG^{*} becomes smaller.

Using equations (C.2), (C.3) and (C.4), Figure C.2 illustrates the dependence of J on p/p_{L} and θ. We observe the exponential dependence of J on p/p_{L} for both θ. More importantly, however, we observe that the difference in θ changes J by many orders of magnitude. For example, at $p/p_{\mathrm{L}} \approx 2.25$, a surface with $\theta = 80^{\circ}$ would result in $J = 1$ $\mathrm{mm}^{-2}\ \mathrm{s}^{-1}$, while a surface with $\theta = 125^{\circ}$ at the same p/p_{L} would result in $J \approx 10^{-35}$, or for all intents and purposes no observation of nucleation. Furthermore, p/p_{L} would have to be ≈ 3.5 before a surface with $\theta = 125^{\circ}$ would result in a substantial nucleation rate $J = 1$ $\mathrm{mm}^{-2}\ \mathrm{s}^{-1}$. Differences in surface wettability have been shown to create favorable condensation nucleation on more hydrophilic areas,[35] however a quantified difference of p/p_{L} between the two surfaces was not measured. Nonetheless, this analysis indicates that one could theoretically engineer more fog-resistant surfaces by simply increasing the surface hydrophobicity in order to inhibit the formation of condensate on the surface. Of course, after the condensate has been formed, the influence of the contact angle of the microdroplets on light scattering is another aspect that must be considered, especially for large droplets or high water surface coverage.

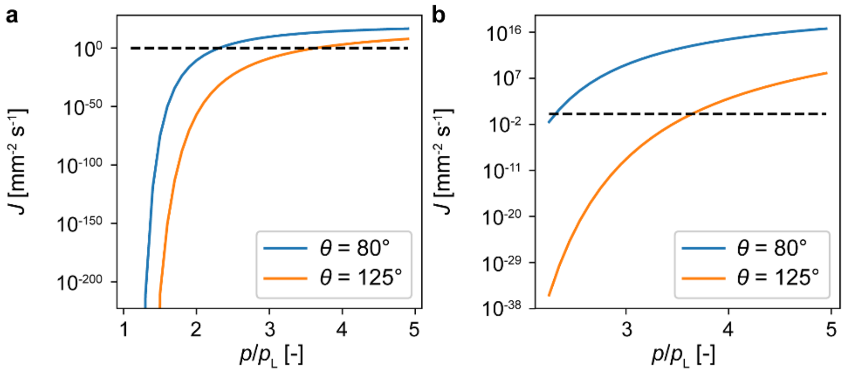

Figure C.2 Dependence of the heterogeneous nucleation rate (J) on both vapor supersaturation and water contact angle. Due to the increased surface area of higher contact angle droplets the energy barrier for heterogeneous nucleation (ΔG^*) increases with contact angle. The exponential dependence of ΔG^* on J is illustrated in **(a)**. This relationship can be better observed in **(b)**: zoomed in plot showing the range of supersaturations in which J becomes substantial, illustrating that J for a substrate with θ is >30 orders of magnitude lower, as compared to the p/p_L where $J=1$ mm^{-2} s^{-1} for a substrate with $\theta=80°$. The black dashed line corresponds to $J=1$ mm^{-2} s^{-1}.

Observed effect of surface wettability on fogging resistance. It has been shown that a biphilic surface exposed to supersaturated conditions nucleates preferentially on the hydrophilic areas. Furthermore, classical nucleation theory predicts that hydrophobic surfaces should be able to also withstand much higher supersaturation without nucleation events when compared to hydrophilic surfaces. Remarkably, we found that the hydrophobic surfaces were not able to withstand higher supersaturation than neutrally wetting surfaces, rather they simply reduced the number of nucleation sites. Figure C.3a–b show a control glass surface and a hydrophobic surface, respectively, that have been exposed to slightly supersaturated ($p/p_L \approx 1.02$) conditions for 60 s. Based upon the aforementioned plot in Figure C.2a, we would expect an extremely low J for both surfaces, however experimentally we still observe nucleation on both surfaces. This may be best explained by either contamination or surface adsorption of hydrocarbons and other environmental contaminants, both of which may render a hydrophobic surface more hydrophilic. Furthermore, surface cavities also increase the likelihood of nucleation. Since we observe more nucleation sites on the control surface than on the hydrophobic surface, it begs the question why more foreign material acting as nucleation sites would be adsorbed to the control surface. We suggest that the high surface energy of highly hydrophilic materials causes them to attract more adsorbates.[120]

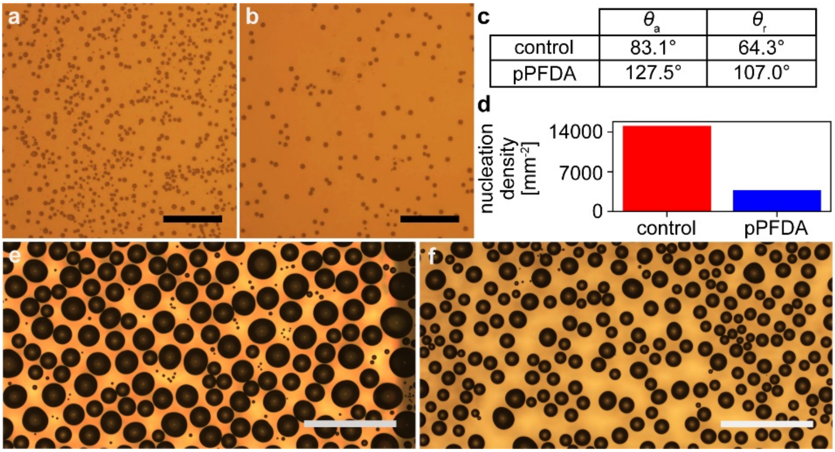

Figure C.3 Effect of the water contact angle on condensation nucleation density. We compared the nucleation density of the untreated glass (control) and the pPFDA-coated glass. Micrographs recorded 60 s after the onset of nucleation on **(a)** untreated glass and **(b)** pPFDA-coated glass show that the nucleation density is higher on the untreated glass in comparison to the pPFDA-coated glass, although nucleation is observed happening at the same supersaturation. The measured macroscopic advancing and receding contact angles of both the untreated and pPFDA-coated glass are shown in **(c)** and indicate that the pPFDA-coated surface is considerably more hydrophobic. According to classical nucleation theory, the barrier for condensation nucleation should be higher the more hydrophobic the surface is, because of higher advancing contact angle. Using computer-aided image analysis, the nucleation density on each substrate was quantified **(d)**. The nucleation density has an influence on the condensate coverage after exposure to a supersaturation of 1.3 for 10 min. The **(e)** control sample has a considerably higher amount of water on its surface, as compared to the **(f)** pPFDA-coated glass. Scale bars: **(a–b)**, 50 µm; **(e–f)**, 500 µm.

Although hydrophobic coatings may reduce the nucleation density, they do not solve the problem of retaining visibility of transparent surfaces under supersaturated conditions (refer to Figure 4.1c). Nonetheless, they reduce the total amount of condensate coverage on the surface as compared to a more hydrophilic surface. We measured the volume of water on the surface using the droplet sizes, assuming an advancing contact angle and using the spherical cap approximation, for our hydrophobic sample, and compared it to the corresponding water volume on an untreated sample. We calculated a reduction of approximately 10% in water volume for the hydrophobic surface, compared to the untreated one, after 60 s of exposure to supersaturated conditions.

Infrared thermography and temperature response measurements. Infrared thermography is a non-intrusive surface temperature measurement technique, especially useful in cases where the thermal mass of the surface in test is very low. This way, we ensure that the actual temperature of our samples upon illumination is measured, while it also enables contactless observations during the single droplet evaporation experiments shown in Figure 4.3. A simplified expression of the temporally and spatially changing signal that the infrared camera receives can be written as:

$$C_{\mathrm{t}} = \varepsilon C_{\mathrm{s}} + C_{\mathrm{base}} \tag{C.5}$$

where ε is the sample emissivity, C_{s} is the signal that the sample would emit if it was a blackbody ($\varepsilon = 1$) and C_{base} is the residue background signal.[130] Using equation (C.5 for two discrete temperatures, ambient, T_{amb} and an elevated one, T', and subtracting in parts, assuming constant background signal, we have:

$$C_{\mathrm{t}}^{T'} - C_{\mathrm{t}}^{T_{\mathrm{amb}}} = \varepsilon \left(C_{\mathrm{s}}^{T'} - C_{\mathrm{s}}^{T_{\mathrm{amb}}} \right) \tag{C.6}$$

We calibrated the infrared camera independently for the metasurface, control, and tinted laminate by using a hot plate and covering a temperature range of approximately 20 °C above the ambient. This way, ε could be estimated ($\varepsilon \approx 0.9$ for the control and metasurface), and signal was converted into temperature by using the internal calibration curve of the camera, $C_{\mathrm{s}}^{T'} = f(T)$. In the IR images shown in Figure 4.3d–e, a standard emissivity of $\varepsilon = 1$ was assumed specifically for the water droplets.

Figure C.4a shows temperature increase *vs* time for a 500 µm untreated control and an untreated metasurface due to illumination, using a visible (halogen) light source and a power density of 1 sun for the illumination. We ran 3 experiments for each sample category ($n = 3$). Figure C.4b shows the temperature response curves at an increased power density of ≈ 4 suns. Here we must mention that those temperatures were acquired by drawing a square box which covered $> 75\%$ of the total sample area (5 mm x 5 mm) and taking the average temperature of the square for each time moment. The maximum temperature increase (180 s after the light was switched on) was 0.2 °C and 0.3 °C for the bare control, and 3.8 °C and 15.4 °C for the bare metasurface, at a power density of 1 sun and 4 suns, respectively.

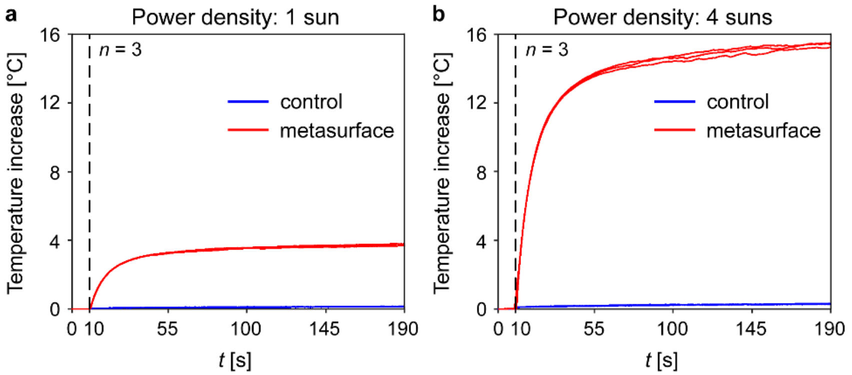

Figure C.4 Infrared-measured temperature response of water droplet-free untreated control (glass) samples and our metasurfaces, upon sun-like illumination. (a) Temperature increase with respect to ambient *vs* t for a control and metasurface, at a power density of 1 sun (1000 W m^{-2}). **(b)** The same quantities, at a power density of 4 suns. Sample size was 5 mm by 5 mm. The dashed black lines indicate the time at which illumination was switched on ($t = 10$ s). Illumination was kept on for 180 s. Ambient temperature was 23.5 ± 0.5 °C.

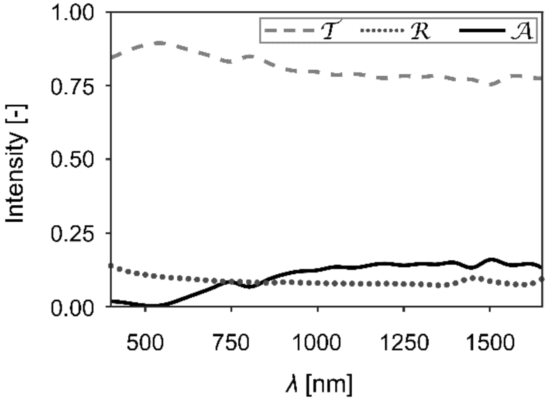

Figure C.5 Infrared Optical characterization of the control. Reflectance ($\mathcal{R}$), transmittance ($\mathcal{T}$), and absorbance ($\mathcal{A}$) spectra of the control sample for visible and near infrared wavelengths (400–1650 nm).

APPENDIX D

Topography of the control. Figure D.1 shows a scanning electron micrograph of the superhydrophobic control surface. This surface lacks a metasurface coating.

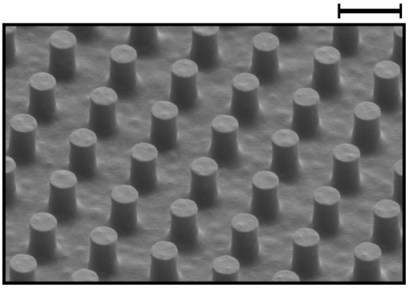

Figure D.1 Micrograph of the control surface. Scale bar: 5 µm.

Transmittance, reflectance and absorbance spectra of control surfaces. The transmittance, reflectance and absorbance spectra of our control surfaces (iCVD-coated PUA micropillars on glass) over a broad wavelength range, covering most of the solar spectrum, are shown in Figure D.2. It was found that for normal light incidence the presence of pillars does not result in a significant change in the optical properties of the glass substrate, as indicated by the mean transmittance value of 85%. Mean reflectance and absorbance are 8% and 7%, respectively.

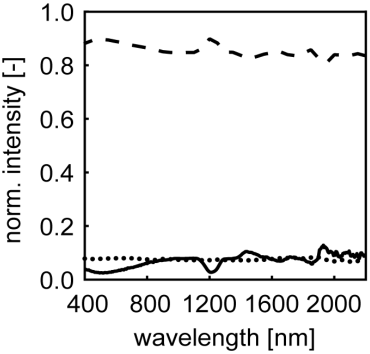

Figure D.2 Transmittance (– – –), $\mathcal{T}$, reflectance (· · ·), $\mathcal{R}$, and absorbance (——), $\mathcal{A}$, spectra of control surfaces over the 400–2200 nm wavelength range.

Room temperature droplet impact on a superhydrophobic metasurface. Figure D.3 shows an image sequence of a room temperature water droplet impacting onto a superhydrophobic metasurface. The metasurface was not illuminated.

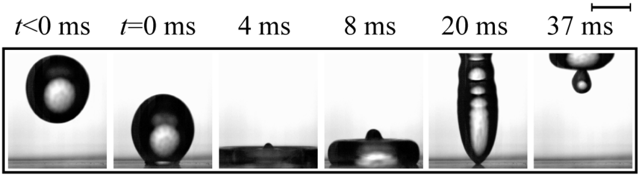

Figure D.3 Droplet impact of an ambient water droplet on a superhydrophobic metasurface. Ambient temperature was ~21 °C and We ≈ 26. Scale bar: 2 mm.

Theoretical basis of impalement criterion. In the case of pure condensation-based impalement, we need to calculate the minimum time (theoretical) required to fill a single cavity between adjacent micropillars due to water vapor diffusion from the warm droplet to the colder surface. Taking Fick's law we first calculate the maximum diffusive mass flux between the droplet ($z=h$) and the condensate within a cavity ($z=H$): $J_{\mathrm{dif}}=-\overline{D_{\mathrm{V}}}\Delta\rho_{\mathrm{V}}/\Delta z$, where D_{V} is the diffusion coefficient of water vapor in air at the mean temperature $\overline{T}=\left(T_H+T_h\right)/2$, $\Delta\rho_{\mathrm{V}}=\rho_{\mathrm{V},h}-\rho_{\mathrm{V},H}$ is the water vapor mass concentration difference, where $\rho_{\mathrm{V},h}$ and $\rho_{\mathrm{V},H}$ are the water vapor mass concentrations at $z=h$ and $z=H$, respectively, and $\Delta z=h-H$ is the distance between the water droplet and the condensate. The flow rate is maximum when the temperature of the condensate is constant and equal to the surface temperature throughout the process of filling; we also assume constant droplet temperature. In order to get the flow rate, we multiply J_{dif} by the projected surface area of the cavity, A : $\dot{m}_{\mathrm{dif}}=A\overline{D_{\mathrm{V}}}\Delta\rho_{\mathrm{V}}/\Delta z$. The cavity filling velocity is: $\dot{H}=\dot{m}_{\mathrm{dif}}/\overline{\rho_{\mathrm{L}}}$, where $\overline{\rho_{\mathrm{L}}}$ is the liquid water density at the mean temperature $\overline{T}$. Given the volume of the cavity that remains unfilled is $A\left(h-H\right)$, the filling time for a partially filled cavity can be calculated as $\tau_{\mathrm{f}}=A\left(h-H\right)/\dot{H}$, which leads us to:

$$\tau_{\mathrm{f}}=\frac{\overline{\rho_{\mathrm{L}}}h\left(h-H\right)}{-\overline{D_{\mathrm{V}}}\left(\rho_{\mathrm{V},h}-\rho_{\mathrm{V},H}\right)} \tag{D.1}$$

For a previously empty cavity ($H=0$), filling time is given by:

$$\tau_{\mathrm{f}}=\frac{\overline{\rho_{\mathrm{L}}}h^2}{-\overline{D_{\mathrm{V}}}\left(\rho_{\mathrm{V},h}-\rho_{\mathrm{V},0}\right)} \tag{D.2}$$

The only unknown in equation (D.2) is the water vapor mass concentration difference, which for simplicity we term ΔC . We can calculate the mass concentrations by assuming that the water vapor is an ideal gas, which should hold true for low water vapor concentrations. Taking into account Dalton's law, applied for the water–air mixture within the cavity at temperature T , and the ideal gas law, we acquire the relation for the total vapor pressure: $P_{\mathrm{tot}}=\left(n_{\mathrm{air}}/V_{\mathrm{air}}+n_{\mathrm{V}}/V_{\mathrm{V}}\right)RT$, where n represents number of moles, V is volume and R is the ideal gas constant. The previous equation can be rewritten upon replacing volumes with densities: $P_{\mathrm{tot}}=\left(\rho_{\mathrm{air}}/M_{\mathrm{air}}+\rho_{\mathrm{V}}/M_{\mathrm{V}}\right)RT$, where M is molecular weight. Upon rearranging, assuming that the water vapor is saturated ($P_{\mathrm{V}}=P_{\mathrm{V,sat}}$), we have:

$$\frac{P_{\text{tot}}}{P_{\text{V,sat}}} = 1 + \frac{\rho_{\text{air}}}{\rho_{\text{V,sat}}} \cdot \frac{M_{\text{V}}}{M_{\text{air}}} \tag{D.3}$$

Solving equation (D.3) for $\rho_{\text{V,sat}}$, assuming $P_{\text{air}} \approx P_0$, where P_0 is the atmospheric pressure, we get the unknown water vapor mass concentration we were looking for:

$$\rho_{\text{V,sat}} = C = \frac{M_{\text{V}}}{M_{\text{air}}} \rho_{\text{air}} \frac{P_{\text{V,sat}}}{P_0} \tag{D.4}$$

Therefore, based on equation (D.4), the aforementioned unknown water vapor mass concentration difference can be calculated as:

$$\rho_{\text{V},h} - \rho_{\text{V},0} = \Delta C = \frac{M_{\text{V}}}{M_{\text{air}} P_0} \left(\frac{P_{\text{V,sat},h}}{\rho_{\text{air},h}} - \frac{P_{\text{V,sat,0}}}{\rho_{\text{air,0}}} \right) \tag{D.5}$$

Combining equations (D.2) and (D.5) we have the complete relation for the filling time:

$$\tau_{\text{f}} = \frac{M_{\text{air}} \overline{\rho_{\text{L}}} P_0 h^2}{M_{\text{V}} \overline{D_{\text{V}}} \left(\frac{P_{\text{V,sat,0}}}{\rho_{\text{air,0}}} - \frac{P_{\text{V,sat},h}}{\rho_{\text{air},h}} \right)} \tag{D.6}$$

In order for condensation-based filling of a cavity to take place, the droplet has to be in contact with the top of the micropillars. The theoretical droplet contact time during a droplet impact event on a rigid substrate, in the case of low viscosity liquids, is equal to the inertial capillary time:[49]

$$\tau = \frac{\pi}{4} \sqrt{\frac{\rho_{\text{L},h} \left(2R_0\right)^3}{\gamma_{\text{LV},h}}} \tag{D.7}$$

where R_0 is the initial water droplet radius and $\gamma_{\text{LV},h}$ is the water surface tension at $z = h$.

One can simply realize the condensation-based impalement criterion based on the τ / τ_{f} ratio. When $\tau / \tau_{\text{f}} << 1$, the contact time is not sufficient for the cavities to fill and impalement to occur, while the opposite is true for $\tau > \tau_{\text{f}}$. Therefore, one expects the transition from no impalement to full impalement to occur at $\tau / \tau_{\text{f}} \approx 1$. A correction factor, α, in front of t_{f} might be needed depending on the droplet temperature to account for cooling of the droplet and other effects.

Effect of surface temperature on condensation nucleation on control surfaces due to warm water droplets. One of the first steps of the condensation impalement study, upon fabrication of superhydrophobic control surfaces (without a metasurface coating), was to investigate the effects of substrate temperature, T_s, and water temperature, T_w, on condensation nucleation due to sessile warm water droplets. For this purpose, we gently placed single warm droplets on the surface and recorded the outcome with our high-speed camera. Figure D.4a shows representative image sequences of warm water droplets placed on surfaces of different temperatures, T_s, ranging from ambient, $T_\mathrm{s} = T_\infty = 21$ °C, to $T_\mathrm{s} = T_\infty + 20 = 41$ °C. The droplet–surface temperature difference, $T_\mathrm{w} - T_\mathrm{s}$, was kept roughly the same, at ≈ 13 °C, in order to investigate the isolated effect of T_s on the impalement time, t_f. Figure D.4b shows plots of impalement probability, *Φ*, *vs* T_w, for the extreme cases of $T_\mathrm{s} = 21$ °C and $T_\mathrm{s} = 41$ °C, for different water temperatures, $T_\mathrm{w} \in [21, 70]$ °C. Finally, in Figure D.4c, we plot the experimental t_f *vs* the theoretically predicted filling time, τ_f, for all T_s and for the T_w which led to impalement events.

Based on Figure D.4b, one observes that the transition from no impalement to the impalement regime (high *Φ*) is smooth, spanning a T_w range of over 10 °C. More importantly, a higher T_s shifts the onset of impalement towards higher water temperatures. In fact, it seems like the $T_\mathrm{w} - T_\mathrm{s} \approx 40$ °C required for this onset remains almost the same, independent of T_s. One can design superhydrophobic surfaces with a specific $T_\mathrm{w} - T_\mathrm{s}$ target, depending on the application, and use a heat source to shift the impalement transition if needed, for example under extreme environmental conditions, with the transition temperature being – roughly – proportional to the temperature increase due to heating. Figure D.4c reveals that, as in the cases of superhydrophobic metasurfaces and heating with light, T_s has an effect on the relation between the experimental t_f and the theoretical τ_f, expressed as a linear relationship, such that $t_\mathrm{f} = \alpha \tau_\mathrm{f}$, where α is the slope of the least squares line. In fact, this proportionality constant, α, highly depends on T_s. For $T_\mathrm{s} = T_\infty$, $\alpha \approx 9$, which is similar to what was found in other works.[50] For $T_\mathrm{s} >> T_\infty$, in our control surfaces, $\alpha \approx 40$. This difference in α is statistically significant. The reasons behind the temperature dependence of α are analysed in the main text.

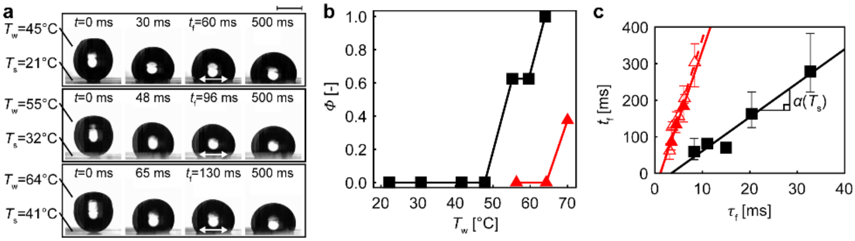

Figure D.4 Effect of surface temperature on condensation nucleation in the presence of sessile warm droplets. (a) Image sequences of warm sessile droplets on a superhydrophobic control surface in the cases of ambient surface temperature (T_s = 21 °C; top row) and medium and high surface temperatures (T_s = 32 °C and T_s = 41 °C; middle and bottom row, respectively). A hot plate was used for heating up the surfaces. **(b)** Impalement probability, *Φ*, *vs* water droplet temperature, T_w, for ambient (black squares) and high (red triangles) temperature substrates. Each data point in **b** represents $N \geq 7$ experiments. **(c)** Droplet impalement time, t_f, *vs* cavity filling time, τ_f, for T_s = 21 °C (black squares and line), 32 °C (red open triangles and red dashed line) and 41 °C (red triangles and red solid line). The lower and upper boundaries of the error bars represent the minimum and maximum values, respectively, of each group of experiments. The three least squares fitted lines have slopes $\alpha \approx 9$, 42 and 38, corresponding to T_s = 21 °C, 32 °C and 41 °C, respectively. The respective 95% confidence levels in α are [5,13], [28,56] and [15,91]. Each data point in c represents $N \geq 3$ experiments. Scale bar: **(a)–(c)**, 2 mm.

Experimental setup and water temperature calibration. The first step towards performing either static or dynamic droplet experiments on superhydrophobic control and metasurface-coated samples is having a protocol to reliably set the temperatures of the substrate, T_s, and water, T_w. Figure D.5a shows a variant of the experimental setup used throughout the calibration process and subsequent hot water impalement studies. In the case of our first experiments on control superhydrophobic samples (see Appendix D, section "Effect of surface temperature on condensation nucleation on control surfaces due to warm water", and Figure D.4), two identical samples were placed next to each other on top of a copper sheet that was placed on a hot plate. On one of the samples, a resistance temperature detector (RTD) was mounted on its surface, based on which T_s could be regulated. On the other sample, water droplets could be laid or impact, coming out of a height-adjustable syringe. The needle of the syringe was temperature-controlled by sending current through a resistance wire wrapped around it. A side-view high-speed camera and a low-intensity LED light on the opposite side helped visualize possible impalement events. For all sun-like light-driven experiments, the hot plate was replaced by a hollow sample holder and T_s was controlled by illumination provided from the bottom side. A solar simulator and a series of lenses were used to illuminate the whole sample homogeneously and regulate the power density of incident light. For samples illuminated with halogen light, in order to enhance precision, we used the high-speed IR camera instead of the sample mounted RTD for surface temperature measurements.

For the purposes of calibrating T_w, a very thin and sensitive thermocouple was placed in the proximity of the needle tip of the syringe, and different amounts of heating were provided by changing the current sent through the heating wire. Upon thermal equilibrium, water droplets were ejected, one at a time, and the temperature of them, T_w, was recorded by the thermocouple. Figure D.5b shows the calibration curve for T_w, in the form of a plot of T_w [°C] *vs* power provided by the heating wire, P_h [W]. The calibration data can be fitted nicely with a least squares line having the following equation: $T_\mathrm{w} = 7.2P_\mathrm{h} + 19.9$.

Finally, we measured the cooling rate of warm droplets – shown in Figure D.5c – upon dispensing them onto an ambient superhydrophobic control surface from a low height. We used the high-speed IR camera to run three experiments. At $t = 0$, each droplet ($T_\mathrm{w} \approx 65$ °C) was on the surface and we let it cool down for a couple of seconds while recording at a framerate of 100 fps. Ambient temperature was ~23 °C. The fitted curve has the following equation: $T_\mathrm{w} = 23.0 + 41.9\exp\left(-0.4x^{0.8}\right)$.

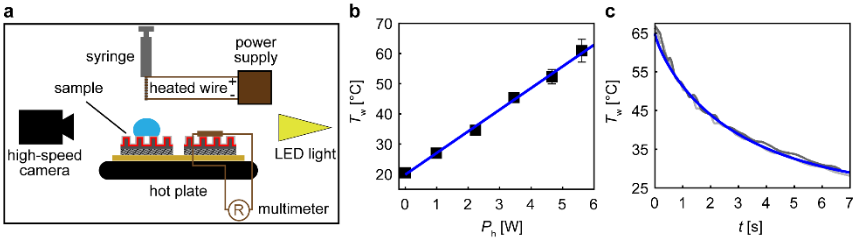

Figure D.5 Experimental configuration and water droplet temperature calibration. (a) Simplified schematic of the setup used for preliminary experiments on control superhydrophobic surfaces. The hot plate was replaced by a converging light beam coming from a solar simulator for the experiments on superhydrophobic metasurfaces. **(b)** Water droplet temperature calibration curve: water droplet temperature, T_w, *vs* power supplied by the heating wire, P_h. A sensitive thermocouple was placed at the edge of the needle of the syringe to measure T_w of ejected water droplets. For each data point, the number of measurements was $N = 3$. **(c)** Water droplet cooling rate plotted as T_w *vs* t. The temperature profiles were measured with a high-speed infrared camera. The blue curve fits all data ($N = 3$ experiments).

Effect of light on the pressure-driven impalement mechanism on metasurfaces. In order to investigate if light has the potential to change the impalement behavior of surfaces even under non-condensing conditions, we investigated the isolated effect of pressure on the impalement of room temperature droplets ($T_\mathrm{w} = T_\infty$) on superhydrophobic metasurfaces. Figure D.6a–b shows image sequences of two water droplets hitting a surface at $We \approx 73$, under no illumination and while the surface was illuminated with our solar simulator ($P \approx 3.5$ kW m^{-2}), respectively. Figure D.6c quantifies impalement probability, *Φ*, for the non-illuminated and illuminated cases. Figure D.6d shows boxplots of the ratio of the initial droplet diameter to the final droplet diameter that – possibly – remains on the surface upon impact, D_imp / D_0 , for the non-illuminated and illuminated surfaces, while Figure D.6e schematically illustrates the pressure-driven impalement mechanism within a cavity.

According to the values of *Φ*, we observe that strong light makes no difference in the impalement probability of room temperature droplets. Thus, we went one step further to investigate whether or not there are any differences in the amount of water that is left behind after an impalement event. For this we picked the cases which showed impalement and quantified the D_imp / D_0 ratio. At first glance, we noticed that in the non-illuminated cases, this ratio can take values within a broad range from 0% to 25%, while for the illuminated cases we observed a less wide distribution of values. However, since both distributions have roughly the same median, a p-test gave a p-value of ~0.15, revealing that the differences we observed are not statistically significant. Possibly, a higher power density or a different (lower) We could lead to statistically significant results.

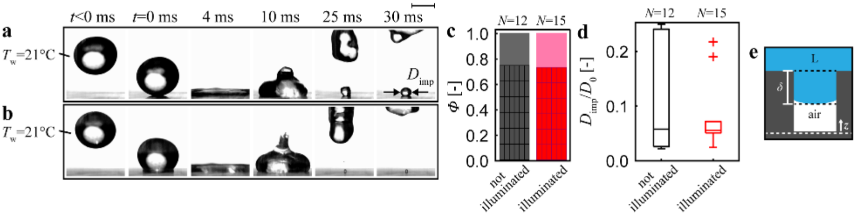

Figure D.6 Effect of light on pressure-driven superhydrophobicity. (a)–(b) Image sequences of room temperature water droplets impacting on a superhydrophobic metasurface ($T_\infty \approx 21$ °C) for **a**, $We \approx 73$, $P = 0$ kW m^{-2}, and **b**, $We \approx 73$, $P \approx 3.5$ kW m^{-2}. A solar simulator was used for illumination. **(c)** Impalement probability, Φ, of room temperature droplets impacting at $We \approx 73$, for $P = 0$ kW m^{-2} and $P \approx 3.5$ kW m^{-2}. Φ corresponds to the crosshatched areas; the remaining area in each bar is $1 - \Phi$. **(d)** Boxplots of impaled to initial droplet diameter, D_{imp}/D_0, of room temperature droplets at $We \approx 73$, for $P = 0$ kW m^{-2} and $P \approx 3.5$ kW m^{-2}. **(e)** Schematic of the pressure-driven impalement mechanism. Scale bar: **(a)–(b)**, 2 mm.

APPENDIX E

Appendix E1

This Appendix includes the permission certificates required for including and reproducing the publications in this thesis.

Metasurfaces leveraging solar energy for icephobicity

Title: Metasurfaces Leveraging Solar Energy for Icephobicity

Author: Efstratios Mitridis, Thomas M. Schutzius, Alba Sicher, et al

Publication: ACS Nano

Publisher: American Chemical Society

Date: Jul 1, 2018

Copyright © 2018, American Chemical Society

Logged in as:
Efstratios Mitridis
ETH Zurich

PERMISSION/LICENSE IS GRANTED FOR YOUR ORDER AT NO CHARGE

This type of permission/license, instead of the standard Terms & Conditions, is sent to you because no fee is being charged for your order. Please note the following:

- Permission is granted for your request in both print and electronic formats, and translations.
- If figures and/or tables were requested, they may be adapted or used in part.
- Please print this page for your records and send a copy of it to your publisher/graduate school.
- Appropriate credit for the requested material should be given as follows: "Reprinted (adapted) with permission from (COMPLETE REFERENCE CITATION). Copyright (YEAR) American Chemical Society." Insert appropriate information in place of the capitalized words.
- One-time permission is granted only for the use specified in your request. No additional uses are granted (such as derivative works or other editions). For any other uses, please submit a new request.

Copyright © 2019 Copyright Clearance Center, Inc. All Rights Reserved. Privacy statement. Terms and Conditions.
Comments? We would like to hear from you. E-mail us at customercare@copyright.com

Transparent metasurfaces counteracting fogging by harnessing sunlight

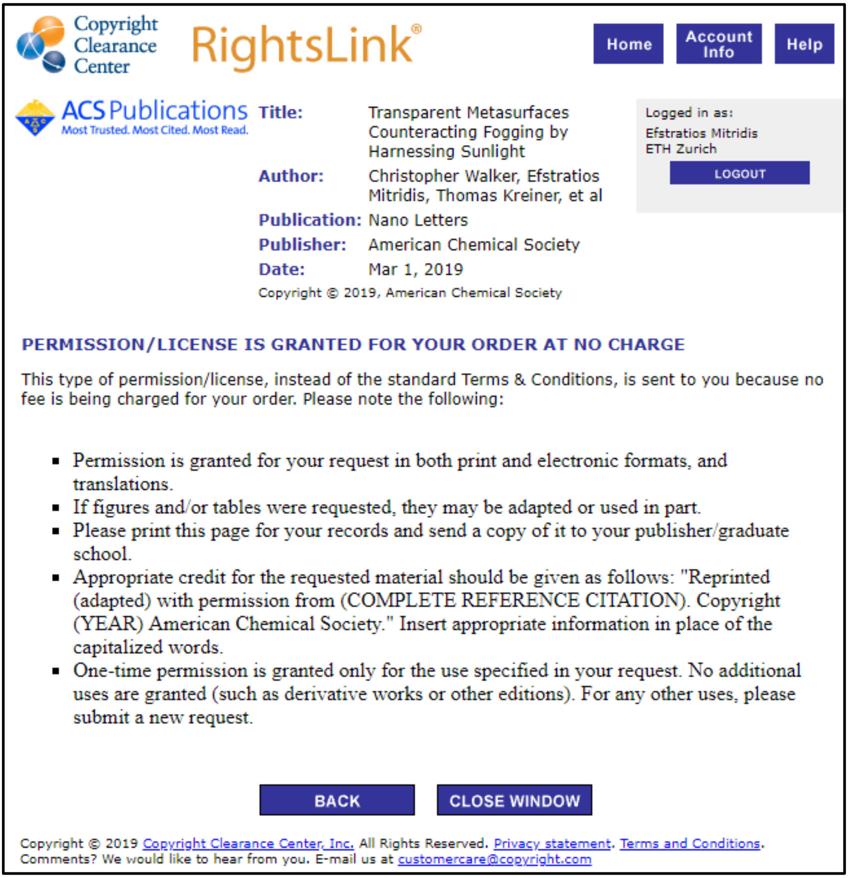

Title: Transparent Metasurfaces Counteracting Fogging by Harnessing Sunlight

Author: Christopher Walker, Efstratios Mitridis, Thomas Kreiner, et al

Publication: Nano Letters

Publisher: American Chemical Society

Date: Mar 1, 2019

Copyright © 2019, American Chemical Society

Logged in as:
Efstratios Mitridis
ETH Zurich

PERMISSION/LICENSE IS GRANTED FOR YOUR ORDER AT NO CHARGE

This type of permission/license, instead of the standard Terms & Conditions, is sent to you because no fee is being charged for your order. Please note the following:

- Permission is granted for your request in both print and electronic formats, and translations.
- If figures and/or tables were requested, they may be adapted or used in part.
- Please print this page for your records and send a copy of it to your publisher/graduate school.
- Appropriate credit for the requested material should be given as follows: "Reprinted (adapted) with permission from (COMPLETE REFERENCE CITATION). Copyright (YEAR) American Chemical Society." Insert appropriate information in place of the capitalized words.
- One-time permission is granted only for the use specified in your request. No additional uses are granted (such as derivative works or other editions). For any other uses, please submit a new request.

Copyright © 2019 Copyright Clearance Center, Inc. All Rights Reserved. Privacy statement. Terms and Conditions.
Comments? We would like to hear from you. E-mail us at customercare@copyright.com

Appendix E2

Metasurfaces leveraging solar energy for icephobicity

Prof. Dr. Dimos Poulikakos conceived the research idea, Prof. Dr. Dimos Poulikakos, Dr. Thomas M. Schutzius, and Dr. Hadi Eghlidi, designed research and provided scientific guidance in all aspects of the work. Efstratios Mitridis, Alba Sicher, and Claudio Hail conducted the experiments and analyzed the results. Prof. Dr. Dimos Poulikakos, Efstratios Mitridis, Dr. Thomas M. Schutzius, and Dr. Hadi Eghlidi wrote the paper draft and all authors participated in manuscript reading, correcting and commenting.

Transparent metasurfaces counteracting fogging by harnessing sunlight

Dr. Thomas M. Schutzius, Dr. Hadi Eghlidi, and Prof. Dr. Dimos Poulikakos designed the research and provided scientific advice on all of its aspects; Christopher Walker, Efstratios Mitridis, and Thomas Kreiner performed experiments and analyzed data; Efstratios Mitridis fabricated and characterized surfaces; Christopher Walker, Efstratios Mitridis, Dr. Thomas M. Schutzius, and Prof. Dr. Dimos Poulikakos wrote the paper.

Transparent metasurfaces naturally boosting their own superhydrophobicity by absorbing sunlight

Dr. Thomas M. Schutzius and Prof. Dr. Dimos Poulikakos designed the research and provided scientific advice throughout its progression; Efstratios Mitridis and Sven Tröber performed experiments, Efstratios Mitridis, Sven Tröber and Henry Lambley analyzed data; Efstratios Mitridis fabricated and characterized the surfaces; Efstratios Mitridis, Dr. Thomas M. Schutzius, Henry Lambley and Prof. Dr. Dimos Poulikakos wrote the paper.

REFERENCES

(1) Schnoor, J. L. Water–Energy Nexus. *Environ. Sci. Technol.* **2011**, *45* (12), 5065–5065. https://doi.org/10.1021/es2016632.

(2) Rijsberman, F. R. Water Scarcity: Fact or Fiction? *Agric. Water Manag.* **2006**, *80* (1–3), 5–22. https://doi.org/10.1016/j.agwat.2005.07.001.

(3) Uri, N. D. A Reconsideration of Effect of Energy Scarcity on Economic Growth. *Energy* **1995**, *20* (1), 1–12. https://doi.org/10.1016/0360-5442(94)00053-6.

(4) Hussey, K.; Pittock, J. The Energy–Water Nexus: Managing the Links between Energy and Water for a Sustainable Future. *Ecol. Soc.* **2012**, *17* (1). https://doi.org/10.5751/ES-04641-170131.

(5) Jacobson, M. Z. Review of Solutions to Global Warming, Air Pollution, and Energy Security. *Energy Environ. Sci.* **2009**, *2* (2), 148–173. https://doi.org/10.1039/b809990c.

(6) Crebolder, J. M.; Sloan, R. B. Determining the Effects of Eyewear Fogging on Visual Task Performance. *Appl. Ergon.* **2004**, *35* (4), 371–381. https://doi.org/10.1016/j.apergo.2004.02.005.

(7) Gent, R. W.; Dart, N. P.; Cansdale, J. T. Aircraft Icing. *Philos. Trans. R. Soc. London. Ser. A Math. Phys. Eng. Sci.* **2000**, *358* (1776), 2873–2911. https://doi.org/10.1098/rsta.2000.0689.

(8) Petrenko, V. F.; Higa, M.; Starostin, M.; Deresh, L. Pulse Electrothermal De-Icing. In *Proceedings of the International Offshore and Polar Engineering Conference*; 2003.

(9) Farzaneh, M. *Atmospheric Icing of Power Networks*; Farzaneh, M., Ed.; Springer Netherlands: Dordrecht, 2008.

(10) Norrman, J.; Eriksson, M.; Lindqvist, S. Relationships between Road Slipperiness, Traffic Accident Risk and Winter Road Maintenance Activity. *Clim. Res.* **2000**, *15* (3), 185–193. https://doi.org/10.3354/cr015185.

(11) Tobiasson, W.; Buska, J.; Greatorex, A. Ventilating Attics to Minimize Icings at Eaves. *Energy Build.* **1994**, *21* (3), 229–234. https://doi.org/10.1016/0378-7788(94)90038-8.

(12) MarketsandMarkets Research Private. Aircraft De-Icing Market worth $1.30 Billion by 2020 https://www.marketsandmarkets.com/PressReleases/aircraft-de-icing.asp (accessed Aug 8, 2017).

(13) MarketsandMarkets Research Private. Ice Protection Systems Market worth 10.17 Billion USD by 2021 https://www.marketsandmarkets.com/PressReleases/ice-protection-system.asp (accessed Aug 8, 2017).

(14) Cole, J.; Sand, W. Statistical Study of Aircraft Icing Accidents. In *29th Aerospace Sciences Meeting*; American Institute of Aeronautics and Astronautics: Reston,

Virigina, 1991.

(15) Schutzius, T. M.; Jung, S.; Maitra, T.; Eberle, P.; Antonini, C.; Stamatopoulos, C.; Poulikakos, D. Physics of Icing and Rational Design of Surfaces with Extraordinary Icephobicity. *Langmuir* **2015**, *31* (17), 4807–4821. https://doi.org/10.1021/la502586a.

(16) Eberle, P.; Tiwari, M. K.; Maitra, T.; Poulikakos, D. Rational Nanostructuring of Surfaces for Extraordinary Icephobicity. *Nanoscale* **2014**, *6* (9), 4874–4881. https://doi.org/10.1039/C3NR06644D.

(17) Boreyko, J. B.; Srijanto, B. R.; Nguyen, T. D.; Vega, C.; Fuentes-Cabrera, M.; Collier, C. P. Dynamic Defrosting on Nanostructured Superhydrophobic Surfaces. *Langmuir* **2013**, *29* (30), 9516–9524. https://doi.org/10.1021/la401282c.

(18) Davis, A.; Yeong, Y. H.; Steele, A.; Bayer, I. S.; Loth, E. Superhydrophobic Nanocomposite Surface Topography and Ice Adhesion. *ACS Appl. Mater. Interfaces* **2014**, *6* (12), 9272–9279. https://doi.org/10.1021/am501640h.

(19) Meuler, A. J.; Smith, J. D.; Varanasi, K. K.; Mabry, J. M.; McKinley, G. H.; Cohen, R. E. Relationships between Water Wettability and Ice Adhesion. *ACS Appl. Mater. Interfaces* **2010**, *2* (11), 3100–3110. https://doi.org/10.1021/am1006035.

(20) Chen, X.; Ma, R.; Zhou, H.; Zhou, X.; Che, L.; Yao, S.; Wang, Z. Activating the Microscale Edge Effect in a Hierarchical Surface for Frosting Suppression and Defrosting Promotion. *Sci. Rep.* **2013**, *3* (1), 2515. https://doi.org/10.1038/srep02515.

(21) Kreder, M. J.; Alvarenga, J.; Kim, P.; Aizenberg, J. Design of Anti-Icing Surfaces: Smooth, Textured or Slippery? *Nat. Rev. Mater.* **2016**, *1* (1), 15003. https://doi.org/10.1038/natrevmats.2015.3.

(22) Kim, P.; Wong, T.-S.; Alvarenga, J.; Kreder, M. J.; Adorno-Martinez, W. E.; Aizenberg, J. Liquid-Infused Nanostructured Surfaces with Extreme Anti-Ice and Anti-Frost Performance. *ACS Nano* **2012**, *6* (8), 6569–6577. https://doi.org/10.1021/nn302310q.

(23) Zhu, L.; Xue, J.; Wang, Y.; Chen, Q.; Ding, J.; Wang, Q. Ice-Phobic Coatings Based on Silicon-Oil-Infused Polydimethylsiloxane. *ACS Appl. Mater. Interfaces* **2013**, *5* (10), 4053–4062. https://doi.org/10.1021/am400704z.

(24) Parent, O.; Ilinca, A. Anti-Icing and de-Icing Techniques for Wind Turbines: Critical Review. *Cold Reg. Sci. Technol.* **2011**, *65* (1), 88–96. https://doi.org/10.1016/j.coldregions.2010.01.005.

(25) Rashid, T.; Khawaja, H. A.; Edvardsen, K. Review of Marine Icing and Anti-/de-Icing Systems. *J. Mar. Eng. Technol.* **2016**, *15* (2), 79–87. https://doi.org/10.1080/20464177.2016.1216734.

(26) Wong, T.-S.; Kang, S. H.; Tang, S. K. Y.; Smythe, E. J.; Hatton, B. D.; Grinthal, A.; Aizenberg, J. Bioinspired Self-Repairing Slippery Surfaces with Pressure-Stable Omniphobicity. *Nature* **2011**, *477* (7365), 443–447. https://doi.org/10.1038/nature10447.

(27) Dong, H.; Ye, P.; Zhong, M.; Pietrasik, J.; Drumright, R.; Matyjaszewski, K. Superhydrophilic Surfaces via Polymer−SiO2 Nanocomposites. *Langmuir* **2010**, *26* (19), 15567–15573. https://doi.org/10.1021/la102145s.

(28) Zhao, J.; Ma, L.; Millians, W.; Wu, T.; Ming, W. Dual-Functional Antifogging/Antimicrobial Polymer Coating. *ACS Appl. Mater. Interfaces* **2016**, *8* (13), 8737–8742. https://doi.org/10.1021/acsami.6b00748.

(29) Gao, X.; Yan, X.; Yao, X.; Xu, L.; Zhang, K.; Zhang, J.; Yang, B.; Jiang, L. The Dry-Style Antifogging Properties of Mosquito Compound Eyes and Artificial Analogues Prepared by Soft Lithography. *Adv. Mater.* **2007**, *19* (17), 2213–2217. https://doi.org/10.1002/adma.200601946.

(30) Sun, Z.; Liao, T.; Liu, K.; Jiang, L.; Kim, J. H.; Dou, S. X. Fly-Eye Inspired Superhydrophobic Anti-Fogging Inorganic Nanostructures. *Small* **2014**, *10* (15), 3001–3006. https://doi.org/10.1002/smll.201400516.

(31) Mouterde, T.; Lehoucq, G.; Xavier, S.; Checco, A.; Black, C. T.; Rahman, A.; Midavaine, T.; Clanet, C.; Quéré, D. Antifogging Abilities of Model Nanotextures. *Nat. Mater.* **2017**, *16* (6), 658–663. https://doi.org/10.1038/nmat4868.

(32) Sharma, C. S.; Stamatopoulos, C.; Suter, R.; von Rohr, P. R.; Poulikakos, D. Rationally 3D-Textured Copper Surfaces for Laplace Pressure Imbalance-Induced Enhancement in Dropwise Condensation. *ACS Appl. Mater. Interfaces* **2018**, *10* (34), 29127–29135. https://doi.org/10.1021/acsami.8b09067.

(33) Howarter, J. A.; Youngblood, J. P. Self-Cleaning and Next Generation Anti-Fog Surfaces and Coatings. *Macromol. Rapid Commun.* **2008**, *29* (6), 455–466. https://doi.org/10.1002/marc.200700733.

(34) Cheng, Y. T.; Rodak, D. E. Is the Lotus Leaf Superhydrophobic? *Appl. Phys. Lett.* **2005**, *86* (14), 1–3. https://doi.org/10.1063/1.1895487.

(35) Varanasi, K. K.; Hsu, M.; Bhate, N.; Yang, W.; Deng, T. Spatial Control in the Heterogeneous Nucleation of Water. *Appl. Phys. Lett.* **2009**, *95* (9), 094101. https://doi.org/10.1063/1.3200951.

(36) Soto, D.; Ugur, A.; Farnham, T. A.; Gleason, K. K.; Varanasi, K. K. Short-Fluorinated ICVD Coatings for Nonwetting Fabrics. *Adv. Funct. Mater.* **2018**, *28* (33), 1707355. https://doi.org/10.1002/adfm.201707355.

(37) Peng, C.; Chen, Z.; Tiwari, M. K. All-Organic Superhydrophobic Coatings with Mechanochemical Robustness and Liquid Impalement Resistance. *Nat. Mater.* **2018**, *17* (4), 355–360. https://doi.org/10.1038/s41563-018-0044-2.

(38) Tuteja, A.; Choi, W.; Ma, M.; Mabry, J. M.; Mazzella, S. A.; Rutledge, G. C.; McKinley, G. H.; Cohen, R. E. Designing Superoleophobic Surfaces. *Science (80-.).* **2007**, *318* (5856), 1618–1622. https://doi.org/10.1126/science.1148326.

(39) Wu, S. *Polymer Interface and Adhesion*; Routledge, 2017. https://doi.org/10.1201/9780203742860.

(40) Mishchenko, L.; Hatton, B.; Bahadur, V.; Taylor, J. A.; Krupenkin, T.; Aizenberg, J. Design of Ice-Free Nanostructured Surfaces Based on Repulsion of Impacting Water Droplets. *ACS Nano* **2010**, *4* (12), 7699–7707. https://doi.org/10.1021/nn102557p.

(41) Lai, Y.; Gao, X.; Zhuang, H.; Huang, J.; Lin, C.; Jiang, L. Designing Superhydrophobic Porous Nanostructures with Tunable Water Adhesion. *Adv. Mater.* **2009**, *21* (37), 3799–3803. https://doi.org/10.1002/adma.200900686.

(42) Maitra, T.; Jung, S.; Giger, M. E.; Kandrical, V.; Ruesch, T.; Poulikakos, D. Superhydrophobicity vs. Ice Adhesion: The Quandary of Robust Icephobic Surface Design. *Adv. Mater. Interfaces* **2015**, *2* (16), 1500330. https://doi.org/10.1002/admi.201500330.

(43) Boreyko, J. B.; Collier, C. P. Dewetting Transitions on Superhydrophobic Surfaces: When Are Wenzel Drops Reversible? *J. Phys. Chem. C* **2013**, *117* (35), 18084–18090. https://doi.org/10.1021/jp4053083.

(44) Feng, L.; Li, S.; Li, Y.; Li, H.; Zhang, L.; Zhai, J.; Song, Y.; Liu, B.; Jiang, L.; Zhu, D. Super-Hydrophobic Surfaces: From Natural to Artificial. *Adv. Mater.* **2002**, *14* (24), 1857–1860. https://doi.org/10.1002/adma.200290020.

(45) Liu, M.; Wang, S.; Jiang, L. Nature-Inspired Superwettability Systems. *Nat. Rev. Mater.* **2017**, *2* (7), 17036. https://doi.org/10.1038/natrevmats.2017.36.

(46) McCarthy, M.; Gerasopoulos, K.; Enright, R.; Culver, J. N.; Ghodssi, R.; Wang, E. N. Biotemplated Hierarchical Surfaces and the Role of Dual Length Scales on the Repellency of Impacting Droplets. *Appl. Phys. Lett.* **2012**, *100* (26), 1–6. https://doi.org/10.1063/1.4729935.

(47) Patankar, N. A. Mimicking the Lotus Effect: Influence of Double Roughness Structures and Slender Pillars. *Langmuir* **2004**, *20* (19), 8209–8213. https://doi.org/10.1021/la048629t.

(48) Vasileiou, T.; Gerber, J.; Prautzsch, J.; Schutzius, T. M.; Poulikakos, D. Superhydrophobicity Enhancement through Substrate Flexibility. *Proc. Natl. Acad. Sci.* **2016**, *113* (47), 13307–13312. https://doi.org/10.1073/pnas.1611631113.

(49) Vasileiou, T.; Schutzius, T. M.; Poulikakos, D. Imparting Icephobicity with Substrate Flexibility. *Langmuir* **2017**, *33* (27), 6708–6718. https://doi.org/10.1021/acs.langmuir.7b01412.

(50) Mouterde, T.; Lecointre, P.; Lehoucq, G.; Checco, A.; Clanet, C.; Quéré, D. Two

Recipes for Repelling Hot Water. *Nat. Commun.* **2019**, *10* (1), 1410. https://doi.org/10.1038/s41467-019-09456-8.

(51) Liu, Y.; Chen, X.; Xin, J. H. Can Superhydrophobic Surfaces Repel Hot Water? *J. Mater. Chem.* **2009**, *19* (31), 5602. https://doi.org/10.1039/b822168e.

(52) Zhu, P.; Chen, R.; Wang, L. Topography-Directed Hot-Water Super-Repellent Surfaces. *Adv. Sci.* **2019**, *1900798*. https://doi.org/10.1002/advs.201900798.

(53) Wan, F.; Yang, D.-Q.; Sacher, E. Repelling Hot Water from Superhydrophobic Surfaces Based on Carbon Nanotubes. *J. Mater. Chem. A* **2015**, *3* (33), 16953–16960. https://doi.org/10.1039/C5TA05231A.

(54) Dorrer, C.; Rühe, J. Condensation and Wetting Transitions on Microstructured Ultrahydrophobic Surfaces. *Langmuir* **2007**, *23* (7), 3820–3824. https://doi.org/10.1021/la063130f.

(55) Krupenkin, T. N.; Taylor, J. A.; Wang, E. N.; Kolodner, P.; Hodes, M.; Salamon, T. R. Reversible Wetting−Dewetting Transitions on Electrically Tunable Superhydrophobic Nanostructured Surfaces. *Langmuir* **2007**, *23* (18), 9128–9133. https://doi.org/10.1021/la7008557.

(56) de Gennes, P. G.; Brochard-Wyart, F.; Quéré, D. *Capillarity and Wetting Phenomena*; Springer: New York, 2004. https://doi.org/10.1007/978-0-387-21656-0.

(57) Bonn, D.; Eggers, J.; Indekeu, J.; Meunier, J.; Rolley, E. Wetting and Spreading. *Rev. Mod. Phys.* **2009**, *81* (2), 739–805. https://doi.org/10.1103/RevModPhys.81.739.

(58) Gupta, M.; Gleason, K. K. Initiated Chemical Vapor Deposition of Poly(1H,1H,2H,2H-Perfluorodecyl Acrylate) Thin Films. *Langmuir* **2006**, *22* (24), 10047–10052. https://doi.org/10.1021/la061904m.

(59) Quéré, D. Wetting and Roughness. *Annu. Rev. Mater. Res.* **2008**, *38* (1), 71–99. https://doi.org/10.1146/annurev.matsci.38.060407.132434.

(60) Wang, S.; Jiang, L. Definition of Superhydrophobic States. *Adv. Mater.* **2007**, *19* (21), 3423–3424. https://doi.org/10.1002/adma.200700934.

(61) Rioboo, R.; Voué, M.; Vaillant, A.; De Coninck, J. Drop Impact on Porous Superhydrophobic Polymer Surfaces. *Langmuir* **2008**, *24* (24), 14074–14077. https://doi.org/10.1021/la802897g.

(62) Yu, Z.-J.; Yang, J.; Wan, F.; Ge, Q.; Yang, L.-L.; Ding, Z.-L.; Yang, D.-Q.; Sacher, E.; Isimjan, T. T. How to Repel Hot Water from a Superhydrophobic Surface? *J. Mater. Chem. A* **2014**, *2* (27), 10639–10646. https://doi.org/10.1039/C4TA00882K.

(63) Standnes, A. Binary Phase Diagram Plotter https://www.chemix-chemistry-software.com/school/binary-phase-diagram-plotter.html (accessed Aug 27, 2019).

(64) Debenedetti, P. G. *Metastable Liquids: Concepts and Principles*; Princeton University Press, 1996.

(65) Poole, P. H.; Sciortino, F.; Essmann, U.; Stanley, H. E. Phase Behaviour of Metastable Water. *Nature* **1992**, *360* (6402), 324–328. https://doi.org/10.1038/360324a0.

(66) Hobbs, P. V. *Ice Physics*; Clarednon Press: Oxford, 1974.

(67) Turnbull, D.; Fisher, J. C. Rate of Nucleation in Condensed Systems. *J. Chem. Phys.* **1949**, *17* (1), 71–73. https://doi.org/10.1063/1.1747055.

(68) McDonald, J. E. Homogeneous Nucleation of Supercooled Water Drops. *J. Meteorol.* **1953**, *10* (6), 416–433. https://doi.org/10.1175/1520-0469(1953)010<0416:HNOSWD>2.0.CO;2.

(69) Murphy, D. M.; Koop, T. Review of the Vapour Pressures of Ice and Supercooled Water for Atmospheric Applications. *Q. J. R. Meteorol. Soc.* **2005**, *131* (608), 1539–1565. https://doi.org/10.1256/qj.04.94.

(70) Na, B.; Webb, R. L. A Fundamental Understanding of Factors Affecting Frost Nucleation. *Int. J. Heat Mass Transf.* **2003**, *46* (20), 3797–3808. https://doi.org/10.1016/S0017-9310(03)00194-7.

(71) Cai, W.; Shalaev, V. *Optical Metamaterials: Fundamentals and Applications*; Springer: New York, 2010. https://doi.org/10.1007/978-1-4419-1151-3.

(72) Freestone, I.; Meeks, N.; Sax, M.; Higgitt, C. The Lycurgus Cup — A Roman Nanotechnology. *Gold Bull.* **2007**, *40* (4), 270–277. https://doi.org/10.1007/BF03215599.

(73) Boardman, A. Pioneers in Metamaterials: John Pendry and Victor Veselago. *J. Opt.* **2011**, *13* (2), 020401. https://doi.org/10.1088/2040-8978/13/2/020401.

(74) Gall, D. Electron Mean Free Path in Elemental Metals. *J. Appl. Phys.* **2016**, *119* (8), 085101. https://doi.org/10.1063/1.4942216.

(75) Yeh, P. *Optical Waves in Layered Media*; Wiley: New Jersey, 2005.

(76) Hedayati, M.; Faupel, F.; Elbahri, M. Review of Plasmonic Nanocomposite Metamaterial Absorber. *Materials (Basel).* **2014**, *7* (2), 1221–1248. https://doi.org/10.3390/ma7021221.

(77) Khurgin, J. B. How to Deal with the Loss in Plasmonics and Metamaterials. *Nat. Nanotechnol.* **2015**, *10* (1), 2–6. https://doi.org/10.1038/nnano.2014.310.

(78) Li, X.; Xiao, D.; Zhang, Z. Landau Damping of Quantum Plasmons in Metal Nanostructures. *New J. Phys.* **2013**, *15* (2), 023011. https://doi.org/10.1088/1367-2630/15/2/023011.

(79) Govorov, A. O.; Richardson, H. H. Generating Heat with Metal Nanoparticles. *Nano Today* **2007**, *2* (1), 30–38. https://doi.org/10.1016/S1748-0132(07)70017-8.

(80) Govorov, A. O.; Zhang, W.; Skeini, T.; Richardson, H.; Lee, J.; Kotov, N. A. Gold Nanoparticle Ensembles as Heaters and Actuators: Melting and Collective Plasmon Resonances. *Nanoscale Res. Lett.* **2006**, *1* (1), 84–90. https://doi.org/10.1007/s11671-006-9015-7.

(81) Fillion, R. M.; Riahi, A. R.; Edrisy, A. A Review of Icing Prevention in Photovoltaic Devices by Surface Engineering. *Renew. Sustain. Energy Rev.* **2014**, *32*, 797–809. https://doi.org/10.1016/j.rser.2014.01.015.

(82) Farag, A.; Huang, L. J. CFD Analysis and Validation of Automotive Windshield De-Icing Simulation. *SAE Tech. Pap.* **2003**, No. 1079. https://doi.org/10.4271/2003-01-1079.

(83) Yang, P.; Sun, P.; Chai, Z.; Huang, L.; Cai, X.; Tan, S.; Song, J.; Mai, W. Large-Scale Fabrication of Pseudocapacitive Glass Windows That Combine Electrochromism and Energy Storage. *Angew. Chemie Int. Ed.* **2014**, *53* (44), 11935–11939. https://doi.org/10.1002/anie.201407365.

(84) Martín-Palma, R. J.; Vázquez, L.; Martínez-Duart, J. M.; Malats-Riera. Silver-Based Low-Emissivity Coatings for Architectural Windows: Optical and Structural Properties. *Sol. Energy Mater. Sol. Cells* **1998**, *53* (1–2), 55–66.

(85) Deng, X.; Schellenberger, F.; Papadopoulos, P.; Vollmer, D.; Butt, H.-J. Liquid Drops Impacting Superamphiphobic Coatings. *Langmuir* **2013**, *29* (25), 7847–7856. https://doi.org/10.1021/la401120j.

(86) He, X.; Liu, A.; Hu, X.; Song, M.; Duan, F.; Lan, Q.; Xiao, J.; Liu, J.; Zhang, M.; Chen, Y.; et al. Temperature-Controlled Transparent-Film Heater Based on Silver Nanowire–PMMA Composite Film. *Nanotechnology* **2016**, *27* (47), 475709. https://doi.org/10.1088/0957-4484/27/47/475709.

(87) Irajizad, P.; Hasnain, M.; Farokhnia, N.; Sajadi, S. M.; Ghasemi, H. Magnetic Slippery Extreme Icephobic Surfaces. *Nat. Commun.* **2016**, *7* (1), 13395. https://doi.org/10.1038/ncomms13395.

(88) Zhou, L.; Tan, Y.; Wang, J.; Xu, W.; Yuan, Y.; Cai, W.; Zhu, S.; Zhu, J. 3D Self-Assembly of Aluminium Nanoparticles for Plasmon-Enhanced Solar Desalination. *Nat. Photonics* **2016**, *10* (6), 393–398. https://doi.org/10.1038/nphoton.2016.75.

(89) Clavero, C. Plasmon-Induced Hot-Electron Generation at Nanoparticle/Metal-Oxide Interfaces for Photovoltaic and Photocatalytic Devices. *Nat. Photonics* **2014**, *8* (2), 95–103. https://doi.org/10.1038/nphoton.2013.238.

(90) Boström, T.; Westin, G.; Wäckelgård, E. Optimization of a Solution-Chemically Derived Solar Absorbing Spectrally Selective Surface. *Sol. Energy Mater. Sol. Cells* **2007**, *91* (1), 38–43. https://doi.org/10.1016/j.solmat.2006.07.002.

(91) Sarina, S.; Waclawik, E. R.; Zhu, H. Photocatalysis on Supported Gold and Silver Nanoparticles under Ultraviolet and Visible Light Irradiation. *Green Chem.* **2013**, *15* (7), 1814. https://doi.org/10.1039/c3gc40450a.

(92) Brongersma, M. L.; Halas, N. J.; Nordlander, P. Plasmon-Induced Hot Carrier Science and Technology. *Nat. Nanotechnol.* **2015**, *10* (1), 25–34. https://doi.org/10.1038/nnano.2014.311.

(93) Wu, K.; Chen, J.; McBride, J. R.; Lian, T. Efficient Hot-Electron Transfer by a Plasmon-Induced Interfacial Charge-Transfer Transition. *Science (80-.).* **2015**, *349* (6248), 632–635. https://doi.org/10.1126/science.aac5443.

(94) Qin, Z.; Wang, Y.; Randrianalisoa, J.; Raeesi, V.; Chan, W. C. W.; Lipiński, W.; Bischof, J. C. Quantitative Comparison of Photothermal Heat Generation between Gold Nanospheres and Nanorods. *Sci. Rep.* **2016**, *6* (1), 29836. https://doi.org/10.1038/srep29836.

(95) Hedayati, M. K.; Javaherirahim, M.; Mozooni, B.; Abdelaziz, R.; Tavassolizadeh, A.; Chakravadhanula, V. S. K.; Zaporojtchenko, V.; Strunkus, T.; Faupel, F.; Elbahri, M. Design of a Perfect Black Absorber at Visible Frequencies Using Plasmonic Metamaterials. *Adv. Mater.* **2011**, *23* (45), 5410–5414. https://doi.org/10.1002/adma.201102646.

(96) Incropera, F. P.; DeWitt, D. P.; Bergman, T. L.; Lavine, A. S. *Fundamentals of Heat and Mass Transfer*, 6th ed.; John Wiley & Sons, 2006.

(97) Perry, R. H.; Green, D. W.; Maloney, J. O. *Perry's Chemical Engineers' Handbook*, 7th ed.; McGraw-Hill: New York, 1997.

(98) Jung, S.; Tiwari, M. K.; Poulikakos, D. Frost Halos from Supercooled Water Droplets. *Proc. Natl. Acad. Sci.* **2012**, *109* (40), 16073–16078. https://doi.org/10.1073/pnas.1206121109.

(99) Chevallier, P.; Turgeon, S.; Sarra-Bournet, C.; Turcotte, R.; Laroche, G. Characterization of Multilayer Anti-Fog Coatings. *ACS Appl. Mater. Interfaces* **2011**, *3* (3), 750–758. https://doi.org/10.1021/am1010964.

(100) Lee, H.; Alcaraz, M. L.; Rubner, M. F.; Cohen, R. E. Zwitter-Wettability and Antifogging Coatings with Frost-Resisting Capabilities. *ACS Nano* **2013**, *7* (3), 2172–2185. https://doi.org/10.1021/nn3057966.

(101) Papadopoulos, P.; Mammen, L.; Deng, X.; Vollmer, D.; Butt, H. How Superhydrophobicity Breaks Down. *Proc. Natl. Acad. Sci.* **2013**, *110* (9), 3254–3258. https://doi.org/10.1073/pnas.1218673110.

(102) Wier, K. A.; McCarthy, T. J. Condensation on Ultrahydrophobic Surfaces and Its Effect on Droplet Mobility: Ultrahydrophobic Surfaces Are Not Always Water Repellant. *Langmuir* **2006**, *22* (6), 2433–2436. https://doi.org/10.1021/la0525877.

(103) Boreyko, J. B.; Chen, C.-H. Self-Propelled Dropwise Condensate on Superhydrophobic Surfaces. *Phys. Rev. Lett.* **2009**, *103* (18), 184501. https://doi.org/10.1103/PhysRevLett.103.184501.

(104) Wang, F.-C.; Yang, F.; Zhao, Y.-P. Size Effect on the Coalescence-Induced Self-

Propelled Droplet. *Appl. Phys. Lett.* **2011**, *98* (5), 053112. https://doi.org/10.1063/1.3553782.

(105) Wisdom, K. M.; Watson, J. A.; Qu, X.; Liu, F.; Watson, G. S.; Chen, C.-H. Self-Cleaning of Superhydrophobic Surfaces by Self-Propelled Jumping Condensate. *Proc. Natl. Acad. Sci.* **2013**, *110* (20), 7992–7997. https://doi.org/10.1073/pnas.1210770110.

(106) Miljkovic, N.; Enright, R.; Nam, Y.; Lopez, K.; Dou, N.; Sack, J.; Wang, E. N. Jumping-Droplet-Enhanced Condensation on Scalable Superhydrophobic Nanostructured Surfaces. *Nano Lett.* **2013**, *13* (1), 179–187. https://doi.org/10.1021/nl303835d.

(107) Sharma, C. S.; Combe, J.; Giger, M.; Emmerich, T.; Poulikakos, D. Growth Rates and Spontaneous Navigation of Condensate Droplets Through Randomly Structured Textures. *ACS Nano* **2017**, *11* (2), 1673–1682. https://doi.org/10.1021/acsnano.6b07471.

(108) Brongersma, M. L.; Halas, N. J.; Nordlander, P. Plasmon-Induced Hot Carrier Science and Technology. *Nat. Nanotechnol.* **2015**, *10* (1), 25–34. https://doi.org/10.1038/nnano.2014.311.

(109) Neumann, O.; Urban, A. S.; Day, J.; Lal, S.; Nordlander, P.; Halas, N. J. Solar Vapor Generation Enabled by Nanoparticles. *ACS Nano* **2013**, *7* (1), 42–49. https://doi.org/10.1021/nn304948h.

(110) Neumann, O.; Feronti, C.; Neumann, A. D.; Dong, A.; Schell, K.; Lu, B.; Kim, E.; Quinn, M.; Thompson, S.; Grady, N.; et al. Compact Solar Autoclave Based on Steam Generation Using Broadband Light-Harvesting Nanoparticles. *Proc. Natl. Acad. Sci.* **2013**, *110* (29), 11677–11681. https://doi.org/10.1073/pnas.1310131110.

(111) Ni, G.; Li, G.; Boriskina, S. V.; Li, H.; Yang, W.; Zhang, T.; Chen, G. Steam Generation under One Sun Enabled by a Floating Structure with Thermal Concentration. *Nat. Energy* **2016**, *1* (9), 16126. https://doi.org/10.1038/nenergy.2016.126.

(112) Adleman, J. R.; Boyd, D. A.; Goodwin, D. G.; Psaltis, D. Heterogenous Catalysis Mediated by Plasmon Heating. *Nano Lett.* **2009**, *9* (12), 4417–4423. https://doi.org/10.1021/nl902711n.

(113) Naldoni, A.; Shalaev, V. M.; Brongersma, M. L. Applying Plasmonics to a Sustainable Future. *Science (80-.).* **2017**, *356* (6341), 908–909. https://doi.org/10.1126/science.aan5802.

(114) Kuzyk, A.; Schreiber, R.; Zhang, H.; Govorov, A. O.; Liedl, T.; Liu, N. Reconfigurable 3D Plasmonic Metamolecules. *Nat. Mater.* **2014**, *13* (9), 862–866. https://doi.org/10.1038/nmat4031.

(115) Jonsson, G. E.; Miljkovic, V.; Dmitriev, A. Nanoplasmon-Enabled Macroscopic Thermal Management. *Sci. Rep.* **2015**, *4* (1), 5111.

https://doi.org/10.1038/srep05111.

(116) Jönsson, G.; Tordera, D.; Pakizeh, T.; Jaysankar, M.; Miljkovic, V.; Tong, L.; Jonsson, M. P.; Dmitriev, A. Solar Transparent Radiators by Optical Nanoantennas. *Nano Lett.* **2017**, *17* (11), 6766–6772. https://doi.org/10.1021/acs.nanolett.7b02962.

(117) Park, S.-H.; Lee, S.-M.; Ko, E.-H.; Kim, T.-H.; Nah, Y.-C.; Lee, S.-J.; Lee, J. H.; Kim, H.-K. Roll-to-Roll Sputtered ITO/Cu/ITO Multilayer Electrode for Flexible, Transparent Thin Film Heaters and Electrochromic Applications. *Sci. Rep.* **2016**, *6* (1), 33868. https://doi.org/10.1038/srep33868.

(118) Kukla, R. Magnetron Sputtering on Large Scale Substrates: An Overview on the State of the Art. *Surf. Coatings Technol.* **1997**, *93* (1), 1–6. https://doi.org/10.1016/S0257-8972(97)00018-2.

(119) Bruix, A.; Lykhach, Y.; Matolínová, I.; Neitzel, A.; Skála, T.; Tsud, N.; Vorokhta, M.; Stetsovych, V.; Ševčíková, K.; Mysliveček, J.; et al. Maximum Noble-Metal Efficiency in Catalytic Materials: Atomically Dispersed Surface Platinum. *Angew. Chemie Int. Ed.* **2014**, *53* (39), 10525–10530. https://doi.org/10.1002/anie.201402342.

(120) You, Y.; Zhao, H.; Vance, G. F. Surfactant-Enhanced Adsorption of Organic Compounds by Layered Double Hydroxides. *Colloids Surfaces A Physicochem. Eng. Asp.* **2002**, *205* (3), 161–172. https://doi.org/10.1016/S0927-7757(01)01137-2.

(121) Burns, N. R.; Nettelbeck, T.; White, M.; Willson, J. Effects of Car Window Tinting on Visual Performance: A Comparison of Elderly and Young Drivers. *Ergonomics* **1999**, *42* (3), 428–443. https://doi.org/10.1080/001401399185577.

(122) LaMotte, J.; Ridder, W.; Yeung, K.; De Land, P. Effect of Aftermarket Automobile Window Tinting Films on Driver Vision. *Hum. Factors J. Hum. Factors Ergon. Soc.* **2000**, *42* (2), 327–336. https://doi.org/10.1518/001872000779656552.

(123) Chow, T.; Li, C.; Lin, Z. Innovative Solar Windows for Cooling-Demand Climate. *Sol. Energy Mater. Sol. Cells* **2010**, *94* (2), 212–220. https://doi.org/10.1016/j.solmat.2009.09.004.

(124) Bhattacharya, R. . Evaluation of High Energy Ion-Implanted Polycarbonate for Eyewear Applications. *Surf. Coatings Technol.* **1998**, *103–104*, 151–155. https://doi.org/10.1016/S0257-8972(98)00368-5.

(125) Ma, C.; Taya, M.; Xu, C. Smart Sunglasses Based on Electrochromic Polymers. *Polym. Eng. Sci.* **2008**, *48* (11), 2224–2228. https://doi.org/10.1002/pen.21169.

(126) McHale, G.; Rowan, S. M.; Newton, M. I.; Banerjee, M. K. Evaporation and the Wetting of a Low-Energy Solid Surface. *J. Phys. Chem. B* **1998**, *102* (11), 1964–1967. https://doi.org/10.1021/jp972552i.

(127) Kulinich, S. A.; Farzaneh, M. Effect of Contact Angle Hysteresis on Water Droplet

Evaporation from Super-Hydrophobic Surfaces. *Appl. Surf. Sci.* **2009**, *255* (7), 4056–4060. https://doi.org/10.1016/j.apsusc.2008.10.109.

(128) Karapanagiotis, I.; Aifantis, K. E.; Konstantinidis, A. Capturing the Evaporation Process of Water Drops on Sticky Superhydrophobic Polymer-Nanoparticle Surfaces. *Mater. Lett.* **2016**, *164*, 117–119. https://doi.org/10.1016/j.matlet.2015.10.110.

(129) Birdi, K. S.; Vu, D. T. Wettability and the Evaporation Rates of Fluids from Solid Surfaces. *J. Adhes. Sci. Technol.* **1993**, *7* (6), 485–493. https://doi.org/10.1163/156856193X00808.

(130) Mitridis, E.; Schutzius, T. M.; Sicher, A.; Hail, C. U.; Eghlidi, H.; Poulikakos, D. Metasurfaces Leveraging Solar Energy for Icephobicity. *ACS Nano* **2018**, *12* (7), 7009–7017. https://doi.org/10.1021/acsnano.8b02719.

(131) Thünemann, A. F.; Lieske, A.; Paulke, B.-R. Low Surface Energy Coatings from Waterborne Nano-Dispersions of Polymer Complexes. *Adv. Mater.* **1999**, *11* (4), 321–324. https://doi.org/10.1002/(SICI)1521-4095(199903)11:4<321::AID-ADMA321>3.0.CO;2-M.

(132) Im, S. G.; Bong, K. W.; Lee, C.-H.; Doyle, P. S.; Gleason, K. K. A Conformal Nano-Adhesive via Initiated Chemical Vapor Deposition for Microfluidic Devices. *Lab Chip* **2009**, *9* (3), 411–416. https://doi.org/10.1039/B812121D.

(133) Coray, P. S.; Lipiński, W.; Steinfeld, A. Spectroscopic Goniometry System for Determining Thermal Radiative Properties of Participating Media. *Exp. Heat Transf.* **2011**, *24* (4), 300–312. https://doi.org/10.1080/08916152.2011.556311.

(134) Barthlott, W.; Neinhuis, C. Purity of the Sacred Lotus, or Escape from Contamination in Biological Surfaces. *Planta* **1997**, *202* (1), 1–8. https://doi.org/10.1007/s004250050096.

(135) Zheng, Y.; Gao, X.; Jiang, L. Directional Adhesion of Superhydrophobic Butterfly Wings. *Soft Matter* **2007**, *3* (2), 178–182. https://doi.org/10.1039/B612667G.

(136) Gao, X.; Jiang, L. Water-Repellent Legs of Water Striders. *Nature* **2004**, *432* (7013), 36–36. https://doi.org/10.1038/432036a.

(137) Blossey, R. Self-Cleaning Surfaces — Virtual Realities. *Nat. Mater.* **2003**, *2* (5), 301–306. https://doi.org/10.1038/nmat856.

(138) Genzer, J.; Efimenko, K. Recent Developments in Superhydrophobic Surfaces and Their Relevance to Marine Fouling: A Review. *Biofouling* **2006**, *22* (5), 339–360. https://doi.org/10.1080/08927010600980223.

(139) Jung, S.; Tiwari, M. K.; Doan, N. V.; Poulikakos, D. Mechanism of Supercooled Droplet Freezing on Surfaces. *Nat. Commun.* **2012**, *3* (1), 615. https://doi.org/10.1038/ncomms1630.

(140) Cassie, A. B. D.; Baxter, S. Wettability of Porous Surfaces. *Trans. Faraday Soc.*

1944, *40* (5), 546. https://doi.org/10.1039/tf9444000546.

(141) Wenzel, R. N. Resistance of Solid Surfaces to Wetting by Water. *Ind. Eng. Chem.* **1936**, *28* (8), 988–994. https://doi.org/10.1021/ie50320a024.

(142) Maitra, T.; Tiwari, M. K.; Antonini, C.; Schoch, P.; Jung, S.; Eberle, P.; Poulikakos, D. On the Nanoengineering of Superhydrophobic and Impalement Resistant Surface Textures below the Freezing Temperature. *Nano Lett.* **2014**, *14* (1), 172–182. https://doi.org/10.1021/nl4037092.

(143) Reyssat, M.; Pépin, A.; Marty, F.; Chen, Y.; Quéré, D. Bouncing Transitions on Microtextured Materials. *Europhys. Lett.* **2006**, *74* (2), 306–312. https://doi.org/10.1209/epl/i2005-10523-2.

(144) Moulinet, S.; Bartolo, D. Life and Death of a Fakir Droplet: Impalement Transitions on Superhydrophobic Surfaces. *Eur. Phys. J. E* **2007**, *24* (3), 251–260. https://doi.org/10.1140/epje/i2007-10235-y.

(145) Bartolo, D.; Bouamrirene, F.; Verneuil, É.; Buguin, A.; Silberzan, P.; Moulinet, S. Bouncing or Sticky Droplets: Impalement Transitions on Superhydrophobic Micropatterned Surfaces. *Europhys. Lett.* **2006**, *74* (2), 299–305. https://doi.org/10.1209/epl/i2005-10522-3.

(146) Maitra, T.; Antonini, C.; Tiwari, M. K.; Mularczyk, A.; Imeri, Z.; Schoch, P.; Poulikakos, D. Supercooled Water Drops Impacting Superhydrophobic Textures. *Langmuir* **2014**, *30* (36), 10855–10861. https://doi.org/10.1021/la502675a.

(147) Schutzius, T. M.; Jung, S.; Maitra, T.; Eberle, P.; Antonini, C.; Stamatopoulos, C.; Poulikakos, D. Physics of Icing and Rational Design of Surfaces with Extraordinary Icephobicity. *Langmuir* **2015**, *31* (17), 4807–4821. https://doi.org/10.1021/la502586a.

(148) Cao, L.; Jones, A. K.; Sikka, V. K.; Wu, J.; Gao, D. Anti-Icing Superhydrophobic Coatings. *Langmuir* **2009**, *25* (21), 12444–12448. https://doi.org/10.1021/la902882b.

(149) Boreyko, J. B.; Chen, C. H. Self-Propelled Jumping Drops on Superhydrophobic Surfaces. *Phys. Fluids* **2010**, *22* (9), 1–2. https://doi.org/10.1063/1.3483222.

(150) Liu, G.; Fu, L.; Rode, A. V.; Craig, V. S. J. Water Droplet Motion Control on Superhydrophobic Surfaces: Exploiting the Wenzel-to-Cassie Transition. *Langmuir* **2011**, *27* (6), 2595–2600. https://doi.org/10.1021/la104669k.

(151) Boreyko, J. B.; Chen, C.-H. Restoring Superhydrophobicity of Lotus Leaves with Vibration-Induced Dewetting. *Phys. Rev. Lett.* **2009**, *103* (17), 174502. https://doi.org/10.1103/PhysRevLett.103.174502.

(152) Boreyko, J. B.; Baker, C. H.; Poley, C. R.; Chen, C.-H. Wetting and Dewetting Transitions on Hierarchical Superhydrophobic Surfaces. *Langmuir* **2011**, *27* (12), 7502–7509. https://doi.org/10.1021/la201587u.

(153) Lee, C.; Kim, C. Underwater Restoration and Retention of Gases on Superhydrophobic Surfaces for Drag Reduction. *Phys. Rev. Lett.* **2011**, *106* (1), 014502. https://doi.org/10.1103/PhysRevLett.106.014502.

(154) Lee, C.; Kim, C.-J. Wetting and Active Dewetting Processes of Hierarchically Constructed Superhydrophobic Surfaces Fully Immersed in Water. *J. Microelectromechanical Syst.* **2012**, *21* (3), 712–720. https://doi.org/10.1109/JMEMS.2012.2184081.

(155) Kumari, N.; Garimella, S. V. Electrowetting-Induced Dewetting Transitions on Superhydrophobic Surfaces. *Langmuir* **2011**, *27* (17), 10342–10346. https://doi.org/10.1021/la2027412.

(156) Manukyan, G.; Oh, J. M.; van den Ende, D.; Lammertink, R. G. H.; Mugele, F. Electrical Switching of Wetting States on Superhydrophobic Surfaces: A Route Towards Reversible Cassie-to-Wenzel Transitions. *Phys. Rev. Lett.* **2011**, *106* (1), 014501. https://doi.org/10.1103/PhysRevLett.106.014501.

(157) Checco, A.; Ocko, B. M.; Rahman, A.; Black, C. T.; Tasinkevych, M.; Giacomello, A.; Dietrich, S. Collapse and Reversibility of the Superhydrophobic State on Nanotextured Surfaces. *Phys. Rev. Lett.* **2014**, *112* (21), 216101. https://doi.org/10.1103/PhysRevLett.112.216101.

(158) Verho, T.; Korhonen, J. T.; Sainiemi, L.; Jokinen, V.; Bower, C.; Franze, K.; Franssila, S.; Andrew, P.; Ikkala, O.; Ras, R. H. A. Reversible Switching between Superhydrophobic States on a Hierarchically Structured Surface. *Proc. Natl. Acad. Sci.* **2012**, *109* (26), 10210–10213. https://doi.org/10.1073/pnas.1204328109.

(159) Prakash, S.; Xi, E.; Patel, A. J. Spontaneous Recovery of Superhydrophobicity on Nanotextured Surfaces. *Proc. Natl. Acad. Sci.* **2016**, *113* (20), 5508–5513. https://doi.org/10.1073/pnas.1521753113.

(160) Stamatopoulos, C.; Schutzius, T. M.; Köppl, C. J.; Hayek, N. El; Maitra, T.; Hemrle, J.; Poulikakos, D. On the Shedding of Impaled Droplets: The Role of Transient Intervening Layers. *Sci. Rep.* **2016**, *6* (1), 18875. https://doi.org/10.1038/srep18875.

(161) Vourdas, N.; Pashos, G.; Kokkoris, G.; Boudouvis, A. G.; Stathopoulos, V. N. Droplet Mobility Manipulation on Porous Media Using Backpressure. *Langmuir* **2016**, *32* (21), 5250–5258. https://doi.org/10.1021/acs.langmuir.6b00900.

(162) Nakajima, A.; Hashimoto, K.; Watanabe, T.; Takai, K.; Yamauchi, G.; Fujishima, A. Transparent Superhydrophobic Thin Films with Self-Cleaning Properties. *Langmuir* **2000**, *16* (17), 7044–7047. https://doi.org/10.1021/la000155k.

(163) Li, J.; Wan, H.; Ye, Y.; Zhou, H.; Chen, J. One-Step Process to Fabrication of Transparent Superhydrophobic SiO2 Paper. *Appl. Surf. Sci.* **2012**, *261*, 470–472. https://doi.org/10.1016/j.apsusc.2012.08.034.

(164) Yu, S.; Guo, Z.; Liu, W. Biomimetic Transparent and Superhydrophobic Coatings:

From Nature and beyond Nature. *Chem. Commun.* **2015**, *51* (10), 1775–1794. https://doi.org/10.1039/C4CC06868H.

(165) Walker, C.; Mitridis, E.; Kreiner, T.; Eghlidi, H.; Schutzius, T. M.; Poulikakos, D. Transparent Metasurfaces Counteracting Fogging by Harnessing Sunlight. *Nano Lett.* **2019**, *19* (3), 1595–1604. https://doi.org/10.1021/acs.nanolett.8b04481.

(166) Cai, W.; Shalaev, V. *Optical Metamaterials*; Springer: New York, 2010. https://doi.org/10.1007/978-1-4419-1151-3.

(167) Scaffardi, L. B.; Pellegri, N.; Sanctis, O. de; Tocho, J. O. Sizing Gold Nanoparticles by Optical Extinction Spectroscopy. *Nanotechnology* **2005**, *16* (1), 158–163. https://doi.org/10.1088/0957-4484/16/1/030.

(168) Kreibig, U.; Fragstein, C. v. The Limitation of Electron Mean Free Path in Small Silver Particles. *Zeitschrift für Phys.* **1969**, *224* (4), 307–323. https://doi.org/10.1007/BF01393059.

(169) Derkachova, A.; Kolwas, K.; Demchenko, I. Dielectric Function for Gold in Plasmonics Applications: Size Dependence of Plasmon Resonance Frequencies and Damping Rates for Nanospheres. *Plasmonics* **2016**, *11* (3), 941–951. https://doi.org/10.1007/s11468-015-0128-7.

(170) Chen, S. Survey over Image Thresholding Techniques and Quantitative Performance Evaluation. *J. Electron. Imaging* **2004**, *13* (1), 220. https://doi.org/1017-9909/2004/$15.00.

(171) Jui-Cheng Yen; Fu-Juay Chang; Shyang Chang. A New Criterion for Automatic Multilevel Thresholding. *IEEE Trans. Image Process.* **1995**, *4* (3), 370–378. https://doi.org/10.1109/83.366472.

(172) Otsu, N. A Threshold Selection Method from Gray-Level Histograms. *IEEE Trans. Syst. Man. Cybern.* **1979**, *9* (1), 62–66.

(173) Optotherm. Emissivity in the Infrared http://optotherm.com/emiss-table.htm (accessed Nov 7, 2017).

(174) Infrared Services. Emissivity Values for Common Materials http://www.infrared-thermography.com/material-1.htm (accessed Nov 7, 2017).

(175) Minkina, W.; Dudzik, S. *Infrared Thermography: Errors and Uncertainties*; John Wiley & Sons, 2009. https://doi.org/10.1002/9780470682234.

(176) Wang, C.; Zhang, W.; Siva, A.; Tiea, D.; Wynne, K. J. Laboratory Test for Ice Adhesion Strength Using Commercial Instrumentation. *Langmuir* **2014**, *30* (2), 540–547. https://doi.org/10.1021/la4044254.